medium-scale integrated (MSI) and large-scale integrated (LSI) circuits which are a form of functional (special-purpose) packaging.

The following general outlines describe a packaging scheme which may meet our objectives. Plugable functional subassemblies carry a significant number of IC packages. These subassemblies accept IC packages on standard grid dimensions. The standard grid dimensioning permits the blank subassembly to be premanufactured, and after mounting the IC packages, to be quickly intraconnected by a tape-controlled automatic machine. Special-purpose modules carrying discrete components, hybrid microelectronics, or LSI will fit the standard grid pattern being constrained to some multiple of the standard dimensions. The key to the acceptability of the whole packaging scheme just described is the technology and methodology for attaching the IC packages.

D. Tracking and Navigational Accuracy Analysis

1. Introduction, *T. W. Hamilton and D. W. Trask*

The DSN Inherent Accuracy Project was formally established by the DSN Executive Committee in July 1965. The objectives of the project are:

(1) Determination (and verification) of the inherent accuracy of the DSN as a radio navigation instrument for lunar and planetary missions.

(2) Formulation of designs and plans for refining this accuracy to its practical limits.

Achievement of these goals is the joint responsibility of the Telecommunications and Mission Analysis Divisions of JPL. To this end, regular monthly meetings are held to coordinate and initiate relevant activities. The project leader and his assistant (from the Mission Analysis and Telecommunications Divisions, respectively) report to the DSN Executive Committee, and are authorized to task project members to (1) conduct analyses of proposed experiments, (2) prepare reports on current work, and (3) write descriptions of proposed experiments. The project is further authorized to deal directly with those flight projects using the DSN regarding data-gathering procedures that bear on inherent accuracy.

The various data types and tracking modes provided by the DSIF in support of lunar and planetary missions are discussed in SPS 37-39, Vol. III, pp. 6–8. Technical work directly related to the Inherent Accuracy Project is presented in SPS 37-38, Vol. III, and in subsequent *Deep Space Network* SPS volumes, and is continued in the following subsections of this volume.

The first five articles (*Subsections 2–6*) of this section report on work carried out under the Tracking System Analytical Calibration (TSAC) activity. The TSAC activity provides calibration of tracking data and estimates of DSN parameters whose uncertainties represent limitations to navigational accuracy. In addition to the generation of analytic calibration coefficients, TSAC validates their proper transmission/utilization during a mission and performs detailed post-flight analysis of the DSN tracking data to uncover/resolve any anomalies which may exist. Further, this activity is concerned with defining the present inherent limitations to navigational accuracy and recommending feasible improvements which will reduce these limitations to meet future navigational accuracy requirements. This information is presented for the consideration of the DSN and flight projects in negotiating error levels for these parameters consistent with the navigational requirements of the projects and economical constraints.

The major guideline for TSAC in the formulation of an error budget is to maintain a balanced system of error sources. That is, the system is balanced such that a given expenditure of resources is budgeted to minimize the rss of the resultant navigational errors. In general, this necessitates advancing the state-of-the-art for the most critical error sources and, within the above constraints, reducing the effects of other error sources to a level which is negligible when compared to the most critical error source.

For a mission such as *Mariner* Mars 1969, the tightest bounds on the allowable errors for a number of parameters arise from the navigational accuracy requirements during encounter support. In particular, encounter navigational accuracy is most sensitive to error sources, which cause a diurnal signature on the radio tracking data (see Hamilton and Melbourne, SPS 37-39, Vol. III, pp. 18–23). These sources of error are of two classes: (1) those parameters which define the location of the DSS in inertial space, and (2) those phenomena which directly affect the DSS tracking data. The first category includes the location of the DSS with respect to the earth's crust, Universal Time (UT1), polar motion (the motion of the earth's crust with respect to the spin axis), precession and nutation (orientation of the earth's spin axis with respect to inertial space), and the ephemerides of the earth, moon, and target body. Of these, uncertainties in the first three are currently the major limitations to encounter support navigational accuracy. Utilizing the information on UT1 supplied by the

U. S. Naval Observatory (USNO) and the Bureau International L'Heure (BIH) and information on polar motion supplied by the BIH and the International Polar Motion Service (IPMS), the DSN has actively supported efforts to reduce the operational uncertainties of these three parameters. Improvements for the remaining ephemeris-related parameters have been primarily supported by non-DSN efforts.

The dominant sources of error in the second category, those affecting the tracking data directly, include charged particles (ionosphere and space plasma), troposphere, frequency system instability, and electrical phase path variations (through both the spacecraft and the DSS). Reducing the effect of all these error sources is directly supported by the DSN. In SPS 37-59, Vol. II, the real-time TSAC support of *Mariner* Mars 1969 encounter was described for two of these error sources, namely, UT1 (pp. 110–114) and the ionospheric calibration of radio tracking data (pp. 97–110). The latter article concentrated on the effect of calibrating the data for the southern hemisphere stations; the first article (*Subsection 2*) in this section extends this work to include the calibration of tracking data for the entire net. *Subsection 3* describes the effect of using the new and more accurate orbit determination program (DPODP) and also the effect of applying ionospheric corrections to the tracking data of past flights in obtaining the DSS locations utilized for the *Mariner* Mars 1969 mission. Our goals on *Mariner* Mars 1969 were to obtain spin axis (r_s) solutions good to 1.5 m and longitude (λ) solutions good to 3 m. Present indications are that these goals were met, although further analysis is required. The spread of Goldstone r_s solutions was 2 m about the average before the ionospheric corrections were applied. The application of the ionospheric corrections caused the average to move by 4 m, but the spread reduced to 1 m. This spread may be even further reduced when corrections for the charged particles in the space plasma (not available for all missions) are applied to the tracking data. These corrections are discussed for the cases of *Mariner V* and *Pioneer IX* in *Subsection 4*, where it is shown that the effects of the charged particles in the space plasma typically affect the DSS location solutions on the order of 1 m.

The tracking data corrections due to the ionosphere and the troposphere are functions of the path (elevation angle) through which the radio wave transverses the atmosphere. For the case of the ionospheric corrections, the program ION (SPS 37-58, Vol. II, pp. 66–73) computes the required elevation angles using the round-trip flight time and an algorithm permitting the facile computation of view periods for a distant spacecraft, as presented in *Subsection 5*. This algorithm requires a knowledge of the right ascension and the declination of the probe within a few days of the time of interest. Although the use of this simple algorithm saves computing time, the algorithm is not exact. The size of the error is analyzed in the following article (*Subsection 6*), where it is found that an error of less than 0.03 m is introduced into the ionospheric calibration process using tabulated values of right ascension and declination 5 days apart. These errors are small compared to the calibration goals for the *Mariner* Mars 1969 Project.

Subsection 7 describes the use of sequential estimation on the orbit determination problem for a planetary orbiter. The sensitivity of estimation accuracy to placement of the data span was studied for an idealized case of a spherical central body and it was found that the tracking of the probe over a span which is centered about, or at least includes, the periapsis time is the most efficient strategy.

The following three articles (*Subsections 8–10*) discuss recent work on the lunar surface mass distribution. For over one year, JPL and the Aerospace Corporation have been cooperating in an effort to determine the lunar gravimetric data from a dynamic fit of the *Lunar Orbiter* doppler tracking data, using a dense grid of discrete mass points on the lunar surface. *Subsection 8* presents the surface (earth side) mass distribution obtained to date from this work, while *Subsection 9* presents a representation of these local gravity features in terms of accelerations at a 100-km altitude (representative of the altitude at which the data most critical to the construction of this model was obtained) and expands on the work presented in *Subsection 8* by using the residual accelerations to estimate additional masses. Because of the success of utilizing the *Lunar Orbiter* tracking data, which has a periapsis altitude of 50 to 100 km, it was felt that the data from the *Apollo 10* and *11* missions, which were tracked within 11 km of the lunar surface, may provide even more information. Unfortunately, as reported in *Subsection 10*, there seems to be a sufficient number of anomalies in the *Apollo* tracking data to preclude its usefulness for this type of analysis.

The landed *Surveyor* two-way doppler "observe minus computed" residuals have systematic structures as shown in SPS 37-50, Vol. II, pp. 110–125, and SPS 37-51, Vol. II, pp. 42–50. The long-term periodocities are lunar ephemeris-dependent while the diurnal signature has a number of suspected causes, among which are the imperfections in the tropospheric refraction corrections applied to the

doppler and ionospheric charged-particles effects which have been discussed in previous issues. The tracking data from the *Surveyor* spacecraft, while they were resting on the lunar surface, represents an excellent source of accurate DSS location solutions providing certain problems such as the above can be surmounted.

An additional corrupting influence associated with the lunar landed *Surveyor* tracking data that prevents the determination of absolute DSS longitude is the physical libration of the lunar figure, which is the topic of the next article (*Subsection 11*). In SPS 37-56, Vol. II, pp. 74–80, the effect of the Heyn physical libration model was compared against a later model (Eckhardt's libration coefficients) as well as against no model. It was surprising that no single model was best for all *Surveyors* utilized in this study and that, in fact, one case was best with no model. However, the libration models utilized in this study were truncated; therefore, the article in this issue investigates the effect of this truncation. It is found that the failure of the model to properly fit the *Surveyor* data does not result from the truncation of the libration series. However, some of the truncated terms are significant.

Generally, reductions from earth–satellite tracking data result in a high correlation between the gravitational mass of the earth ($GM_\oplus$) and the scale of the coordinate system (i.e., linear coordinates of the tracking station). This is especially true in the case of optical data that relies on an independent determination of $GM_\oplus$. To provide the scale for quantities that involve linear dimensions, the most accurate $GM_\oplus$ determinations have been provided from the radio tracking data of deep space probes, such as those reported in SPS 37-43, Vol. III, pp. 3–18, and SPS 37-44, Vol. III, pp. 11–28. At present, these $GM_\oplus$ determinations from deep space probe data have no close competitors in that their claimed uncertainty is an order of magnitude less than provided by other techniques. In previous SPS articles (SPS 37-53, Vol. II, pp. 16–20; SPS 37-56, Vol. II, pp. 80–85), the ability to determine $GM_\oplus$ from a moderate-altitude satellite and from a family of three high-altitude satellites (including *Syncom II*) was analyzed. In *Subsection 12*, this analysis is extended to reveal the relative quality of $GM_\oplus$ solutions obtainable as a function of the elements of the earth-orbiting spacecraft. This analysis was accomplished by the use of the Multiple-Link Satellite Program (MLSP) discussed in *Subsection 13*. MLSP was developed as a tool to study the statistics of satellite orbit determination using data types involving several satellites. In particular, the MLSP assumes that the orbit determination process will be done with radio ranging and/or doppler data; however, unlike current orbit determination programs, the MLSP does not confine the signal path to direct ground station–satellite measurements, but allows the signal to be relayed many times, including relays between satellites.

The last article (*Subsection 14*) in this section demonstrates the feasibility of computing doppler observables from differenced-range observables. Changes are specified for the DPODP which should produce differenced-range doppler accurate to 10^{-5} m/s or better for all count times above 0.2 s. This is compatible with the design goal of being able to compute range differences accumulated over 10^4 s to 0.1 m or better.

2. Results of *Mariner* Mars 1969 In-Flight Ionospheric Calibration of Radio Tracking Data,

B. D. Mulhall, V. J. Ondrasik, and N. A. Mottinger[4]

Using the procedures described by Mulhall in SPS 37-57, Vol. II, pp. 24–29, the authors processed the ionospheric measurements obtained from the Faraday rotation polarimeters at the Venus site and at the University of New England, Armidale, Australia, and from ionosonde vertical sounding stations at Tortosa, Spain, Mount Stromlo and Woomera, Australia, and Johannesburg, South Africa. These measurements were converted to total electron content and mapped to the *Mariner* ray path; range and doppler corrections were computed and applied to *Mariner VI* and *VII* radio tracking data. The results of the calibrations are shown in Table 16.

The recommended changes listed in Table 16 were determined by differencing the results of Double Precision Orbit Determination Program (DPODP) solutions using in-flight data which had not been calibrated for the ionosphere with station location based on post-flight solutions using uncalibrated data versus DPODP runs using ionospherically calibrated data and station location based on post-flight calibrated data (see Mottinger, *Subsection 3*). These differences are not necessarily the actual ionospheric effect on the orbit determination since the error introduced by the ionosphere into the in-flight data might be masked in part by the uncalibrated station location.

For example, the ionosphere caused an error which consistently increased the apparent station spin radius r_s.

[4]The authors wish to express their appreciation to Prof. F. Hibbard, The University of New England, Armidale, NSW, Australia; the staffs of the ionospheric observatories of Mount Stromlo and Woomera, Australia; Fr. E. Galdon and staff, Observatorio de Ebro, Tortosa, Spain; and R. M. Vice and staff, National Institute for Telecommunications Research, Johannesburg, South Africa, for recording and reducing ionospheric measurements.

Table 16. Recommended changes due to ionospheric effect, *Mariner* Mars 1969 mission

Mission	**B** • **R**, km	**B** • **T**, km
Mariner VI	−53	48
Mariner VII	−40	20

It is very likely that the ionosphere had a similar effect for *Mariner* Mars 1969. Consequently, station locations based on uncalibrated *Mariner V* data would compensate in part for the ionospheric error in *Mariner* Mars 1969 data.

The ionospheric effect on navigation shown in Table 16 is measured in terms of the **B** vector, a vector perpendicular to the incoming asymptote, from the center of the planet Mars to the probe's aiming point. **B** • **T** is the component of the **B** vector in the ecliptic plane and **B** • **R** is the component perpendicular to **B** • **T**.

The ionospheric effects shown in Table 16 are different from the effects shown by Ondrasik in SPS 37-59, Vol. II, pp. 97–110, because Table 16 shows the results obtained by calibrating the entire net (not just the southern hemisphere stations) and does not include certain days with ionospheric measurements that could not be reduced prior to encounter.

The ionospheric effect was considerably lower than anticipated. Although 1969 has been a year of high ionospheric concentrations due to solar flare activity, the ionosphere was relatively inactive during the period when the calibration was performed (July 1 to August 5, 1969). This low activity was particularly noticeable in the southern hemisphere where the total columnar electron ionospheric content was typically less than half of the content in the northern hemisphere. Due to the southerly declination of the *Mariner* spacecraft, most of the radio tracking data were obtained from southern latitude stations. Consequently, the smaller effect of the southern ionosphere outweighed the effect in the northern ionosphere and reduced the magnitude of the calibration for the entire net.

Future plans include converting the ionospheric calibration programs from a power series to a Chebychev series. The power series proved to be an inferior smoothing technique for the ionospheric range calibration prior to differentiation into a doppler calibration. Occasionally, the power series fit was so noisy that the calibration for that day could not be used. The deficiency was recognized prior to encounter but could not be incorporated in the software system without jeopardizing the calibration effort. The software is presently being revised to incorporate the Chebychev series and the ionospheric effect will be recomputed for the *Mariner* Mars 1969 data.

Measurement mapping techniques will also be studied for possible improvement as well as techniques for resolving ambiguities in Faraday rotation measurements.

3. Status of DSS Location Solutions for Deep Space Probe Missions: Third-Generation Orbit Determination Program Solutions for *Mariner* Mars 1969 Mission, N. A. Mottinger

a. Introduction. As discussed by Mottinger and Trask in SPS 37-48, Vol. II, pp. 12–22, the uncertainties in DSS locations can become limiting factors to the navigational accuracy obtainable with earth-based radio tracking data. To meet the navigational goals under consideration for some planetary projects, the uncertainties in the DSS longitude σ_λ and the distance off the earth's spin axis[5] σ_{r_s} must be known on the order of 1 m. In an earlier article, Hamilton, Grimes, and Trask (SPS 37-44, Vol. III, pp. 4–11) presented an approximate method for determining the navigational accuracy obtainable during the encounter phase of a mission and discussed the dependence of this accuracy on station location uncertainties.

A general discussion of DSS location solutions obtained from postflight analyses is presented in SPS 37-48, Vol. II. SPS 37-49, Vol. II, pp. 10–23, gives the solutions for DSS locations obtained in processing the *Mariner V* data at about the same time the mission was in progress.

The third article in the series (SPS 37-56, Vol. II, pp. 45–58) discussed solutions obtained which were considered accurate at the 5-m level in r_s and λ. The results presented in this article are location solutions obtained with a third-generation orbit determination program, the double-precision orbit determination program (DPODP)[6]. Ionospheric corrections have been included in the reductions and have reduced the scatter to about 2 m in r_s and 2.5 m in λ. Uncertainties for these solutions are about 3 m.

b. Discussion. The reduction of earth-based radio tracking data done in the last year, using the single-precision orbit determination program (SPODP) (Ref. 1)

[5] r_s = geocentric radius times the cosine of the geocentric latitude.
[6] See SPS 37-47, Vol. II, pp. 35–41, SPS 37-38, Vol. III, pp. 24–26, and successive articles in the DSN Volume III series.

and more recently the DPODP, has produced station location solutions that are consistent at and below the 5-m level. The 10-m level was broken with the SPODP by processing the planetary zero declination and encounter two-way doppler data. These results are discussed in SPS 37-56, Vol. II, pp. 45–58, and were also presented at the American Geophysical Union Meeting in April 1969 (Ref. 2). In the early part of the year, reductions with essentially the same data were initiated using the DPODP and employing simple averaging techniques to create a best estimate. Maximum disagreement between the two sets of solutions (SPODP vs DPODP) was 3.3 m in spin axis r_s and 4.2 m in longitude, with the average difference of 1 m in r_s and 1.6 m in longitude. The implied quality of the SPODP results was extremely encouraging, considering the vast improvements and changes in the DPODP over the SPODP. Following these reductions, changes were made in the timing and polar motion polynomials provided by Muller and Chao (SPS 37-57, Vol. II, pp. 42–51). The new polynomials incorporated the changes in UT1 made by the U.S. Naval Observatory (USNO) after switching to the Bureau International L'Heure (BIH) polar motion as well as the processing and data selection choices made by Muller and Chao. Succeeding reductions using the new timing and polar motion coefficients were performed exclusively with the DPODP. A program was developed to combine the estimates obtained from each reduction in the same manner as were the *Ranger* Block III station location and other common parameter estimates (SPS 37-43, Vol. III, pp. 3–18).

Breaking the 5-m level was made possible by the ionosphere corrections produced by Mulhall, Ondrasik, and Thuleen as discussed in a JPL internal document.[7] As will be shown, the scatter in location estimates was reduced with the application of the ionosphere corrections. The most significant reduction was 50% for r_s at Goldstone. The absolute longitude solutions from the planetary encounter solutions, *Mariners IV* and *V*, diverge by 2.9 m following the application of the ionosphere corrections. The exact agreement noted in SPS 37-56, Vol. II, pp. 45–58, appears to have been coincidental. Possible explanations for this scatter lie in the ephemeris, precession rates, or a secular rate in UT1, which would be associated with proper motion of the stars used to determine UT1. A half meter of the spread is due to the specific ephemeris developed for the *Mariner* Mars 1969 encounter activities. Using the current recommended ephemeris of the solar system reduces the spread to 2.4 m.

[7]Mulhall, B. D., *In Flight Ionospheric Calibration Procedures for Mariner Mars 1969 Radio Tracking Data*, June 26, 1969.

Priority was given to processing the *Mariner IV* and *V* data near zero declination to obtain r_s and $\Delta\lambda$ (relative longitude) and encounter for r_s and λ. Although some *Pioneer* zero declination cases were analyzed, the analyses are neither as complete as for the *Mariner* cases nor were charged-particle calibrations available. The locations obtained with the ionosphere corrections appear to be reliable at the 3-m level.

c. DPODP vs SPODP station locations. The decisions which led to the reduction of solely planetary data to support the *Mariner* Mars 1969 mission have been discussed in SPS 37-56, Vol. II, pp. 45–58, and Ref. 2. Basically, the problem is that the lunar and planetary ephemerides are not compatible at the level desired in terms of the DSS locations obtained from these two mission types.

The *Mariner* reductions listed in Table 17 are very nearly identical to those listed in a similar table in SPS 37-56, Vol. II, p. 50. Since these earlier reductions had been performed with the SPODP, it was attempted to reduce the same data with the DPODP to test the agreement in station locations obtained by these two programs. In addition to the numerical accuracy of 16 digits instead of 8 for the SPODP, other improvements such as the employment of a polar motion model[8] in the DPODP will cause the SPODP and DPODP location solutions to differ. The agreement noted with initial reductions from the DPODP were very encouraging.

Location set (LS) 14, the best SPODP set, is compared with the first DPODP set, LS 17, in Table 18. Average disagreement was 1 m in r_s and 1.6 m in λ, with worst case of 4.2 m occurring in λ. The uncertainty expressed with the locations, both SPODP and DPODP, was about 5 m. The important item, however, was the overall general consistency obtained between programs.

d. Location combination techniques. A combination technique developed by J. D. Anderson and used by Trask and Vegos to combine the *Ranger* Block III missions (SPS 37-43, Vol. III, pp. 3–18) was also used to combine these DPODP estimates. The technique uses the normal equations matrix from the orbit determination program and condenses the information, producing a new information matrix on those parameters that are common to several missions and whose combined estimate is desired. The problem present with the station location solutions obtained from the zero-declination

[8]A polar motion model was nonexistent in the SPODP. Polar motion had to be applied after the reduction assuming a mean pole position over the time interval in question.

reductions is that statistical significance is attached to the absolute station longitudes by the program when it is not clear where this information comes from. Relative longitudes are well determined, however, and it is this information that must be brought out in the normal matrix. A technique adopted was to invert the matrix, corrupt the absolute longitude uncertainties by an arbitrary factor, generally 1 km, and reinvert to obtain the new normal matrix. This preserves the information on relative longitudes by increasing the correlation between stations (longitude), while destroying information on absolute. It may not be the most desirable technique to use, however, because of the double inversion required. Satisfactory results appear to have been obtained with this method. Other techniques will be investigated which may lead to abandonment of this procedure.

Similar techniques were developed for use as an information matrix in preserving relative locations at the Goldstone and Madrid DSCCs where these are accurately known from geodetic surveys. The Australian stations are too far apart to be able to rely upon the geodetic relative locations.

e. Advanced station location solutions using the DPODP. As mentioned earlier, Table 17 is essentially a duplicate of the *Mariner* missions listed in SPS 37-56, Vol. II, p. 50, Table 1. Summarized are the flights analyzed, the time span of each, number of doppler points fit, ephemeris, and other items pertinent to the reduction. One of the most interesting items is the new timing polynomials which have been used. The difference, UT1 − UTC, is presented in each table; that in SPS 37-56, Vol. II, is for the system as it existed then and that in Table 17 of this article as it stands now. Pole positions are also shown. Although they are applied for each data point in the program, an average value was calculated for the time span of the flight for inclusion in this table. For the *Mariner IV* and *V* encounter cases, it is possible to note very good agreement between the changes in UT1 − UTC for the old and new timing systems and the shift in DSS longitude.

This table also lists five different *Pioneer* reductions which have been performed with these probes in the zero-declination configuration. To distinguish between different zero-declination passages for the same spacecraft, the letters A and B have been added. If the spacecraft is near the threshold of the 85-ft antenna, as was *Pioneer IX* in this case, the data is quite noisy (~0.1 cycle). The 210-ft antenna data is not as noisy (~0.03 cycle).

The table concludes with the declination of the probe and the sun–earth–probe (SEP) angle. The latter is useful for comparing possible ionospheric and space plasma effects on the data from different missions.

As was mentioned earlier, problems did exist with some of the *Pioneer* zero-declination reductions. Specifically, the *Pioneer VIIA, VIIIB,* and *IX* reductions had occasional solutions which disagreed significantly with the existing *Mariner* solutions. For these reasons they were never included in a combination. These can be seen in Tables 19 and 20.

Table 17 also summarizes the data spans of the *Mariners* used with ionospheric corrections.[9] In some cases these represent a significant reduction in the number of points or even stations due to a lack of ionospheric calibration data. Because of the long lead time required to obtain ionospheric total electron content from ionosonde data, only the spans listed in Table 17 could be calibrated prior to *Mariner* Mars 1969 encounter.

Additional data have been obtained and are awaiting the conclusion of this report and other *Mariner* Mars 1969 summaries before they can be applied to the data. Figures 33 and 34 show what the application of the ionospheric corrections (discussed in Footnote 7) did to the r_s and longitude solutions, respectively, at the Goldstone DSCC. However, it should be noted that, due to the times at which the particular missions occurred and the particular stations tracking, the northern hemisphere stations received the largest corrections. Southern hemisphere stations, as may be noted in Table 21, did not show the scatter that the northern hemisphere did. In Figs. 33 and 34 are the combined solution, no ionosphere (LS 24), and solutions from constituent runs and those with the ionosphere corrections (LS 25). Absolute and relative locations for all stations are listed in Tables 22 and 23. In some cases it was necessary to transfer a solution from DSS 11 or DSS 14 to DSS 12 using the geodetic survey relative locations. These relative locations are given in Table 24. In other cases, solutions for DSS 12 were available directly and indirectly in the same reduction. Most significant is the reduction of the 4.9-m scatter in the left side (non-ionosphere) to 2.3 m on the right side of Fig. 33, r_s solutions. The combined solutions

[9]In the course of compiling this table a mistake was uncovered. For *Mariner V* cruise, the data from DSS 62 was left in the fit but the station location was not estimated. This was corrected by eliminating the DSS 62 data. The combination has not been redone. The spin axis of DSS 14 changed ~0.1 m. In future reductions, with more ionospheric data available, this will be corrected.

Table 17. Flight analysis summary

Flight	Doppler points	Doppler count time, s	Tracking span, days	Ephemeris		DPODP		ET − UTC, s	UT1 − UTC ms	Effective data weights (60-s count time), mm/s	Instantaneous pole position (BIH)[a]				Probe declination, deg	SEP angle, deg	Location set
				DE	LE	Mod	Lock file				X, m	Y, m	ΔX, m	ΔY, m			
Non-ionosphere reductions																	
Mariner IV Encounter	419	600[b]	15 (Jul 7–21, 1965)	69	16	5.0	5A	36.178	19	3.3	−2.9	13.9	1.3	0.6	−3	77	24
Mariner V Cruise	616	600	58 (Jul 21–Sep 16, 1967)	69	16	4.3	5A	Start 37.965 End 38.113	66 94	3.3	−0.2	6.5	0.5	0.4	−8 to 8	35–20–35	24
Encounter	561	600[b]	11 (Oct 14–24, 1967)	69	16	5.0	5A	38.198	107	3.3	−0.5	6.5	0.1	0.1	6	45	24
Post-encounter	665	600	15 (Oct 29–Nov 12, 1967)	69	16	5.0	5A	38.240	100	3.3	−0.6	6.7	0.03	0.4	2 to −2	43	24
Pioneer VIIA	1392	600	43 (Aug 19–Sep 30, 1966)	69	16	5.0	5A	Start 37.095 End 37.204	13 30	3.3 3.3	0.8	10.9	2.4	0.4	−1.4 to 0.8	150	—
Pioneer VIIB	75	60	8 (Jul 27–Aug 3, 1968)	69	16	5.0	5A	38.837	36	3.3	2.6	5.2	0.06	0.1	3 to −2	54	—
Pioneer VIIIA	370	300	9 (Jun 3–11, 1968)	69	16	5.0	5A	38.699	−4	3.3	1.5	6.7	0.2	0.2	1.3 to −1.3	102–105	—

[a]Although a polar motion model is present in the DPODP, these values were computed at the midpoint of the tracking span primarily for comparison with previous articles.

[b]Count time reduced to 60 s during encounter.

Table 17 (contd)

Flight	Doppler points	Doppler count time, s	Tracking span, days	Ephemeris		DPODP		ET − UTC, s	UT1 − UTC ms	Effective data weights (60-s count time), mm/s	Instantaneous pole position (BIH)[a]				Probe declination, deg	SEP angle, deg	Location set
				DE	LE	Mod	Lock file				X, m	Y, m	ΔX, m	ΔY, m			
Non-ionosphere reductions																	
Pioneer VIIIB	520	600	19 (Dec 25, 1968–Jan 12, 1969)	69	16	5.0	5A	39.244	30	3.3	−4.6	7.6	0.5	1.2	−2.8 to 5.0	80	—
																50	—
Pioneer IX	309	600	6 (May 8–13, 1969)	69	16	5.0	5A	39.573	−1	3.3	1.0	11.4	0.3	0.06	−3 to 3		—
Ionosphere reductions																	
Mariner IV Encounter	373		12 (Jul 10–21, 1967)	71	16	5.0	5A			3.3							25
Mariner V Cruise	364		58 (Jul 21–Sep 16, 1967)	69	16	5.0	5A			3.3							25
Encounter	561		11 (Oct 14–24, 1967)	69	16	5.0	5A			3.3							25
Post-encounter	411		15 (Oct 29–Nov 12, 1967)	69	16	5.2	5A			3.3							25

Table 18. First DPODP estimates compared with best SPODP

DSS	DPODP (LS 17) − SPODP (LS 14)	
	Δr_s, m	$\Delta_{\Delta\lambda}$[a] from DSS 12, m
12	0.1	1.0
41	0.5	0.7
42	0.8	1.3
51	3.0	4.2
61	3.3	1.5
62	0.4	2.2
Average	1.0	1.6

[a] $(\lambda_i - \lambda_{12})_{LS\ 17} - (\lambda_i - \lambda_{12})_{LS\ 14}$

also differ by about 4 m. The changes noted all agree well with those anticipated by Mulhall et al. In these figures the standard deviations are not shown since the reduction of scatter and the change in absolute value is of primary importance. Figure 34 shows the ionosphere effects on the absolute longitude solutions obtained in the *Mariner IV* and *V* encounter reductions. Unlike the previous figure showing the spin axis solutions, the addition of the ionosphere has disrupted the previous continuity in absolute longitude solutions. This earlier agreement appears to have been coincidental, since portions of the disagreement may be explained in terms of possible ephemeris inconsistencies [*Mariner IV* (Mars) vs *Mariner V* (Venus)], or more realistically in terms of precession errors which could account for 0.3 m, or a secular drift in UT1 which could result from proper motions of stars used by the USNO to determine UT1.

Location set 24 was produced using solutions obtained with Development Ephemeris (DE) 69. Just before the ionosphere corrections for *Mariner IV* were obtained, a special ephemeris (DE 71) was issued to support the *Mariner* Mars 1969 encounter activities. DE 71 was intended only for use during the encounter phase of *Mariner* Mars 1969 to facilitate the fitting of doppler and range data during this critical phase of the mission.[10] In order to support the station location effort, the *Mariner IV* data were refitted to DE 71, corrected for ionosphere, and used in the combination program along with other ionosphere-corrected station locations. The changes observed in the *Mariner IV* longitude solutions using DE 71 were the predicted 0.5 m. The solutions corrected for ionosphere appear in Figs. 33 and 34. The combination with this ephemeris produced insignificant changes in λ because the *Mariner V* solution dominated the weighted solution due to its smaller uncertainties. For purposes of general comparison, 0.5 m should be subtracted from the *Mariner IV* longitude plotted in the right-hand side of Fig. 34 to obtain the correct indication of the agreement with *Mariner V*. Spin axis was not significantly affected by the change in ephemeris. DE 69 will be used for all station location reductions until a different ephemeris is recommended.

New ionosphere corrections will be computed for these missions since Mulhall et al have more data for them and better ideas and programs for preparing the corrections. Efforts are also underway to provide space plasma corrections.

Improvements have also been made in Z, the component along the earth's spin axis. Values prepared by Lambeck (Ref. 3) at the Smithsonian Astrophysical Observatory (SAO) were incorporated in LSs 24 and 25. The changes made in Z vary from 4 to 55 m, when compared with the previous sets. Although these changes have imperceptible effects on doppler tracking, they can have quite an effect on range data, particularly at extremely high or low declinations. When they were incorporated into the *Mariner* Mars 1969 reductions, a low-declination case, using the DPODP, approximately 30- to 40-m reductions occurred in the range biases, confirming that they represented an improvement. Confidence at the 15-m level was expressed by SAO for these Z values as computed using dynamical and geometrical fits to Baker–Nunn and other earth–satellite data.

Although there have been significant advances in station locations obtained using the ionosphere corrections, the troposphere model used in the SPODP and the DPODP has come under examination. In consideration of goals of the *Mariner* Mars 1969 mission and future missions, studies have been made of the tropospheric refraction effects on the doppler signal and how this affects determination of station locations. Balloon measurements of pressure, temperature, and humidity are being analyzed to see which measurements will be necessary to calibrate these effects out of the tracking data.

During the *Mariner* Mars 1969 mission, changes were made in the existing refraction model. The troposphere model represents a least-squares fit from the horizon to the zenith to a ray trace model based upon a standard

[10] O'Handley, D. A., *Ephemeris of Mars for Mariners 6 and 7*, Aug. 15, 1969 (JPL internal document).

Table 19. Absolute station locations and statistics[a]

DSS	Data source	Distance off spin axis, km	1-σ standard deviation, m	Geocentric longitude,[b] deg	1-σ standard deviation,[b] 10^{-5} deg	Distance along spin axis,[c] km
Non-ionosphere reductions—DPODP						
11		5206.3xxx		243.15xxxx		3676.xxx
	Mariner IV encounter	40.8	2.9	063.3	5.6	759
	Pioneer VIIA	40.8	1.6	045.4	17.0	759
	Pioneer VIIIA	38.2	1.9	068.6	109.0	759
12		5212.0xxx		243.19xxxx		3665.xxx
	Mariner V encounter	47.5	2.1	456.0	3.6	624
	Mariner V postencounter	50.9	1.9	458.8	9.8	624
	Pioneer VIIA	50.8	1.2	438.2	16.5	624
	Pioneer VIIIB	48.4	3.6	431.8	77.4	624
	Pioneer IX	46.9	5.8	449.8	61.0	624
14		5203.9xxx		243.11xxxx		3677.xxx
	Mariner V cruise	96.4	2.4	053.1	9.2	048
	Mariner V encounter	94.2	1.7	052.8	3.6	048
	Mariner V postencounter	93.6	3.0	052.3	9.8	048
	Pioneer VIIB	95.7	2.5			
	Pioneer IX	99.2	5.7	043.8	62.0	048
41		5450.xxxx		136.88xxxx		−3302.xxx
	Mariner V encounter	197.5	2.1	753.1	3.0	238
	Mariner V postencounter	200.0	2.4	757.8	9.7	238
	Pioneer VIIA	200.6	8.0	736.5	17.6	238
42		5205.3xxx		148.98xxxx		−3674.xxx
	Mariner IV encounter	49.4	2.9	128.8	5.0	628
	Mariner V cruise	50.3	1.4	131.1	9.3	628
	Pioneer VIIA	51.9	1.6	112.9	16.5	628
	Pioneer VIIIA	47.8	1.6	137.8	108.0	628
	Pioneer VIIIB	47.5	2.1	100.4	75.7	628
	Pioneer IX	42.4	7.8	126.8	62.0	628
51		5742.9xxx		27.68xxxx		−2768.xxx
	Mariner IV encounter	40.8	2.6	543.2	4.5	760
	Pioneer VIIIB	37.0	2.4	519.2	75.7	760
	Pioneer IX	39.7	9.1	539.6	62.0	760
61		4862.6xxx		355.75xxxx		4114.xxx
	Mariner V cruise	03.7	1.4	101.9	9.3	829
	Mariner V postencounter	05.6	5.5	103.3	10.4	829
	Pioneer VIIIA	12.0	1.9	107.4	109.0	829
62		4860.8xxx		355.63xxxx		4116.xxx
	Mariner V cruise	14.9	2.1	221.9	9.8	950
	Mariner V encounter	15.1	2.0	222.1	3.3	950
	Mariner V postencounter	15.5	2.4	223.4	10.0	950
	Pioneer IX	12.7	8.1	207.5	69.0	950

[a]These are formal uncertainties computed by the DPODP based on data weights listed in Table 17. They do not include uncertainties in Universal Time, polar motion, ephemeris, ionosphere, or space plasma, but are about 1.5 times the visible noise on the data.

[b]The minor part may be assumed to be tabulated in meters, where the equivalence of 10^{-5} deg at: DSSs 11, 12, 14 = 0.91 m, DSSs 61, 62 = 0.85 m, DSS 51 = 1.00 m, DSS 41 = 0.95 m, and DSS 42 = 0.91 m.

[c]This component was not estimated, but is included for completeness.

Table 19 (contd)

DSS	Data source	Distance off spin axis, km	1-σ standard deviation, m	Geocentric longitude,[b] deg	1-σ standard deviation,[b] 10^{-5} deg	Distance along spin axis,[c] km
			Ionosphere reductions			
11		5206.3xxx		243.15xxxx		3676.xxx
	Mariner IV encounter	41.8	2.9	065.3	6.2	763
12		5212.0xxx		243.19xxxx		3665.xxx
	Mariner V encounter	52.3	2.1	455.5	3.6	628
	Mariner V postencounter	54.5	2.0	459.4	10.8	628
14		5203.9xxx		243.11xxxx		3677.xxx
	Mariner V cruise	98.6	2.7	057.7	4.9	052
	Mariner V encounter	99.6	1.7	051.9	3.6	052
	Mariner V postencounter	97.5	3.0	052.6	10.8	052
41		5450.xxxx		136.88xxxx		−3302.xxx
	Mariner V encounter	198.0	2.1	749.7	3.0	243
	Mariner V postencounter	200.3	3.0	756.8	10.7	243
42		5205.3xxx		148.98xxxx		−3674.xxx
	Mariner IV encounter	50.1	3.3	130.3	5.8	646
	Mariner V cruise	50.5	2.0	136.8	6.0	646
51		5742.9xxx		27.68xxxx		−2768.xxx
	Mariner IV encounter	42.1	3.2	544.1	5.0	744
61		4862.6xxx		355.75xxxx		4114.xxx
	Mariner V cruise	06.9	1.6	107.0	6.0	
62		4860.8xxx		355.63xxxx		4116.xxx
	Mariner V encounter	17.9	2.0	219.8	3.3	908
	Mariner V postencounter	20.1	3.0	224.3	11.0	908

Table 20. Relative longitude solutions—nonionosphere[a]

Source	$\Delta\lambda_{12-41}$	$\Delta\lambda_{12-42}$	$\Delta\lambda_{12-51}$	$\Delta\lambda_{12-61}$	$\Delta\lambda_{12-62}$
	906.30xxxx	94.21xxxx	215.50xxxx	−112.55xxxx	−112.43xxxx
Mariner IV encounter	—	327.6	913.3	—	—
Mariner V cruise	—	326.6	—	644.3	764.3
Mariner V encounter	702.9	—	—	—	766.1
Mariner V postencounter	701.0	—	—	644.5	764.6
Pioneer VIIA	701.7	325.3	—	—	—
Pioneer VIIIA	—	323.9	—	645.7	—
Pioneer VIIIB	—	331.4	912.6	—	—
Pioneer IX	—	323.0	910.2	—	757.7

[a]See Footnote b, Table 19.

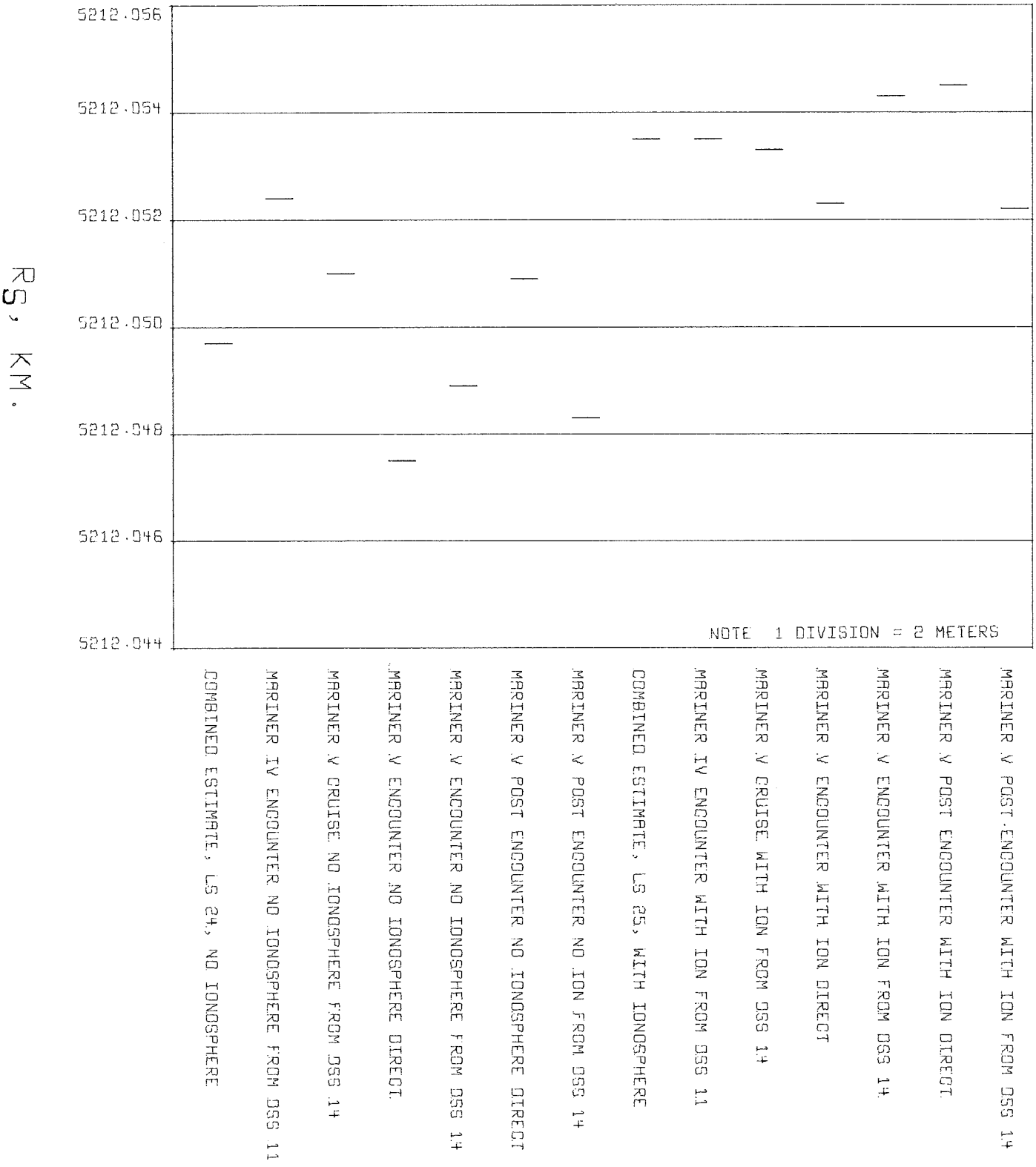

Fig. 33. Distance off spin axis, earth-fixed system (1903.0 pole), DSS 12

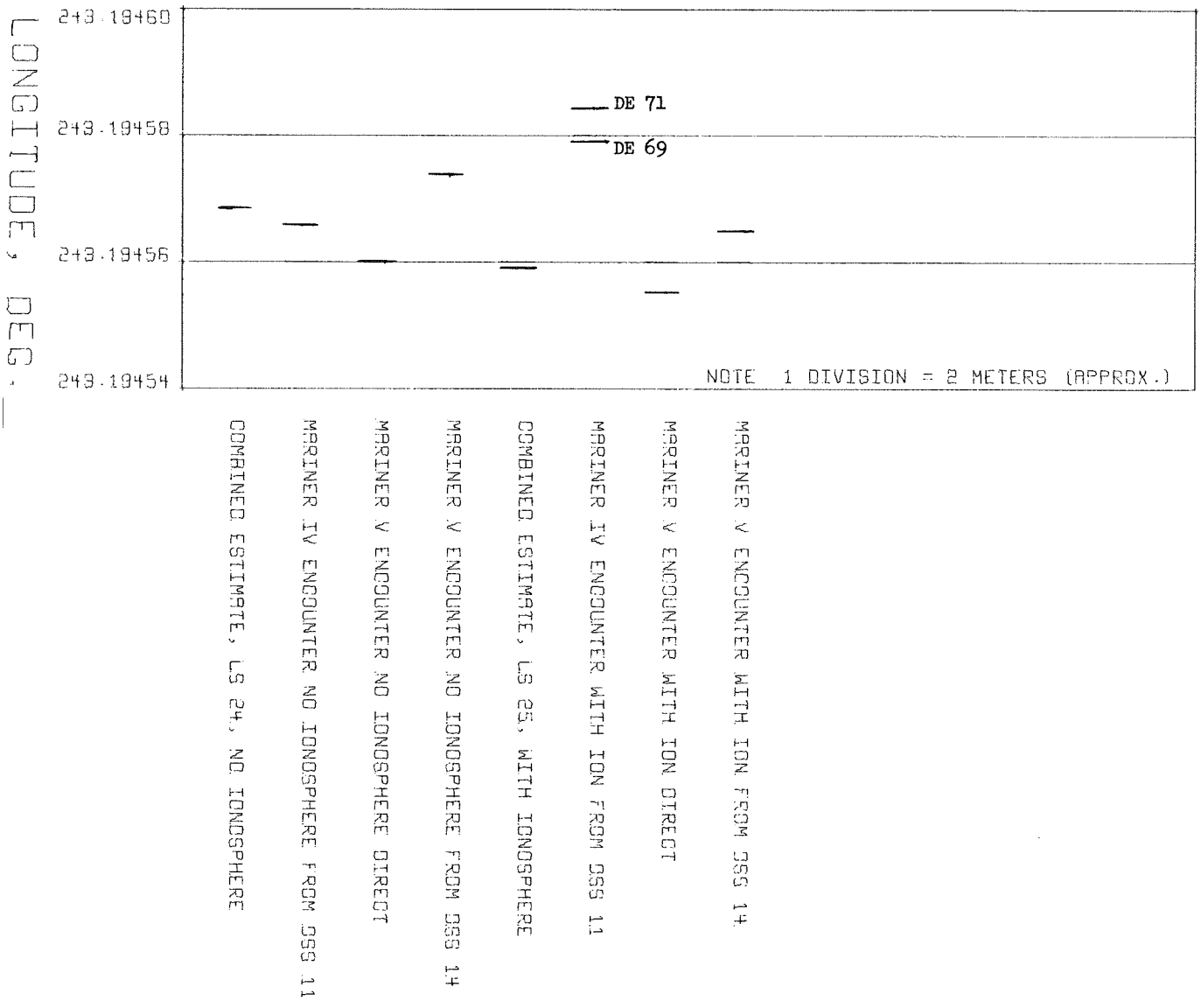

Fig. 34. Geocentric longitude, earth-fixed system (1903.0 pole), DSS 12

Table 21. Difference in station locations, LS 25 (ionosphere) — LS 24 (no ionosphere)

DSS	Δr_s, m	$\Delta\lambda$, 10^{-5} deg[a]	Δ relative longitude (DSS 12 − DSS --)
11	3.8	−0.94	—
12	3.8	−0.94	—
14	3.8	−0.96	—
41	0.26	−3.24	2.3
42	−0.28	−0.32	−0.62
51	−0.61	−0.84	−0.1
61	3.47	−1.04	0.1
62	3.45	−1.08	0.14

[a]See Footnote b, Table 19.

atmosphere. A new fit was made from 15 deg to the zenith for use by *Mariner* Mars 1969 in the DPODP. To check the effects of this new model on the existing station locations, only the *Mariner V* zero-declination cruise case was refitted due to time limitations. The corrections were made in r_s only and range from 0.5 to 0.8 m. They were applied to the spin axis values in LSs 24 and 25 to create sets 27 and 26, respectively. Their general usage is not recommended until the current investigations are completed.

f. Location set uncertainties. The formal statistics produced by the combination program may not be realistic in view of known contributing error sources. An attempt will be made to expand the existing normal matrix from each DPODP reduction by scaling the station location rows and columns by factors to represent different error

Table 22. Absolute locations[a]

DSS	RI, km	ϕ, deg	λ, deg	r_s, km	Z, km	UC, km[b]	VC, km[c]
			LS 24[d]				
11	6372.0084	35.208049	243.150637	5206.3381	3673.763	−2351.4238	−4645.0794
12	6371.9927	35.118672	243.194568	5212.0497	3665.628	−2350.4372	−4651.9789
14	6371.9915	35.244360	243.110523	5203.9951	3677.052	−2353.6156	−4641.3423
41	6372.5561	−31.211425	136.887540	5450.1984	−3302.243	−3978.7193	3724.8430
42	6371.7103	−35.219659	148.981300	5205.3501	−3674.646	−4460.9808	2682.4093
51	6375.5247	−25.739300	27.685441	5742.9410	−2768.744	5085.4416	2668.2683
61	6370.0235	40.238924	355.751018	4862.6043	4114.885	4849.2395	− 360.27414
62	6369.9643	40.263216	355.632211	4860.8141	4116.908	4846.6970	− 370.19224
			LS 25[e]				
11	6372.0115	35.208029	243.150627	5206.3419	3673.763	−2351.4263	−4645.0824
12	6371.9958	35.118652	243.194559	5212.0535	3665.628	−2350.4397	−4651.9819
14	6371.9946	35.244340	243.110513	5203.9989	3677.052	−2353.6181	−4641.3453
41	6372.5563	−31.211423	136.887507	5450.1986	−3302.243	−3978.7174	3724.8454
42	6371.7106	−35.219658	148.981301	5205.3504	−3674.646	−4460.9809	2682.4097
51	6375.5252	−25.739297	27.685432	5742.9417	−2768.744	5085.4425	2668.2678
61	6370.0262	40.238904	355.751007	4862.6078	4114.885	4849.2429	− 360.27527
62	6369.9670	40.263196	355.632200	4860.8176	4116.908	4846.7004	− 370.19342

[a]All location sets at 1903.0 pole. Survey constraints used at Goldstone and Madrid DSCCs.
[b]$UC = r_s \cos\lambda$.
[c]$VC = r_s \sin\lambda$.
[d]*Mariners IV* and *V* with no ionosphere.
[e]*Mariners IV* and *V* with ionosphere.

Table 23. Relative locations

DSS parameter[a]	LS 24		LS 25	
	$\Delta\lambda$	Δr_s	$\Delta\lambda$	Δr_s
DSS 12 — 41	106.307029	−238.1487	106.307052	−238.1451
DSS 12 — 42	94.213264	6.6996	94.213258	6.7032
DSS 12 — 51	215.509128	−530.8913	215.509127	−530.8881
DSS 12 — 61	−112.556449	349.4454	−112.556448	349.4457
DSS 12 — 62	−112.437643	351.2356	−112.437641	351.2359
DSS 41 — 42	− 12.093764	244.8483	− 12.093794	244.8483
DSS 41 — 51	109.202099	−292.7427	109.202075	−292.7430
DSS 41 — 61	−218.863478	587.5940	−218.863500	587.5908
DSS 41 — 62	−218.744671	589.3842	−218.744693	589.3811
DSS 51 — 61	−328.065577	880.3367	−328.065575	880.3339
DSS 51 — 62	−327.946770	882.1269	−327.946768	882.1241

[a]Relative locations for DSS 11 — 12, DSS 12 — 14, and DSS 61 — 62 are listed in Table 24.

Table 24. Relative locations at Goldstone and Madrid tracking complexes[a]

DSS parameters	Δr_s, km	$\Delta\lambda$, deg	ΔZ, km
Goldstone DSCC			
DSS 11 — 12	−5.7117	−0.043931	8.1353
DSS 11 — 14	2.3430	0.040114	− 3.288
DSS 12 — 14	8.0547	0.084046	−11.42364
Madrid DSCC			
DSS 61 — 62	1.7902	0.118807	− 2.0232

[a]Computed from geodetic survey reductions.

sources and adding them to the matrix. All the location sets discussed in this article have had formal statistics of 0.9 to 2.5 m in r_s and 2.5 to 3.0 m in longitude. Using the distribution of the components of the combination as a guide to the uncertainty, one would say that LS 24, the no ionosphere set, should have an uncertainty in r_s of about 5 m based on the worst-case scatter found in the solutions for DSS 12. The longitude solutions only show a scatter of about 1 m. To quote this as an uncertainty for the combined longitude value would not be realistic considering possible ionosphere, ephemeris, and timing effects. Upon examining the ionosphere-corrected reductions and the resulting combination, the shift from LS 24 in r_s at the Goldstone and Madrid DSCCs and the reduction in the scatter show that 5 m may have been a realistic uncertainty in r_s for the non-ionosphere set and, similarly, 2.4×10^{-5} deg in longitude for DE 69. Given a number of solutions in the combination, a reasonable estimate of the uncertainty for the combination appears to be obtainable by observing the worst-case distribution of the constituents. The criteria of the total scatter at Goldstone DSCC would have appeared to produce acceptable uncertainties for LS 24 in view of the results noted when applying the ionosphere to produce LS 25. For the ionosphere-corrected set, uncertainties of about 2.25 m would appear reasonable for r_s based on the scatter at DSS 12. Considering that space plasma and troposphere might still be adversely affecting the solutions, an estimate of 3 m might be more applicable. The longitude would be at about the same level.

The location set recommended for a specific task will depend upon many things. As has been indicated in the text of this article, the timing system, choice of ephemeris, polar motion, troposphere model, and ionosphere corrections are very important parts of the overall earth–solar system model, which strongly influences the derived station location solutions. Of greatest importance are the timing, polar motion, and ephemeris systems used. Before a given location set can be recommended for usage or comparison with other results, an understanding of these systems as they exist is necessary. Differences in certain lunar and planetary ephemeris systems at JPL are one indication of how station locations (longitude) would have to be modified before use.

g. Concluding remarks. It has been demonstrated that an accuracy of 5 m or better was obtained in estimating station locations using the SPODP. The DPODP has been required, though, to carry the solutions below the 5-m level, with its improved data reduction capability and application of the ionosphere corrections. Improved techniques in combining the estimates obtained are helpful in using the output of the DPODP to provide more meaningful location estimates. This same program will also be used as a part of the process to improve the credibility of the uncertainties calculated. There are still areas to be investigated. The lunar-derived locations can hopefully be joined with the planetary, but first the differences appearing in the planetary encounter longitude solutions need to be clearly understood. Improved ionosphere, space plasma, and troposphere corrections are being investigated and will hopefully trim even more of the scatter and uncertainty off the existing solutions.

References

1. Warner, M. R., and Nead, M. W., *SPODP—Single Precision Orbit Determination Program*, Technical Memorandum 33-204. Jet Propulsion Laboratory, Pasadena, Calif., Feb. 15, 1965.

2. Mottinger, N. A., "Breaking the 10 Meter Level in Obtaining Consistent Station Location Solutions From the Reduction of Deep Space Probe Data," presented at the American Geophysical Union Meeting, Washington, D.C., Apr. 23, 1969.

3. Lambeck, K., "Comparisons and Combinations of Geodetic Parameters Estimated From Dynamic and Geometric Satellite Solutions and From Mariner Flights," prepared for XII Plenary Meeting of COSPAR, Prague, May 1969, Smithsonian Institution Astrophysical Observatory, Cambridge, Mass.

4. A Cursory Examination of the Effect of Space Plasma on *Mariner V* and *Pioneer IX* Navigation With Implications for *Mariner* Mars 1971 TSAC,

V. J. Ondrasik, B. D. Mulhall, and N. A. Mottinger

a. Introduction. The tracking system analytical calibration (TSAC) effort is concerned with reducing the effect of various error sources that limit the ability to determine the orbit of a spacecraft using earth-based radio tracking data. One of these error sources is the change in the phase and group velocities of the radio signal as it passes through the charged particles in the earth's ionosphere and the interplanetary medium, the space plasma. Although an intensive effort is in progress to calibrate radio tracking data for the effects of charged particles in the ionosphere, relatively little attention has been paid to the effect of the charged particles in the space plasma. This is due primarily to the extreme scarcity of space plasma data. Two missions that did carry dual frequency experiments, which enable space plasma calibrations to be made, were *Mariner V* and *Pioneer IX*. Selected portions of the tracking data from these two missions have been calibrated and the effects of the space plasma are illustrated in terms of the apparent daily changes in station locations. These results are then used to draw implications concerning the navigational capabilities of *Mariner* Mars 1971 TSAC.

b. Space plasma total electron content. Before space plasma corrections to range and doppler measurements can be made, it is necessary to determine the number of charged particles, and their time rate of change, that the signal encounters along its ray path in the interplanetary medium. This quantity, called the space plasma electron content E_s, may be found very simply from Eq. (1), under the following assumptions:

(1) Any time variations occurring in the time span of the round-trip light time between the earth and the spacecraft are negligible. Note that for typical Venus missions the round-trip light time is less than 10 min.

(2) The difference in path lengths outside the ionosphere between the spacecraft and the various earth-based tracking stations is negligible.

Since the purpose of this article is to determine the magnitude of the effects of space plasma and not to calibrate the tracking data, these assumptions are justified.

$$E_s(t) = E_T(t) - E_I(t) \tag{1}$$

where

$E_T(t)$ = total electron content along the entire ray path, determined from Stanford University dual frequency measurements[11] (SPS 37-58, Vol. II, pp. 66–73) for the *Mariner V* and *Pioneer IX* missions.

$E_I(t)$ = ionospheric electron content along the portion of the ray path in the earth's ionosphere. This quantity may in this case be most conveniently determined by mapping (SPS 37-57,

[11]The principle investigator of the Stanford University dual frequency is Prof. V. R. Eshleman. Members of his team include Drs. T. Howard and T. Croft. The total electron content determined from this experiment was supplied to Dr. L. Efron of JPL, who made it available to the authors.

Vol. II, pp. 38–42) Faraday rotation measurements made at Stanford University to the spacecraft's ray path. This mapping process contains some errors (which will be discussed in a forthcoming article) that will allow E_s to be determined to an accuracy of about 5×10^{16} electrons/m^2, which corresponds to approximately one-half meter in path length change for S-band frequencies.

The small circles in Figs. 35–38 show the space plasma electron content as determined from Eq. (1) along with the corresponding S-band range errors for data acquired from

(1) *Pioneer IX* near zero declination in May 1969.

(2) *Mariner V* in July, August, and September 1967 when there were at least 8 h of data per pass.

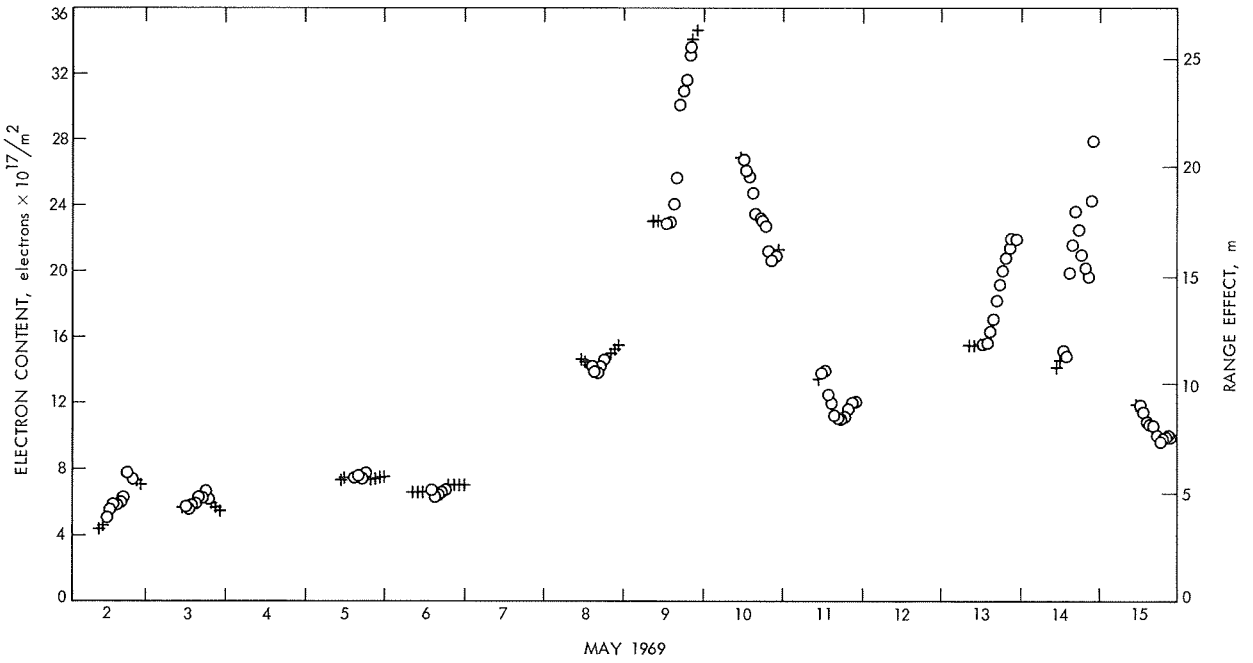

Fig. 35. *Pioneer IX* space plasma electron content and range effect in May 1969

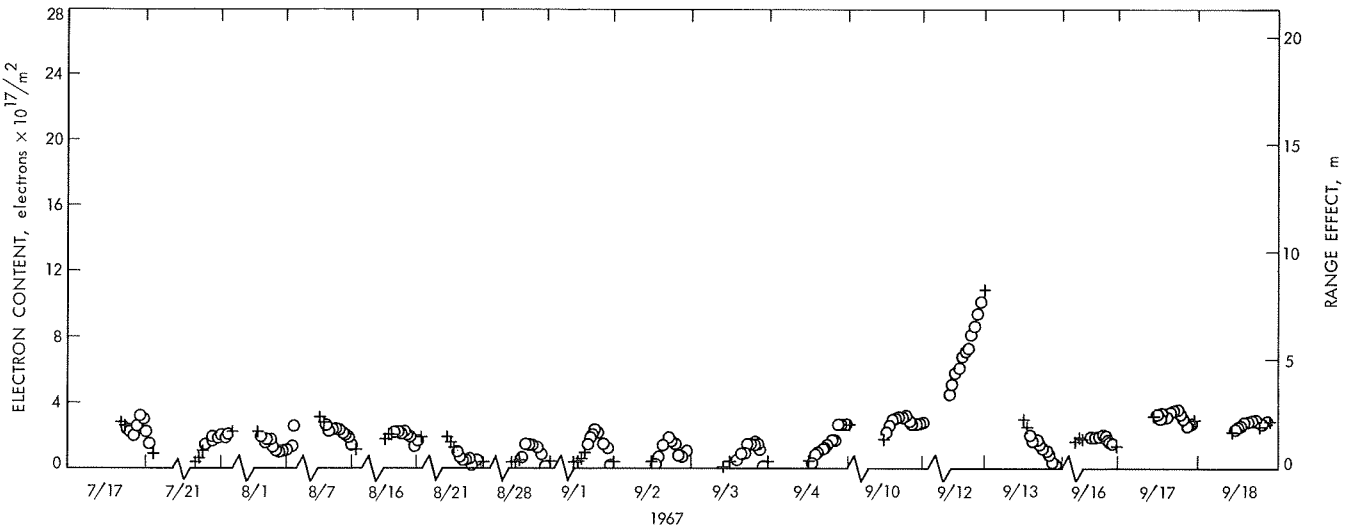

Fig. 36. *Mariner V* space plasma electron content and range effect in Jul, Aug, and Sep 1967

(3) *Mariner V* for the Venus encounter on October 19, 1967 and the surrounding days.

(4) *Mariner V* near zero declination in October and November 1967.

The data from (1), (3), and (4) are particularly useful in determining the tracking station locations, and the data from (3) may be used to determine the encounter trajectory.

Figures 35, 37, and 38 have a continuous time scale and indicate that trying to interpolate the space plasma electron content for approximately half of every day, when the spacecraft is not in view by Stanford University, would often be impossible. This is particularly true during periods of high solar activity, such as occurred

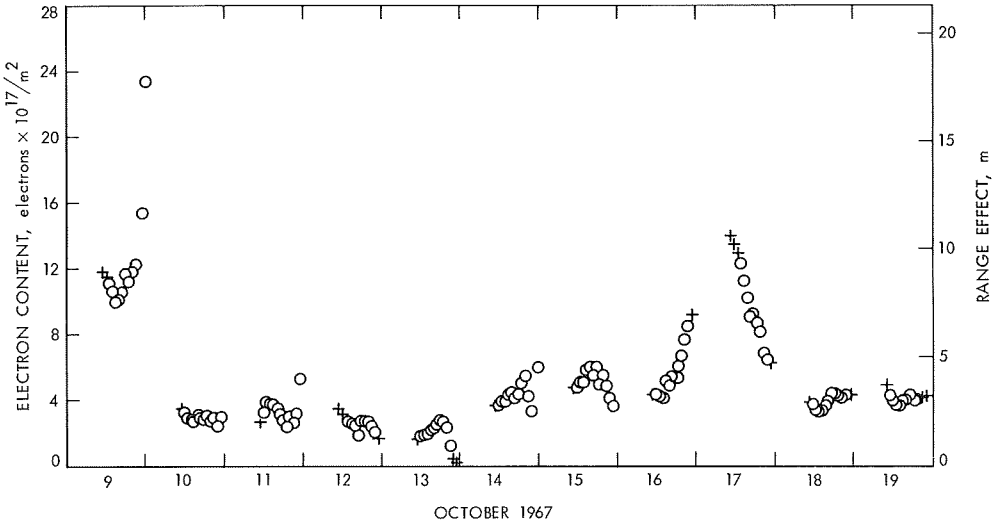

Fig. 37. *Mariner V* space plasma electron content and range effect in Oct 1967

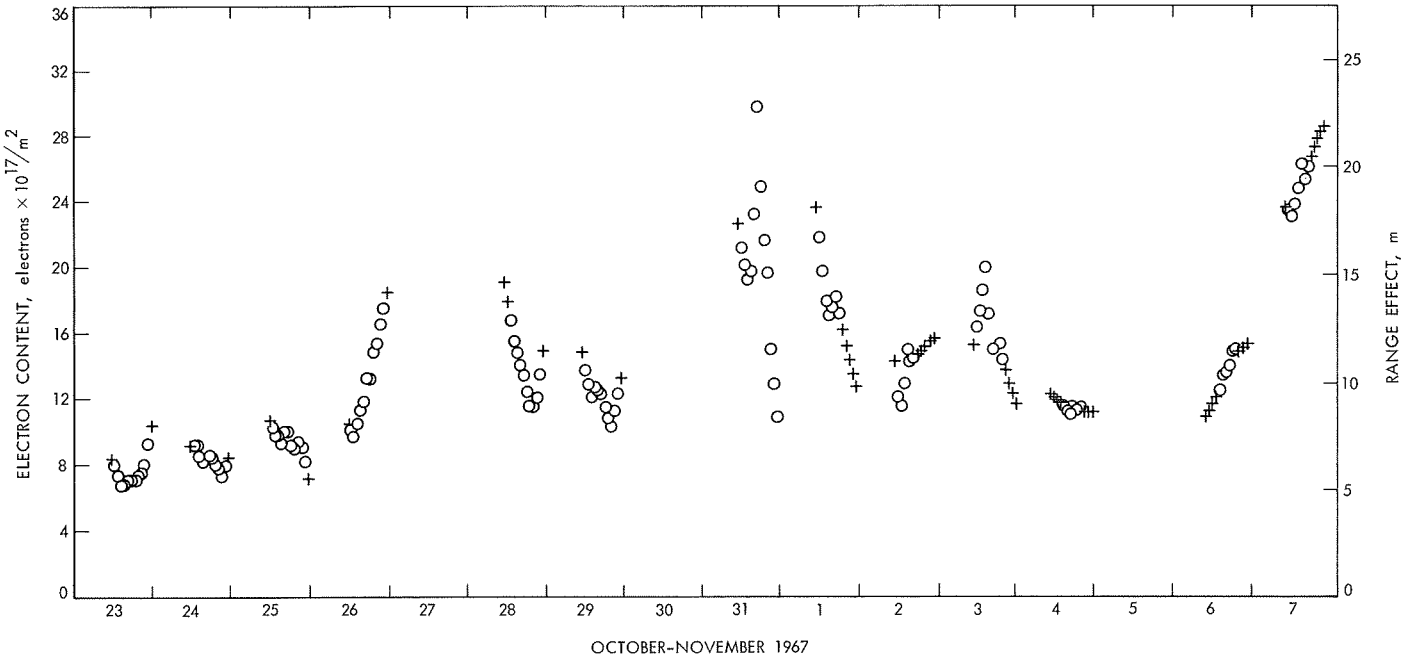

Fig. 38. *Mariner V* space plasma electron content and range effect in Oct and Nov 1967

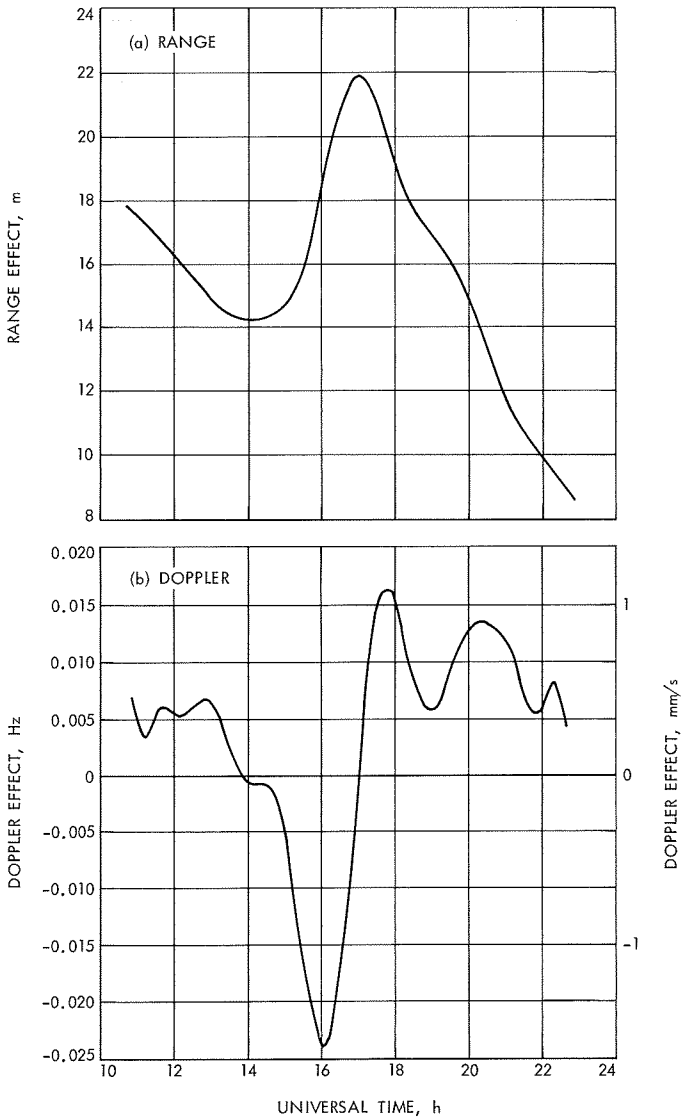

Fig. 39. *Mariner V* space plasma range and doppler effects on Oct 31, 1967

during October–November 1967 and May 1969, when there are many peaks and valleys.

c. Range and doppler space plasma corrections. The software used for this analysis (ION) (SPS 37-58, Vol. II, p. 73) was designed to produce ionospheric range and doppler corrections using measured values of the ionospheric electron content. ION may give inferior results if the electron content measurements do not cover the entire pass. For this reason it was sometimes desirable to extend the real data by estimating the space plasma total electron content at the beginning and end of the tracking pass. These estimated values are shown as crosses in Figs. 35–38. This combination of real and simulated data may be substituted into ION (with the mapping operations peculiar to the ionosphere deleted) to produce range and doppler corrections. Figure 39 shows the computed range and doppler space plasma effects for *Mariner V* on October 31, 1967, which was a day of very high solar activity. It should be noted that the peak values of 22 m in range and −1.6 mm/s in doppler are twice as large as produced by an active ionosphere (SPS 37-57, Vol. II, p. 42).

d. Apparent changes in station locations produced by the space plasma. A useful artifice for investigating the navigational errors is to describe them in terms of errors in tracking station location. As described in SPS 37-57, Vol. II, pp. 24–29, an effect which corrupts tracking data can be decomposed into parameters, one of which is the apparent change in the station distance off the spin axis, Δr_s, and another is the apparent change in the station's longitude, $\Delta\lambda$. The program HAMMEL (SPS 37-57, Vol. II, pp. 24–29) has been developed to obtain these apparent daily changes in station location using the doppler corrections produced by ION.

The apparent daily changes in station locations obtained from HAMMEL for the *Mariner V* and *Pioneer IX* space plasma illustrated in Figs. 35–38 are given in Table 25 and Figs. 40 and 41. Although the *Mariner V* results are generally significantly lower than the ionospheric changes in apparent station locations computed for the same days, of approximately Δr_s (ion) ~5 m and $\Delta\lambda$ (ion) ~3 m (SPS 37-57, Vol. II, p. 34), these numbers were sometimes exceeded as on October 31, 1967. Table 26 gives the percentage of days when the apparent station location changes were above a certain limit, and, in particular for *Mariner V*, shows that for more than 60% of the days either Δr_s or $\Delta\lambda$ is larger than 0.5 m.

Table 27 shows that although the standard deviations of Δr_s and $\Delta\lambda$ are fairly large (1.7 and 3.1 m, respectively, for *Mariner V*), the averages are almost zero. This indicates that over a long period of time the space plasma change in station locations is random, unlike the ionospheric corrections which are usually biased in one direction (SPS 37-57, Vol. II, p. 34). To see if the random character of the change in station locations is maintained over a 10-day period, running averages were calculated for this time scale. The results are given in Fig. 42 and show that a high solar activity, as occurred in late October and early November 1967, can bias the 10-day averages by 1 m. Even deleting the abnormally high days of

Table 25. *Mariner V* apparent station location changes in July, August, and September 1967

Date, 1967	Δr_s, m	$\Delta\lambda$, m
7/17	−1.0	−0.5
7/21	−0.4	−0.5
8/1	1.2	−1.6
8/7	−0.1	1.0
8/16	0	−1.1
8/21	0.4	0.3
8/28	−0.9	0.5
9/1	−1.4	0.5
9/2	−1.2	0
9/3	−0.8	−0.8
9/4	−0.2	0.5
9/10	−0.7	−0.9
9/12	0.3	−0.5
9/13	0.3	0
9/16	−0.3	0
9/17	−0.2	−0.5
9/18	−0.3	−0.2

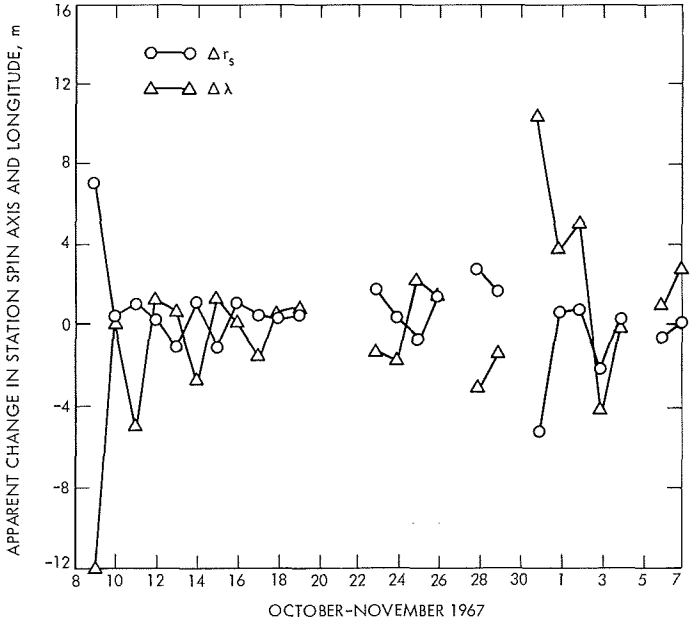

Fig. 40. Apparent changes in station locations for *Mariner V*

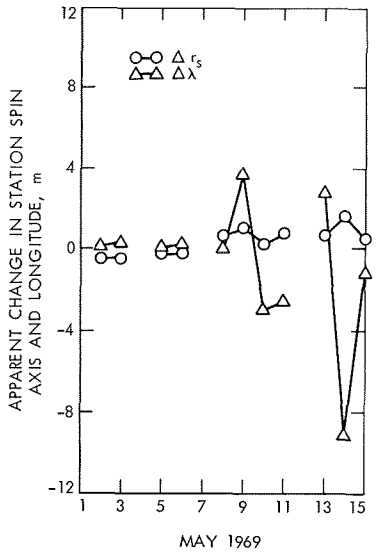

Fig. 41. Apparent changes in station locations for *Pioneer IX*

Table 26. Percentage of days when apparent change in station locations exceeds a certain limit

Limit, m	*Mariner V*[a]		*Pioneer IX*[b]	
	$\lvert\Delta r_s\rvert >$ limit, %	$\lvert\Delta\lambda\rvert >$ limit, %	$\lvert\Delta r_s\rvert >$ limit, %	$\lvert\Delta\lambda\rvert >$ limit, %
0.5	61	68	45	55
1.0	29	52	18	55
1.5	16	35	9	45
2.0	6	23	0	45
3.0	3	13	0	18
5.0	3	6	0	9

[a]For 41 days during July–November 1967.
[b]For 11 days in May 1969.

Table 27. *Mariner V* and *Pioneer IX* average and standard deviations for apparent changes in station locations

Spacecraft	Number of days	Time span	Average		Standard deviation	
			Δr_s, m	$\Delta\lambda$, m	Δr_s, m	$\Delta\lambda$, m
Mariner V	41	Jul 17 to Nov 7, 1967	0	0	1.7	3.1
Pioneer IX	11	May 2 to 15, 1969	0.41	−0.8	0.62	3.2

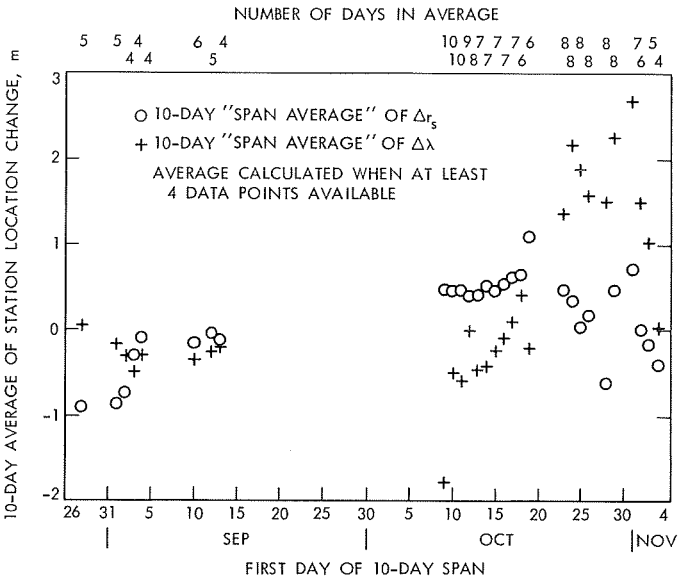

Fig. 42. Ten-day running averages for apparent changes in station locations for *Mariner V* in Jul–Nov 1967

October 9 and 31, 1967, does not significantly improve the averages.

The results of this section may be related to the *Mariner* Mars 1971 mission by using Efron's steady-state model of the solar wind (SPS 37-56, Vol. II, pp. 61–69). This model predicts that a solar activity that produced the apparent changes in station locations shown in Fig. 40 would give changes of a similar size for a *Mariner* Mars 1971 encounter.

e. Summary and implications for Mariner Mars 1971. Although only a cursory examination has been made of a portion of the Stanford space plasma data available from *Mariner V* and *Pioneer IX*, it demonstrates that the space plasma is a potentially limiting effect with regard to the navigational requirements for future missions. For example, the navigational goals for *Mariner* Mars 1971 encounter minus 30 days are to know the effective tracking station locations within 0.8 and 1.6 m in spin axis and longitude, respectively. Assuming there are no other errors, the randomness of the space plasma apparent changes in station locations may allow these goals to be approached without making space plasma corrections, if the sun is not unusually active and a method of determining which data should be deleted is developed. However, for a situation such as a planetary encounter, which has a span of only a few days, so that none of the data may be deleted and the randomness does not help, the data may easily contain a bias on the order of 1 m in effective tracking station locations. Thus, to meet the Mariner Mars 1971 navigational goals, near-real-time space plasma corrections will probably have to be made. This article has shown that simulation runs of the *Mariner* Mars 1971 mission, particularly the encounter sequence, with the data suitably corrupted by a simulated space plasma are certainly justified.

5. An Algorithm for Calculating the View Periods of a Distant Spacecraft, G. A. Madrid

a. Introduction. There are many applications that require an analytical method for determining the time that a distant spacecraft will appear over an observer's horizon and the extent of time that it will remain in view. This type of application often requires that the algorithm employed be embedded in a computer program thereby imposing certain constraints. These are that the algorithm be convenient to use and efficient in operation.

No algorithm permitting such a facile computation of view periods is currently in use. Existing systems that can provide such information are integral parts of large computer programs and therefore could not be suitably implemented for the purposes being considered here. Furthermore, the interface and format requirements are usually sufficiently distinct from those provided by existing systems that information from them must be transcribed onto cards before it can be utilized.

The method presented here exhibits all of the features desired of such an algorithm and, notwithstanding certain simplifying assumptions, produces a remarkably accurate representation of the view periods of a *distant* spacecraft.

b. Method. It is required that the time of rise, time of set, and maximum elevation of a distant probe be calculated analytically, knowing the right ascension α and declination δ of the probe at any time. Assuming that the declination remains fairly constant over the view period[12] and overlooking any correction due to land mask and atmospheric refraction, we can calculate the rise time t_r as

$$t_r = \frac{\alpha + \theta_r - \lambda - p(d)}{\omega}$$

[12]For deep space probes this is practically true after 5 days from launch. For terrestrial or lunar orbiting vehicles this assumption fails, thereby restricting the use of this method.

where

d = number of days from 1950.0

t_r = number of seconds past beginning of day d

α = right ascension of probe on day d, deg

θ_r = hour angle of probe at time of rise, deg

λ = east longitude of observing station, deg

$p(d) = [100° \; 0.0755426 + 0.9856473d + 2.9015 \times 10^{-3}d^2]_{\text{mod } 360}$

ω = rotation rate of earth, deg/day

Values for all of these parameters are known except for θ_r. This parameter can be evaluated by

$$\theta_r = 360° - \cos^{-1}(-\tan\phi \tan\delta)$$

where

ϕ = latitude of observing station

δ = declination of probe on day d

The set time t_s can be readily computed by

$$t_s = t_r + (480)\cos^{-1}(-\tan\phi \tan\delta)$$

and the maximum elevation of the pass $\gamma_{\max}$ can be determined by the well-known relationship

$$\gamma_{\max} = 90° - |\phi - \delta|$$

c. Applications. A program called LOOK, which utilizes this algorithm, has been coded and has successfully produced view periods for *Mariner V* and *Pioneer VII* for use by the program ION[13]. In this application ION required elevation angles for the upleg and downleg of both the first and last radio tracking antenna transmissions. This information was provided by using this algorithm to obtain the geometric view period relationships, then using the distance to the spacecraft to correct for the elapsed light time. In tests the geometric rise and set times computed were within 30 s of the times computed for angular observations by the single-precision orbit determination program (SPODP) (Ref. 1). The maximum elevation was never more than 0.1 deg from the SPODP value and the hour angle and declination at rise were never more than 0.125 deg from the reference values. The SPODP values were, of course, obtained without reference to a land mask (i.e., at the observer's geometric horizon). If land mask is taken into consideration, there would be a difference of about 10 to 15 deg in elevation at rise. Such corrections could easily be incorporated into the algorithm if a closer correspondence to the real world were desired.

[13]The program ION (Mulhall, SPS 37-58, Vol. II, pp. 66–73), which provides the capability to calibrate tracking data for ionospheric effect based on either ionosonde data, Faraday rotation measurements or model of the ionosphere, requires the calculation of view periods. An analysis of the errors introduced in ION through the use of this algorithm is presented in the following article (*Subsection 6*).

Reference

1. Warner, M. R., Nead, M. W., and Hudson, R. H., *The Orbit Determination Program of the Jet Propulsion Laboratory*, Technical Memorandum 33-168. Jet Propulsion Laboratory, Pasadena, Calif., Mar. 18, 1964.

6. The Effect of Interpolation on Ionospheric Calibration,

G. A. Madrid

a. Introduction. One of the aims of the Precision Navigation Project (PNP) was to improve the estimates of the DSN station locations for the *Mariner* Mars 1969 mission. In accordance with this aim, Mulhall has developed several techniques to calibrate the radio tracking data so as to remove the effects of charged particles in the ionosphere. One of these methods is embodied in the computer program ION developed by Mulhall and Thuleen (SPS 37-58, Vol. II, pp. 66–73). This method requires as inputs the hour angle and declination[14] of the spacecraft at the beginning of each pass in order to map the ionospheric data to the spacecraft ray path. The correction to the ray path used by this program was derived from a relationship developed by Cain and Liu[15] relating range corrections as a function of the elevation angle. Since the hour angle and declination are obtained by interpolation, any error will be propagated into the calculation of the elevation angle and therefore into the range correction.[16]

[14]The program LOOK, which uses a simplified view period calculation developed by the author, provides these inputs to ION. A description of the view period algorithm is described in the previous article, *Subsection 5*.

[15]Cain, D., and Liu, A., *Ionospheric Range and Angular Correction*, Mar. 23, 1966 (JPL internal document).

[16]It is assumed that a light time correction has been applied to obtain the correct elevation angles and that any errors from this process are negligible.

b. Effects. For a Chapman ionosphere, the elevation angle effect can be expressed as

$$\Delta\rho_I = G_1 + G_2Z + G_3Z^2 + G_4Z^3 + G_5Z^4 \qquad (1)$$

where

$\Delta\rho_I$ = range correction, m

$Z = (\pi/2 - \gamma)$

γ = elevation, rad

The error in the slant range correction is related to an error in the elevation angle by

$$\epsilon_{\Delta\rho} = (G_2 + 2G_3Z + 3G_4Z^2 + 4G_5Z^3)\epsilon_Z \qquad (2)$$

where $\epsilon_Z = -\epsilon_\gamma$ = an error in the elevation angle.

Selecting the coefficients G_1 through G_5 to represent a "heavy" electron situation (i.e., 5.0×10^{17} electrons/m^2) and finding that the range correction reaches a maximum at $\gamma = 0$ deg, it can be stated that

$$|\epsilon_{\Delta\rho}|_{\max} \leq |G_2 + 2G_3Z + 3G_4Z^2 + 4G_5Z^3|_{\max} |\epsilon_Z|_{\max}$$
$$\leq 28.625 |\epsilon_Z|_{\max} \qquad (3)$$

The error in elevation ϵ_Z is related to errors in hour angle and declination. An error in hour angle is directly related to an error in right ascension:

$$\theta = \alpha_G - \alpha + \lambda$$

where

α_G = right ascension Greenwich

α = right ascension probe

λ = longitude of observer

Thus,

$$|\epsilon_\theta| = |\epsilon_\alpha|$$

The relationship between the elevation parameter Z, the right ascension of the probe α, and the declination of the probe δ is such that

$$\epsilon_Z^2 = \epsilon_\alpha^2 + \epsilon_\delta^2$$

From this it follows that

$$|\epsilon_Z|_{\max} = [(\epsilon_\alpha^2)_{\max} + (\epsilon_\delta^2)_{\max}]^{1/2} \qquad (4)$$

Now $(\epsilon_\alpha)_{\max}$ and $(\epsilon_\delta)_{\max}$, the interpolation errors in right ascension and declination, can be determined directly from numerical relationships to be

$$(\epsilon_\alpha)_{\max} = \frac{(t_1 - t_0)^2}{8} K_\alpha$$

$$(\epsilon_\delta)_{\max} = \frac{(t_1 - t_0)^2}{8} K_\delta$$

where K is the curvature at a local maximum or minimum point along the locus of the function of right ascension or declination with respect to time, and $t_1 - t_0$ is the interpolation interval.

Figure 43 shows the locus of the right ascension and declination histories for *Mariner V*. Table 28 lists the maximum interpolation errors at the critical segments of these curves. These segments are numbered 1, 2, 3, and 4. At 5-day intervals, the largest of these maximum values are $(\epsilon_\alpha)_{\max} = 0.09$ deg and $(\epsilon_\delta)_{\max} = 0.07$ deg.

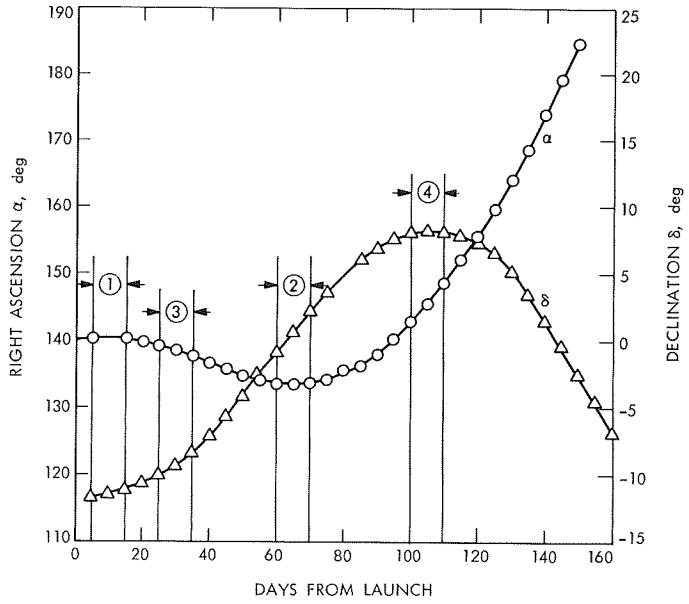

Fig. 43. *Mariner V* right ascension–declination plotted from post-flight trajectory characteristics

Table 28. Interpolated errors in right ascension and declination at critical positions in *Mariner V* trajectory

Interval, days	Days from launch	Position	Parameter	Maximum interpolation error, deg
10	10	1	α	0.220
	65	2	α	0.170
	30	3	δ	0.100
	105	4	δ	0.120
5	7	1	α	0.090
	12	1	α	0.001
	67	2	α	0.040
	72	2	α	0.060
	27	3	δ	0.030
	32	3	δ	0.070
	102	4	δ	0.030
	107	4	δ	0.030
2	9	1	α	0.010
	11	1	α	0.006
	64	2	α	0.009
	66	2	α	0.017
	29	3	δ	0.004
	31	3	δ	0.004
	104	4	δ	0.005
	106	4	δ	0.004

By substituting these values in Eq. (4) and then using this result in Eq. (3), a bound for the error in the range correction can be determined to be

$$\left| \epsilon_{\Delta\rho} \right|_{\max} \leq 0.06 \text{ meters}$$

Utilizing the same procedure, the corresponding result for *Mariner VII* is

$$\left| \epsilon_{\Delta\rho} \right|_{\max} \leq 0.0012 \text{ meters}$$

Figure 44 illustrates the right ascension and declination history for *Mariner VII*. Because the curves are smoother (curvature is smaller) than the *Mariner* V data, it is to be expected that the latter will exhibit larger interpolation errors than the former. This is borne out by the results stated above.

c. Conclusions. The PNP goals for 1969 call for a range resolution capability of 0.1 m in the calibration of the ionospheric effect. According to this criterion, the maximum interpolation error at 5-day intervals of 0.06 m

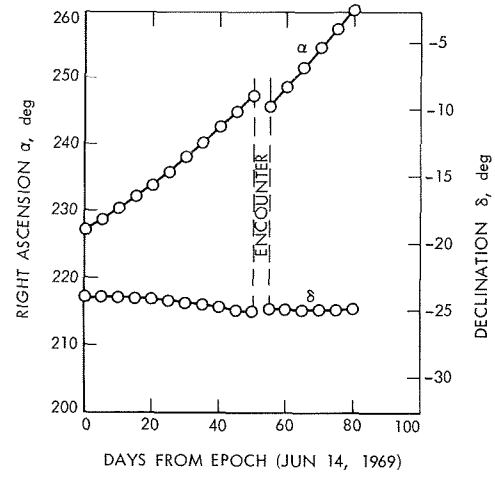

Fig. 44. *Mariner VII* right ascension–declination plotted from post-flight trajectory characteristics

introduced in calibrating the *Mariner V* tracking data falls within these requirements and can therefore be considered an acceptable error. The *Mariner VII* 5-day interpolation error of 0.0012 m is clearly acceptable.

7. The Use of Sequential Estimation With DSN Tracking Data for a Planetary Orbiter, *J. F. Jordan and R. K. Russell*

a. Introduction. With the advent of technical studies on the feasibility of planetary orbiter missions, such as the *Mariner* Mars 1971 orbiter mission and the *Viking* 1973 Mars orbiter/lander mission, JPL has become increasingly aware of the difficulties of determining accurately the orbit of a spacecraft placed as an artificial satellite of a distant planet from DSN range-rate and ranging data.

Some of the unique features of this orbit-determination problem which contribute to the difficulty are: (1) the nonlinearity of the equations of motion of the probe in orbit; (2) the lack of complete knowledge of the physical model involved, e.g., the planet's gravitational model and surface features, atmospheric drag effects, and nongravitational spacecraft-generated forces; and (3) the absence of appreciable position parallax due to the distance from which measurements are made.

For the past year, JPL has been engaged in research directed at developing a sufficient planetary orbiter navigation capability. The research has included the investigation of the feasibility of using current software tools for the task, defining the problem areas resulting from

their use, and the investigation of new state estimation techniques which may circumvent these problems.

One such technique is the sequential data filtering concept. In order to investigate the possibilities of this technique, the sequential orbit determination (SOD) program has been developed. The program is designed primarily for sequential state estimation of a planetary satellite using earth-based range and range-rate observations. The primary goals of the program production results will be aimed at (1) making recommendations (using the results of simulation studies) for the formulation of the sequential filter option to be implemented into the double-precision orbit determination program (DPODP), and (2) influencing (using the results of inherent accuracy studies) the trajectory and guidance maneuver planning in future planetary satellite missions.

The immediate tasks to be performed with the program are as follows:

(1) Conduct a tracking strategy study to determine the most favorable time during the orbit to take data if a given tracking time is alloted.

(2) Perform a definitive study on the sensitivity of the inherent estimation accuracies to the values of the orbital parameters, i.e., the orbit shape and position relative to earth.

(3) Investigate the effects of the nonlinearity of the equations of motion of the orbiting spacecraft on the linear estimation scheme and note the sensitivities of the effects to the orbit parameters.

(4) Investigate the effects of uncertainties in the gravitational model of the planet on the accuracy of the filtering procedure. Look at both harmonic uncertainties and surface anomalies (mascons). Note the sensitivities of the effects to the orbit parameters.

(5) Attempt simple methods for adjusting the filtering routine to accommodate the errors due to the effects investigated in tasks (3) and (4). Examine the use of the process noise concept and the feeding of uncertainty into the planetary mass for keeping the filter gain large.

(6) Attempt more sophisticated methods for adjusting the filtering algorithm. Examine and compare the suitability of several methods, including the limited memory filter concept and the adaptive filter concept, for the planetary orbiter problem.

(7) Examine the suitability of nonlinear extensions to the filtering routine.

(8) Investigate the advantages of increasing the dimension of the estimated state vector to include uncertain model parameters.

The purpose of this and subsequent articles is to report the progress made while carrying out the tasks listed above. Included here is a discussion of the program structure, the coordinate systems and input–output options, and the filtering equations. Results of the first task, the tracking strategy study, are presented for both the 12- and 33-h orbits of the *Mariner* Mars 1971 mission.

b. SOD program structure and description. A description of the input–output options and major functions of the program (see Fig. 45) is as follows:

(1) The initial simulated and estimated spacecraft states and *a priori* covariance matrix of the error in the estimated state can be introduced in the following systems:

(a) Cartesian, earth equatorial.

(b) Cartesian, plane-of-the-sky (see Fig. 46).

(c) Orbital elements, earth equatorial.

(d) Orbital elements, plane-of-the-sky (see Fig. 46).

The position and velocity of the target body relative to the earth in cartesian coordinates can be stated in plane-of-the-sky or earth equatorial systems. The position of the earth tracking station is an input to the program in cylindrical, earth equatorial coordinates.

(2) The program maps the simulated state $(\bar{x}_a, \bar{v}_a)$ and estimated state $(\bar{x}, \bar{v})$ of the spacecraft between points in time in target-centered, plane-of-the-sky cartesian coordinates. The vector equations of motion are

$$\dot{\mathbf{v}} = -\frac{\mu}{r}\mathbf{x}$$

$$\dot{\mathbf{x}} = \mathbf{v}$$

where μ is the mass of the central body. (Note that the simulated state is mapped with the simulated μ, while the estimated state is mapped with the estimated μ.)

(3) The covariance matrix, Λ, of errors in the estimated state and gravitational mass μ is mapped by

$$\frac{d\Lambda}{dt} = F\Lambda + \Lambda F^T + Q$$

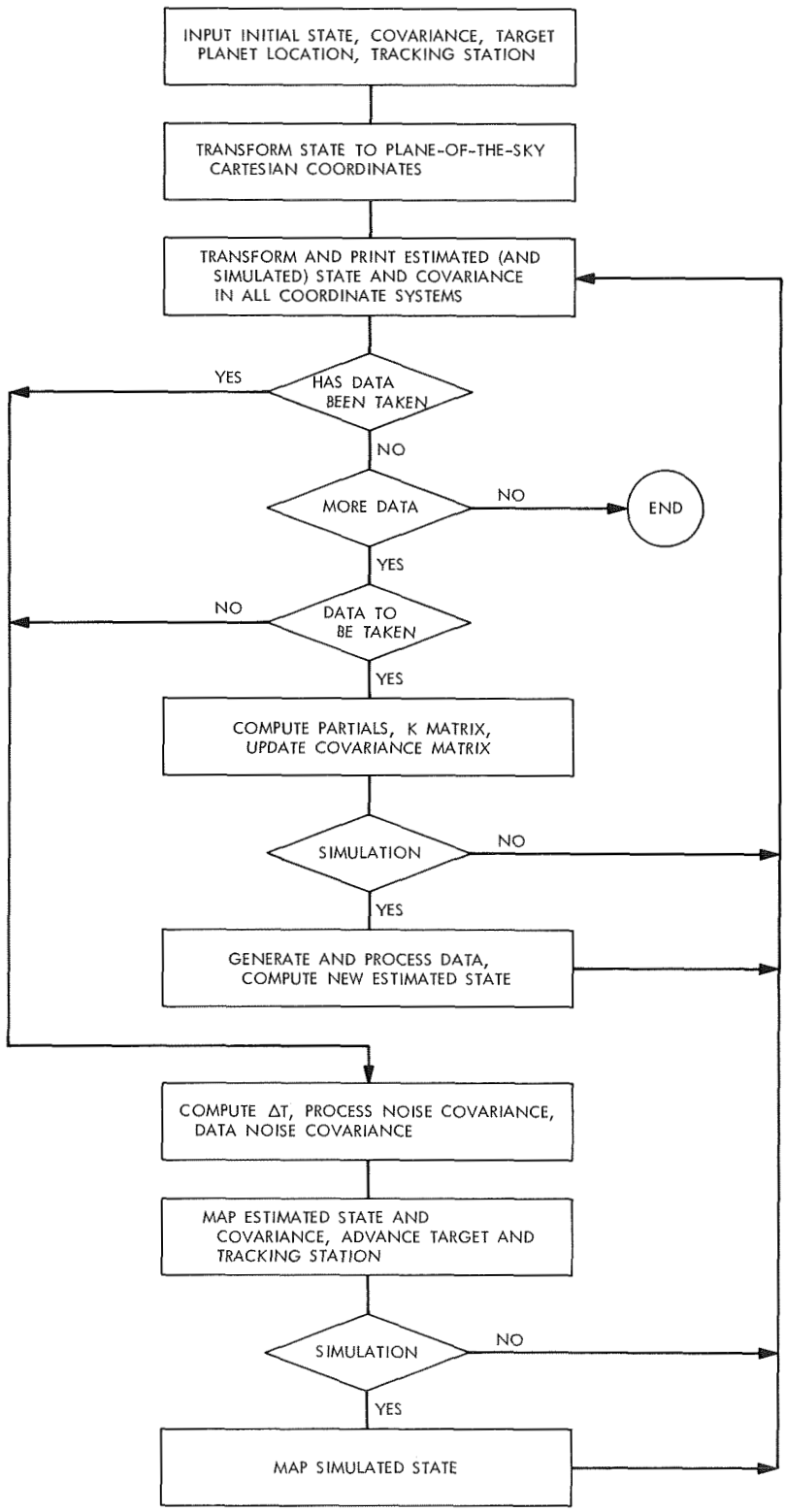

Fig. 45. SOD program flow chart

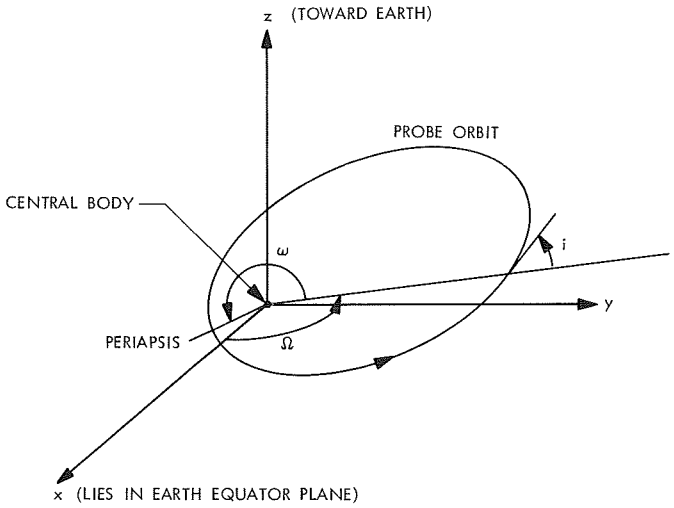

Ω = LONGITUDE OF ASCENDING NODE (MEASURED IN x-y PLANE)

ω = ARGUMENTS OF PERIAPSIS (MEASURED IN ORBIT PLANE)

i = INCLINATION OF ORBIT PLANE TO PLANE-OF-THE-SKY

x-y PLANE IS THE PLANE-OF-THE-SKY

Fig. 46. Orbit configuration referenced to plane-of-the-sky

where

$$F = \frac{\partial\left(-\frac{\mu}{r^3}\mathbf{x}, \mathbf{v}, 0\right)}{\partial(\mathbf{v}, \mathbf{x}, \mu)}$$

and Q is a symmetric matrix representative of the covariance of any assumed "white noise" type of accelerations on the probe (including both gravitational and nongravitational accelerations).

(4) The tracking observables $\dot{\rho}_a$ (range rate) and ρ_a (range) are generated directly from the simulated state. The observables are assumed corrupted by independent gaussian noise increments, and the observable vector z_a becomes

$$z_a = \begin{bmatrix} \dot{\rho}_a \\ \rho_a \end{bmatrix} + \begin{bmatrix} \eta_1 \\ \eta_2 \end{bmatrix}$$

η_1 and η_2 are simulated by a random number generator which yields the following statistics:

$$E[\eta_1] = E[\eta_2] = 0$$

$$E[\eta_1(t_i)\eta_1(t_j)] = \sigma^2_{\eta_1}\,\delta_{ij}$$

$$E[\eta_2(t_i)\eta_2(t_j)] = \sigma^2_{\eta_2}\,\delta_{ij}$$

$$E[\eta_1(t_i)\eta_2(t_j)] = 0$$

The estimated tracking observables $\dot{\rho}$ and ρ are computed directly from the estimated state.

(5) A new state estimate is formed at each point of observation, which can be as often as desired. The new state estimate X_+, where

$$X = \begin{bmatrix} \mathbf{x} \\ \mathbf{v} \end{bmatrix}$$

is computed from the old estimate X_- by the equation

$$X_+ = X_- + K[z_a - z]$$

where z is the estimated observable vector

$$z = \begin{bmatrix} \dot{\rho} \\ \rho \end{bmatrix}$$

and K, the gain matrix, is given by

$$K = \Lambda_- H^T[H\Lambda_- H^T + R]^{-1}$$

with

$$\Lambda_- = E[(X_a - X_-)(X_a - X_-)^T]$$

$$H = \frac{\partial z}{\partial X_-}$$

$$R = \begin{bmatrix} \sigma^2_{\eta_1} & 0 \\ 0 & \sigma^2_{\eta_2} \end{bmatrix}$$

The updated covariance matrix Λ_+, defined as

$$\Lambda_+ = E[(X_a - X_+)(X_a - X_+)^T]$$

is then computed from the old covariance matrix by

$$\Lambda_+ = (I - KH)\Lambda_-(I - KH)^T + KRK^T$$

(6) The output from the program consists of the simulated and estimated states, the matrix of the partials of the observables, the mapping matrix, and the covariance of the error in the estimated state before and after each data point, or as often as specified. In addition these quantities are also mapped and displayed in all coordinate systems referenced in subparagraph (1).

c. Mariner Mars 1971 tracking strategy study. In line with the tasks mentioned above for this program, a tracking data strategy study has been performed that examines questions relating to the orbiter portion of the *Mariner* Mars 1971 mission.

The purposes of this study are:

(1) To determine the relative importance of data spans taken at different intervals of an eccentric orbit.

(2) To recommend a suitable tracking strategy contingent upon requirements of a limited amount of available tracking time.

To study the first problem, two orbits typical of those being considered for the *Mariner* Mars 1971 orbiter were chosen for investigation. Their characteristics in plane-of-the-sky orbital elements follow:

Parameter	Orbit 1	Orbit 2
Period p, h	12	33
Semi-major axis a, km	12651	24862
Eccentricity e	0.58	0.8
Inclination to plane-of-the-sky i, deg	69	85
Argument of periapsis ω, deg	200	220
Longitude of ascending node Ω, deg	111	136

The assumptions of the program's operation are:

(1) Range rate data only, with a noise of 10^{-3} m/s.

(2) A sample interval of 60 s.

(3) Sphericity of Mars is assumed, and accordingly no process noise perturbing the estimated state.

(4) Six probe-state parameters and the mass of the central body are estimated.

(5) The *a priori* covariance of the errors in the state are

$$\sigma_a = 100 \text{ km}$$
$$\sigma_e = 0.1$$
$$\sigma_{T_p} = 100 \text{ s}$$
$$\sigma_\Omega = 1 \text{ deg}$$
$$\sigma_\omega = 1 \text{ deg}$$
$$\sigma_i = 1 \text{ deg}$$
$$\sigma_\mu = 10 \text{ km}^3/\text{s}^2$$

where T_p is the time of periapsis passage.

(6) The earth station is assumed to be at the center of the earth. During the course of this study, it was ascertained that station location and station motion had no effect on the subsequent results, since estimated state was target-centered.

Sensitivity of estimation accuracies to placement of the data span. In order to investigate the tracking strategy problem, it was decided to take a fixed amount of data in the orbit and observe the influence on the estimation capability of varying the portion of the orbit where these data were taken. In addition it should be mentioned that two successive orbit passes of data are used instead of one pass, since the estimation capability is significantly improved by using the additional pass of data. In the following results, the length of the data span is fixed at 4 h.

The plots in Fig. 47 display respectively, in polar form, the uncertainty in the estimates of the semi-major axis and eccentricity as a function of the time of the center of the data span from periapsis for Orbit 1.

It is easily seen that data spans including periapsis offer the best determination of the parameters. For example, for a span taken about periapsis, $\sigma_a = 0.036$ km, while for a span centered about a time 4 h before periapsis, $\sigma_a = 0.26$ km; an order of magnitude difference exists between the two results although the same tracking time span was employed.

Figure 48 illustrates the tracking accuracies of a and e for Orbit 2. The same conclusions can be drawn from the Orbit 2 results, namely, that data spans including periapsis provide the best determination of a and e. In Orbit 2 it is seen that the data spans at periapsis provide a relatively greater determination of the estimated parameters than in Orbit 1. This is due to the higher eccentricity of Orbit 2.

It should be noted that the remaining orbital elements exhibit similar behavior to the semi-major axis.

Sensitivity to variation in the tracking span. Since it has been concluded that tracking centered about the periapsis time is the most efficient general tracking strategy, it would be interesting to note the sensitivity of the parameter estimate uncertainties to the width of the pass.

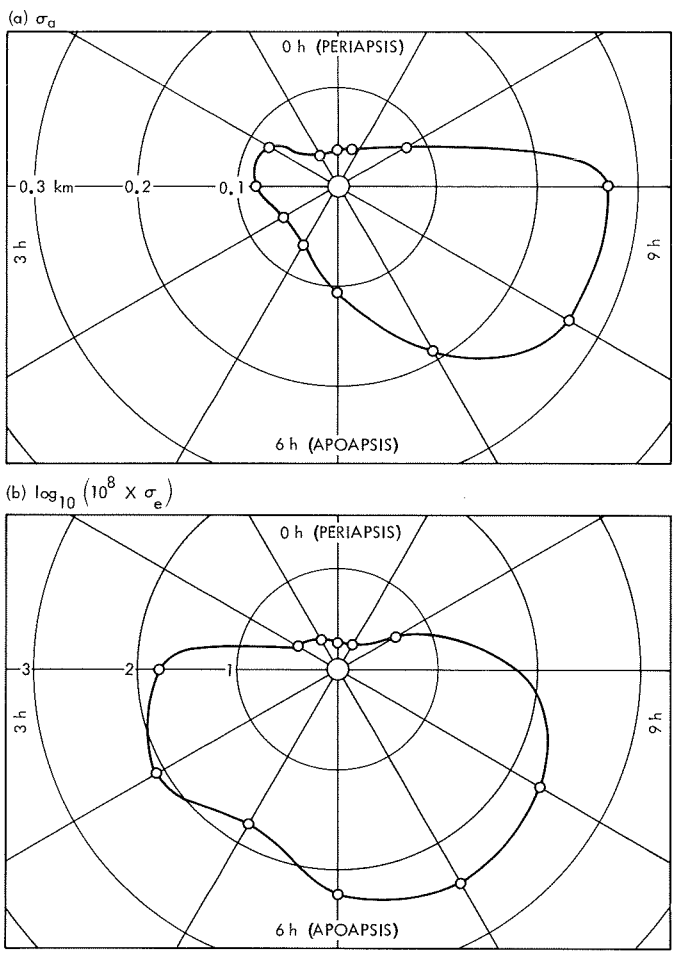

Fig. 47. Uncertainties of semi-major axis and eccentricity for Orbit 1

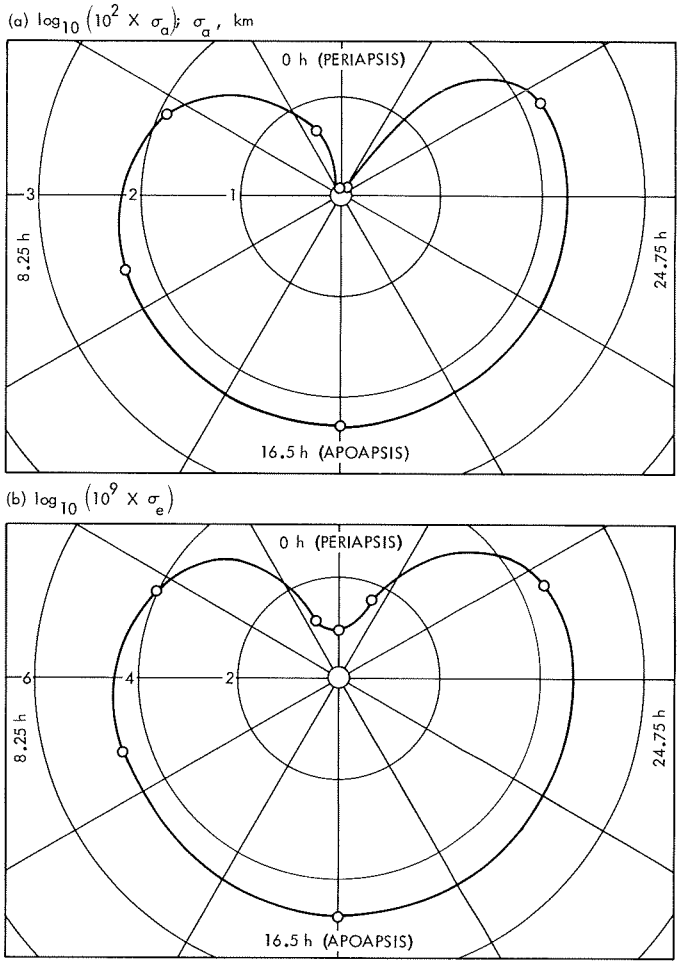

Fig. 48. Uncertainties of semi-major axis and eccentricity for Orbit 2

Plots of the uncertainties in a and e versus the pass width time are presented for Orbit 1 in Fig. 49, with curves shown for both one and two passes. The uncertainty in the semi-major axis appears to level off at a value of 35 m, while the eccentricity has an uncertainty of 0.18×10^{-7}. Plots of the same parameters for Orbit 2 are presented in Fig. 50. σ_a reaches a value of 10 m, while σ_e is just under 10^{-8}. The uncertainties in the other orbital elements behave similarly to those shown and reach the following values:

Parameter	Orbit 1	Orbit 2
σ_{T_p}, s	0.21×10^{-3}	0.16×10^{-3}
σ_Ω, rad	0.9×10^{-5}	0.66×10^{-5}
σ_ω, rad	0.7×10^{-7}	0.5×10^{-7}
σ_i, rad	0.57×10^{-5}	0.42×10^{-5}

Conclusions of the tracking strategy study. The results indicate that the most efficient tracking strategy is the tracking of the probe over spans that are centered about or at least include the periapsis time. It also appears that if more than 1 pass is taken, the parameter uncertainties are not very sensitive to the span width when it is wider than about 4 h.

It should be cautioned that the results presented in this article are idealized in the sense that a spherical central body was assumed with no effects of oblateness considered. The consideration of oblateness effects and harmonic uncertainties will no doubt affect the numerical results presented here, but it is doubtful if the presence of these and other error sources will affect the tracking strategy conclusions stated above, if the orbit determination process effectively accounts for the error sources. As nonlinear and gravitation model error effects are investigated in future work, the results of these investi-

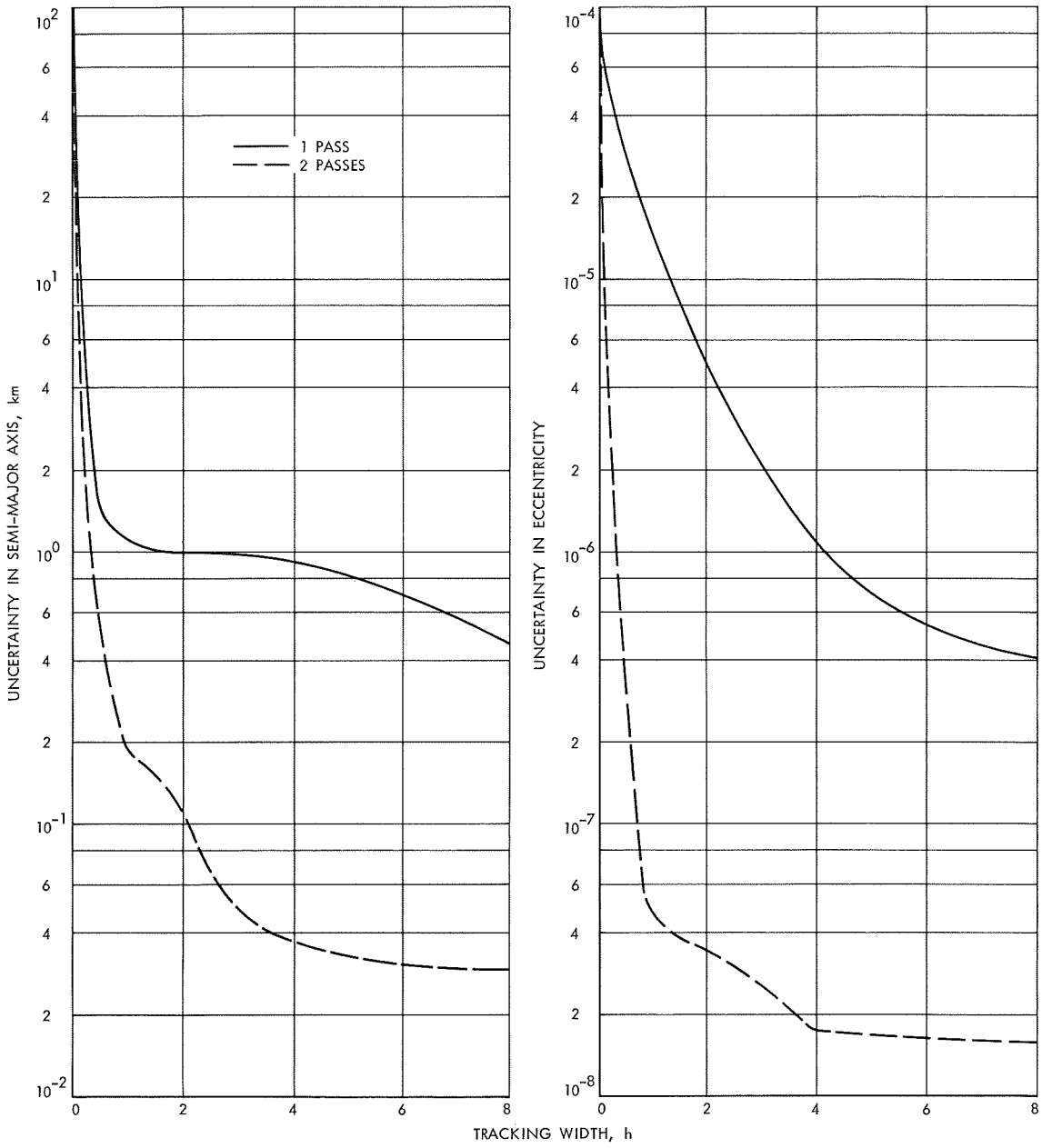

Fig. 49. Uncertainties of semi-major axis and eccentricity as a function of tracking interval width for Orbit 1

gations and their bearing on the conclusions of this article will be published.

8. Lunar Surface Mass Distribution Map From Dynamic Point-Mass Solution, *P. M. Muller and W. L. Sjogren*

a. Introduction. For over one year, JPL and the Aerospace Corporation of El Segundo, California, have been cooperating in an effort to determine lunar gravimetry from a dynamic fit of the *Lunar Orbiter* doppler tracking data, using a dense grid of discrete mass points on the lunar surface. This method differs in fundamental respects from that used in the previous analysis (Ref. 1).

In the original reductions of *Lunar Orbiter* data (Ref. 1 and SPS 37-53, Vol. II, pp. 10–15), the line-of-sight accelerations were inferred by differentiating the residuals after the fit to the doppler tracking data. The many simplifications necessary to this method were stated in Ref. 1. While the data reduced in this way had a high degree of qualitative information, it was always suspected

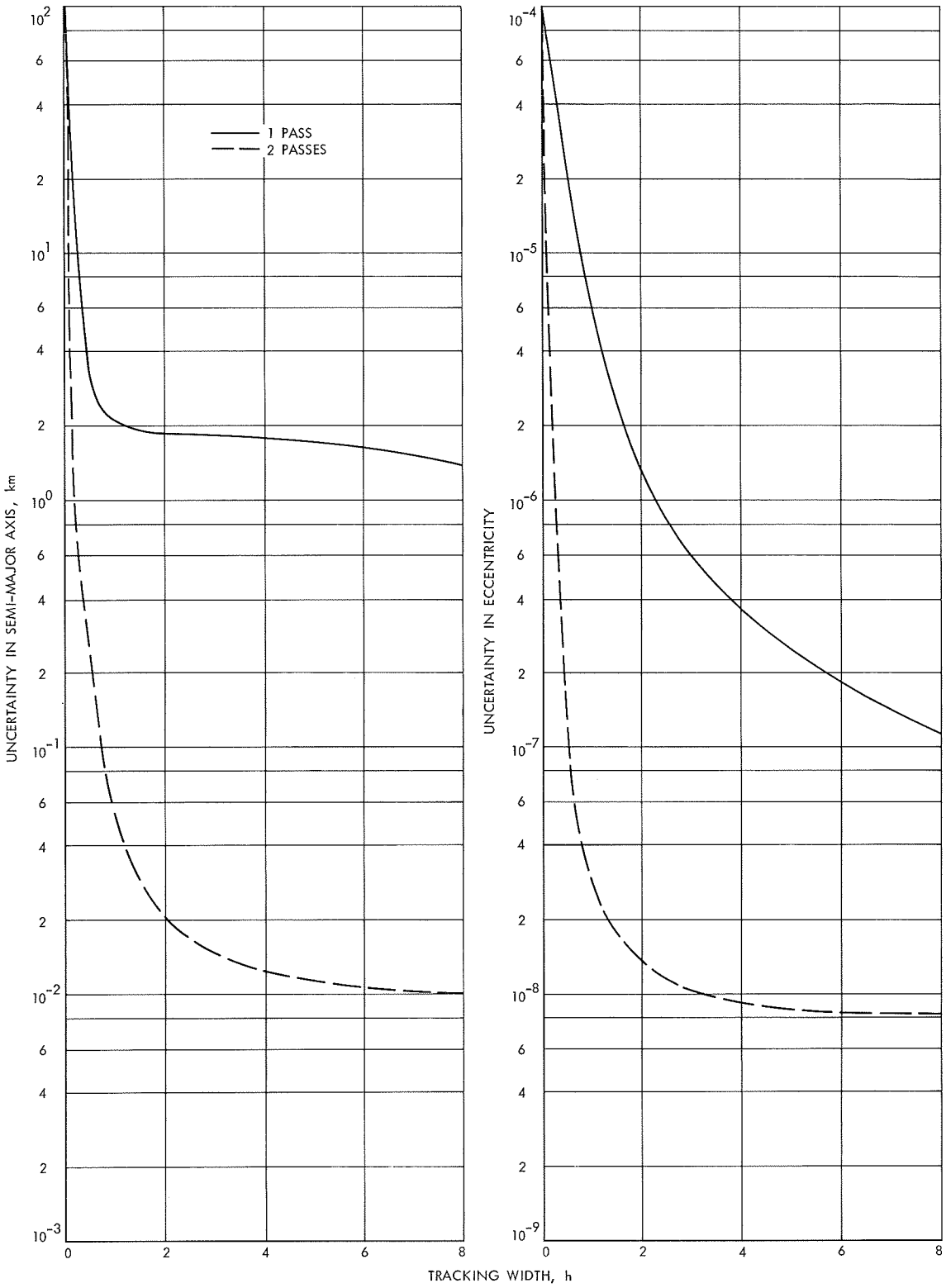

Fig. 50. Uncertainties of semi-major axis and eccentricity as a function of tracking interval width for Orbit 2

that a dynamic determination (either via harmonic expansions, point masses, or a combination) would eventually supersede the initial results. The Aerospace team, direct by L. Wong, and in cooperation with the authors and P. Gottlieb of JPL, has completed the determination[17] using over 100 orbits of *Lunar Orbiter IV* and *V* polar-orbit data. While it is expected that the inclusion of a like amount of equatorial orbit data (*Lunar Orbiters I, II,* and *III*) in subsequent work will change the results slightly, it is deemed appropriate to present the new map at this time.

b. Method. A brief description of the method is presented here. Some 580 discrete mass points were set at the lunar surface, spanning $\pm 90°$ in longitude and $\pm 55°$ in latitude. The separation of individual points at the equator was 5°, increasing to 10° in latitude at 55°N lat, such that correlation between the "solved-for" masses at adjacent points were approximately 0.8[18] given the geometry of *Lunar Orbiter V* polar orbits. These orbits reach perilune at the equator with an altitude of approximately 100 km, increasing with increasing latitude (eccentricity = 0.27). This results in the spacecraft traveling over the surface of the moon (within the region where the doppler tracking data is sensitive to the local lunar surface mass distribution) for 55 min out of each orbital period of 220 min.

A total of 121 orbits was processed individually, solving for the spacecraft state associated with each 55-min data arc centered on the equator. The program was capable of solving 100 parameters, which were usually apportioned to 8 spacecraft data arcs (48 state parameters) and approximately 50 mass points falling under the selected family of data arcs. Groups of orbits processed in this way were overlapped, with the families of mass points in the solve-for set similarly shifted. The solution converged after some 50 computer runs, in which previously solved mass points (not in the solution set of a given run) were included in the trajectory integration. This "bootstrapping" system was the result of an extensive correlation and sensitivity analysis carried out by the Aerospace team.

c. Results. The 580 mass points were plotted on the ACIC mercator earthside hemisphere lunar map. They were then contoured at intervals of 1×10^{-6} lunar masses (Fig. 51). This method of presentation is a surface mass distribution, and can be converted to units of mass/deg^2 by multiplying the map value by the factor 0.04 cos^2 (lat). This relates the mass per square equatorial degree (approximately 1000 km^2) and the latitude on the map for the contoured levels in units of 1×10^{-6} lunar masses.

Preliminary examination of independent comparison with the quasi-static model (next article, *Subsection* 9) and other data such as equatorial orbits, plus the statistical output of the computer program after the fit, led us to believe that the standard deviation of error is 0.5×10^{-6} lunar masses for a typical individual point. This may be somewhat larger at the limbs, and the effective averaging implied in the contouring may have somewhat reduced the apparent errors. The error limits will be further reduced when the equatorial data set is added to the solution.

d. Interpretation. The most significant observation would seem to be confirmation of the negative ring surrounding Mare Orientale as speculated in Ref. 3 from interpretation of the line-of-sight acceleration. In fact, it can be noted that all the ringed seas seem to have negative areas, particularly Imbrium, Nectaris, and Serenitatis, with Nectaris and Crisium having less pronounced relative lows.

The central-eastern highlands are generally slightly positive, with an interesting field of discrete highs around Mare Nectaris. These include the new mascon area (with our proposed name Lacus Gravitatis) northwest of Nectaris. In addition, there is a diffuse but definite high southeast of Nectaris, one in Mare Fecunditatis and two more highs over Petavius and Furnerius. No speculation is offered regarding whether these last two areas are physically related to the large named craters.

Sinus Aestuum, Grimaldi, and the newly discovered mascon area near the crater Balmer do not show up well on this map. The latter two may just not be quite resolved, and the former is probably coming out with an amplitude that is too low. Equatorial data should refine these regions, since the mass-point spacing will be closer (2.5°) and lower perilune data will have more information content.

It has generally been agreed (Refs. 4 and 5) by selenologists that the Oceanus Procellarum and Mare Tranquillitatis areas are among the most recent lunar surfaces, are most likely to be lava flows, and have a thin regolith. It is interesting to note that these are gravimetric lows, an observation which casts some doubt on

[17] A detailed description of the method employed and the results are presented in Ref. 2.

[18] Although additional useful results can still be obtained by allowing closer mass spacing and still higher correlations (see following article, *Subsection* 9).

the suggestion that the mascons are themselves lava flows which built up the extra mass that we now observe.

References

1. Muller, P. M., and Sjogren, W. L., "Mascons: Lunar Mass Concentrations," *Science*, Vol. 161, No. 3842, pp. 680–684, Aug. 16, 1968.
2. *Dynamic Determination of Mascons on the Moon*, Report No. ATR-69(7140)-1. Aerospace Corp., El Segundo, Calif., Apr. 29, 1969.
3. Muller, P. M., and Sjogren, W. L., "Lunar Gravimetrics," *Proceedings of COSPAR*, 1969.
4. Oberbeck, V. R., and Quaide, W. L., "Genetic Implications of Lunar Regolith Thickness Variations," Icarus, Vol. 9, pp. 446–465, 1968.
5. Tyler, G. L., "Oblique-Scattering Radar Reflectivity of the Lunar Surface: Preliminary Results from Explorer 35," *J. Geophys. Res.*, Vol. 73, No. 24, Dec. 1968.

9. Lunar Gravimetric Maps, *P. Gottlieb*

Most of the information on local lunar gravity features has been obtained from doppler tracking of *Lunar Orbiter* spacecraft at altitudes near 100 km. A representation of the local gravity features (such as mascons) in terms of accelerations at 100 km altitude would, therefore, be quite representative of the data most critical to the construction of the model. The present article provides representations of two models in terms of the resulting radial (directed toward the center of the moon) acceleration expressed in earth milligals (10^{-6} of the gravitational acceleration at the surface of the earth). (Line-of-sight accelerations would be more representative of the actual data, but would greatly distort the field at points more than 20° distant from the sub-earth point.)

The model represented in Fig. 52 was obtained by dynamically estimating the values of 580 point masses on a regular grid across most of the earthside lunar hemisphere. This is called a dynamic model because the values of the masses are estimated in the orbit determination run to estimate the spacecraft state. A description of the actual procedure used to obtain this dynamic model is given in the preceding article (*Subsection 8*).

The model represented in Fig. 53 was obtained by an open loop iteration procedure using 35 orbits (25 nearly polar and 10 nearly equatorial) spaced to cover the earthside lunar hemisphere. At each iteration the model was updated by adding masses whose values were estimated from residual accelerations remaining after orbit determination estimation of the spacecraft state, using the gravitational model updated at the previous iteration. The locations and depths of each new set of masses were chosen according to a reasonable physical interpretation of the residual accelerations. Many masses obtained in this manner had strongly overlapping spheres of influence, and, consequently, had little *individual* physical significance. It was, therefore, physically reasonable to smooth the mass distribution by expanding the field of the point masses in a set of twentieth-degree spherical harmonics. (Further details on the construction of this model are given in SPS 37-57, Vol. II, pp. 68–70.)

The contours of Figs. 52 and 53 were drawn by a program utilizing a two-dimensional interpolation subroutine (described in SPS 37-32, Vol. IV, pp. 18–22). The interpolations were based on numerical evaluations of the acceleration at 2.5° intervals.

A summary of the distinctions in the two model constructing procedures is provided by Table 29. The agreement between Figs. 52 and 53 is somewhat remarkable in view of these distinctions, and should be taken as a confirmation of the results. One difference between the two maps is that the positive acceleration above Sinus Aestuum (lat 10°, lon −10°) is very weak in Fig. 52 (as is mentioned in the preceding article, *Subsection 8*). From the residuals remaining after application of these models, probable errors are estimated to be less than 20 milligals.

Table 29. Comparison of model constructing procedures

Parameter	Dynamic model (Fig. 52)	Quasi-static model (Fig. 53)
Number of orbits	100 polar	25 polar 10 equatorial
Depth of masses	Surface	50–150 km
Spacing of masses	Regular grid	As needed
Smoothing of discrete masses	None	Twentieth-degree spherical harmonics
Arc length	55 min	90 min

The features of these maps are also comparable to the least squares filtered line-of-sight accelerations originally found by Muller and Sjogren (Ref. 1). One new feature of interest is the relative positive acceleration over Mare Fecunditatis (lat −4°, lon 48°).

Reference

1. Muller, P. M., and Sjogren, W. L., "Mascons: Lunar Mass Concentrations," *Science*, Vol. 161, No. 3842, pp. 680–684, Aug. 16, 1968.

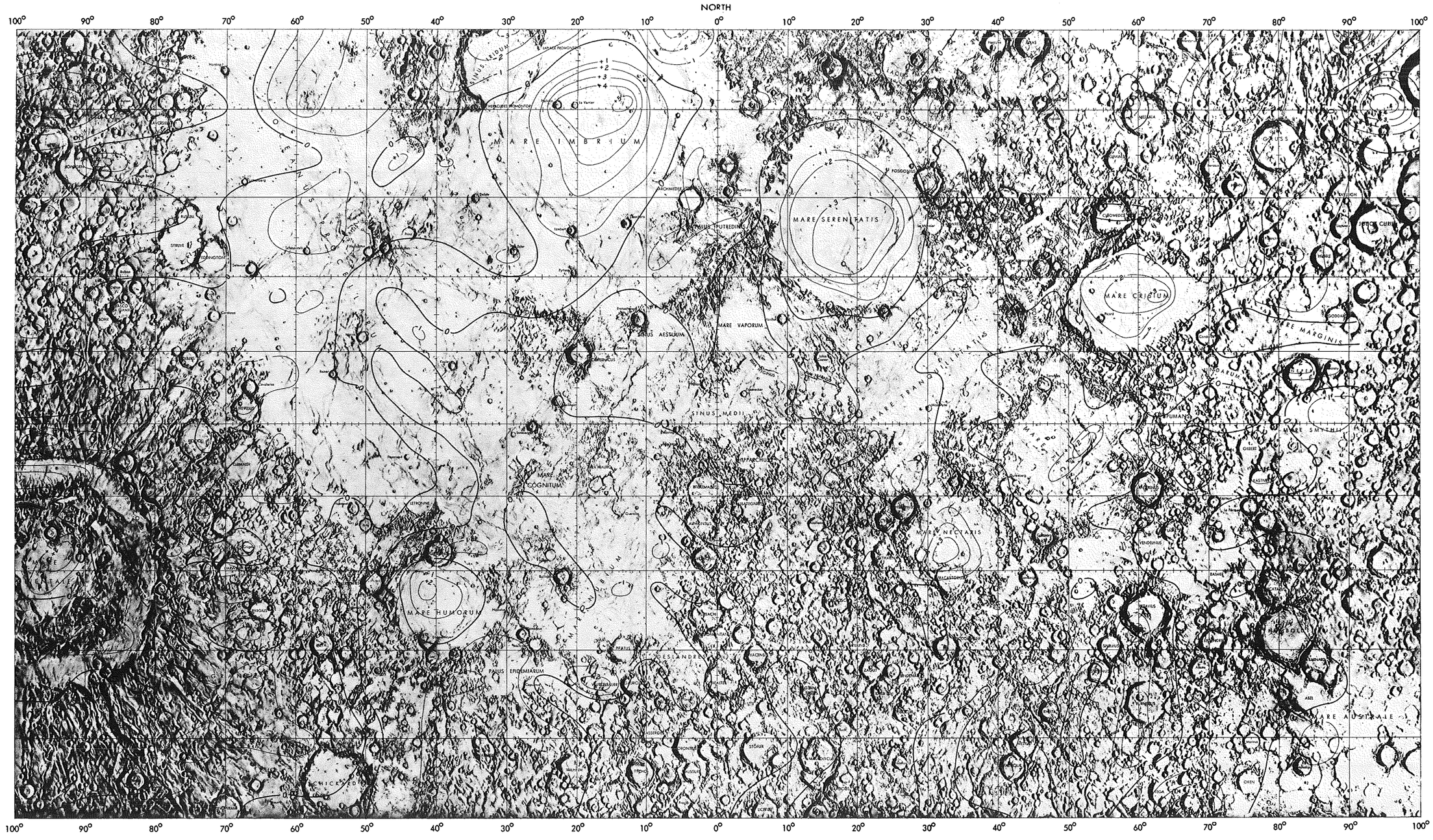

Fig. 51. A surface mass distribution

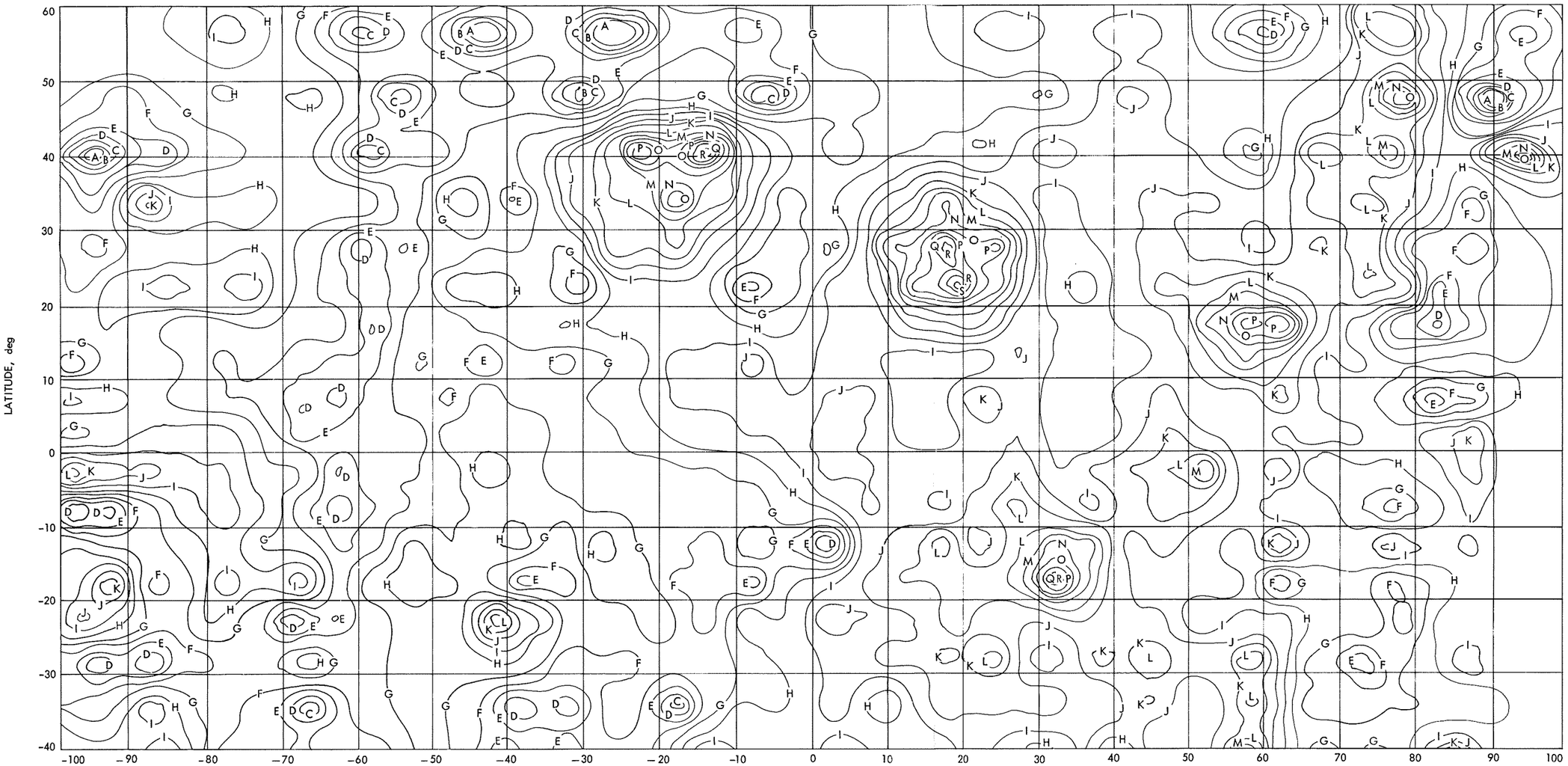

CONTOUR	VALUE, milligals
A	-175
B	-150
C	-125
D	-100
E	-75
F	-50
G	-25
H	0
I	25
J	50
K	75
L	100
M	125
N	150
O	175
P	200
Q	225
R	250
S	275
T	300
U	325
V	350
W	375

Fig. 52. Radial acceleration of discrete points mass from dynamic model

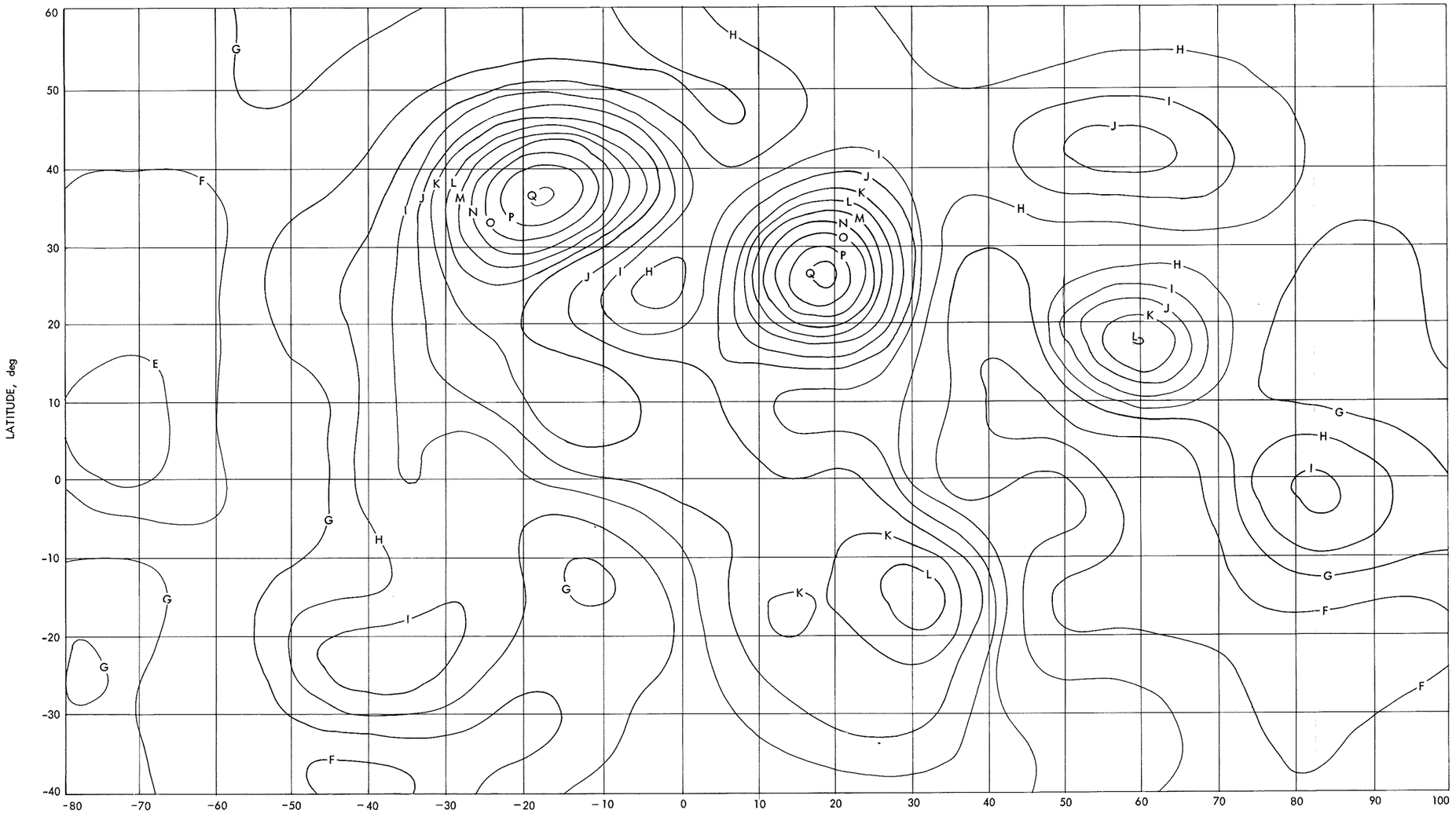

CONTOUR	VALUE, milligals
A	-175
B	-150
C	-125
D	-100
E	-75
F	-50
G	-25
H	0
I	25
J	50
K	75
L	100
M	125
N	150
O	175
P	200
Q	225
R	250
S	275
T	300
U	325
V	350
W	375

Fig. 53. Radial acceleration from quasi-static, smoothed model

Page intentionally left blank

10. The Paucity of Gravimetric Information Due to Spurious Anomalies in *Apollo 10* and *11* LM Tracking Data, *P. Gottlieb and W. L. Sjogren*

Recent progress in the estimation of local lunar gravity features based on doppler tracking data from *Lunar Orbiter* spacecraft (see the two preceding articles, *Subsections 8 and 9*) has encouraged the belief that still more gravitational information should be obtainable from lower altitude spacecraft. An attempt was made on the *Apollo 10* and *11* missions where the lunar module (LM) was tracked in a ballistic orbit to within 11 km of the lunar surface. This compares with a 50- to 100-km periapsis altitude for the *Lunar Orbiter* spacecraft. Unfortunately, the receiver seems to have been poorly locked-up during much of the tracking time (i.e., there were 10 bad gaps in the 30 min of *Apollo 10* LM data). Perhaps there were antenna pointing problems, for there were some large doppler anomalies on *Apollo 10* for which there seems to be no physical explanation and which were not observed on *Apollo 11* when overflying the same area. Even the smaller doppler anomalies of *Apollo 10*, which could have been due to the surface mass distributions, were not confirmed in the *Apollo 11* tracking data. These smaller scale doppler anomalies were probably caused by spurious oscillation of the spacecraft leading to small, but rapid, motions of the antenna. The spacecraft attitude control logs were insufficient to either confirm or contradict this hypothesis.

The DSS 14 antenna (Goldstone, 210 ft) was used to receive the 3-way S-band signal and the doppler was computed at 1-s intervals using the fractional cycle resolver to overcome the quantization error caused by the small counting time. The minimum spacecraft altitude of 11 km allowed resolution (minimum observable horizontal dimension of a well-distinguished feature) to approximately 10 km. This resolution is at least a factor of 10 better than the *Lunar Orbiter* data. The sample rate of 1-per-second provided 6 samples over 10 km of path length, giving some redundancy and smoothing capability.

The *Apollo 10* and *11* orbits were almost equatorial and essentially had the same lunar track, so that they provide a direct check on each other's acceleration patterns. The 20–25 min arc of 1-s tracking data was fit using a simple triaxial model for the lunar gravitational field.

There were three large anomalies (Fig. 54) in the resulting doppler residuals from *Apollo 10*. The first two were positive peaks at longitudes of 85°E and 78°E,

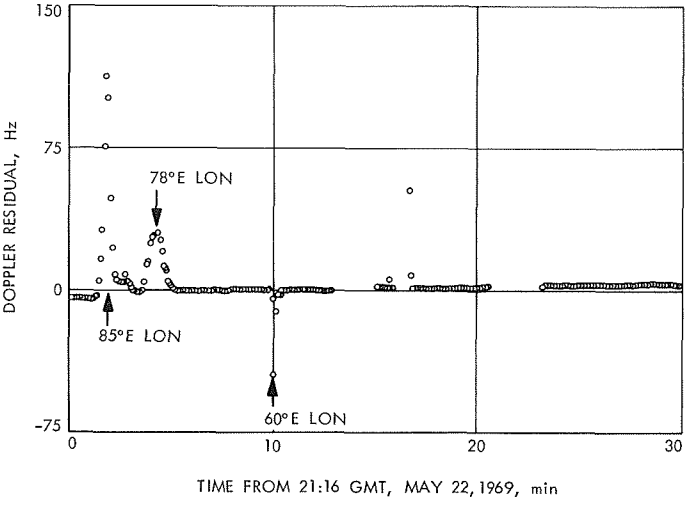

Fig. 54. *Apollo 10* LM descent residuals

respectively. The third was a negative peak at longitude 60°E. Examples of positive masses which could produce such positive peaks are hemispherical lumps of material of density 12 g/cm^3, 68 and 50 km deep, respectively. The negative peak is so sharp that it would have to be produced by a 10-km-diameter mass of 10 g/cm^3. These large residuals occurred shortly after initial acquisition of signal from exit occultation and during times of loss of voice communication. It is believed that antenna pointing problems caused the difficulty in signal lock-up.

The *Apollo 10* LM tracking data also shows three less spectacular features. One of the features is the sharp negative slope at 23.5 min (68°E lon) shown in Fig. 55. The extreme sharpness of this acceleration indicates a hole 25 km in diameter which would have to be more than 20 km deep to provide the required negative mass. However, when this same longitude is examined in *Apollo 11* data (Fig. 56), there is no indication of any negative slope in the residuals. Also visible here is the

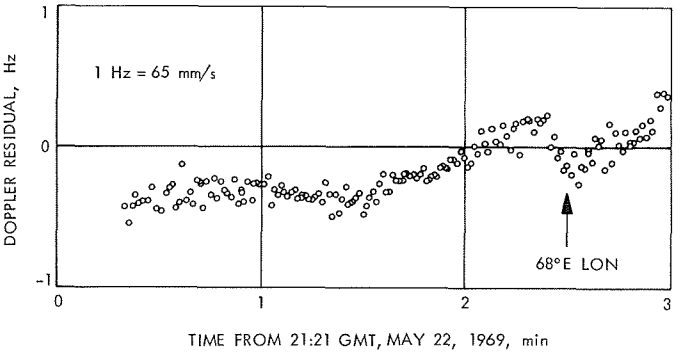

Fig. 55. Detail of *Apollo 10* LM descent residuals

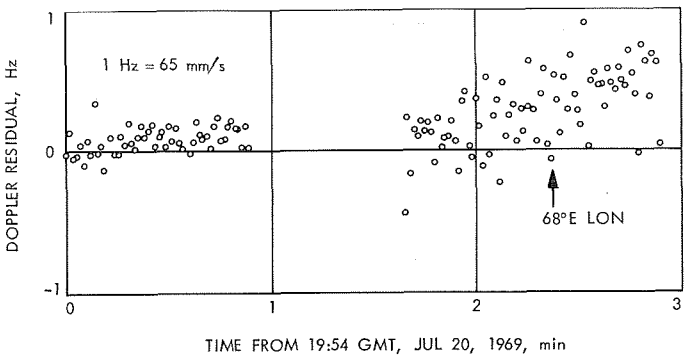

Fig. 56. Detail of *Apollo 11* LM descent residuals

fact that *Apollo 11* data was somewhat noisier than *Apollo 10*. This was the same situation with the other possible gravity anomalies, that each data block contradicted the other and no two anomalies are correlated.

If significant information from the low-altitude LM tracking data is to be obtained, both the receiver lock-up (spacecraft antenna pointing?) problem and spacecraft spurious motions from maneuvers and venting must be eliminated.

11. Use of Lunar Transponders to Obtain DSS Locations: Lunar Physical Libration Analysis,

F. B. Winn and G. Dvornychenko

Planetary and lunar spacecraft tracking data have been used to determine the absolute longitudes of Deep Space Stations (DSSs), as discussed by Mottinger in *Subsection 3* of this chapter. At present only two data spans are available which result in absolute longitude solutions of the desired accuracy, namely, the encounter phases of the *Mariner IV* (Mars, 1964) and *Mariner V* (Venus, 1967) missions. Additional solutions are needed and the tracking data from the *Surveyor* spacecraft, while they were resting on the lunar surface, represent an excellent source of accurate DSS location solutions, providing certain problems can be surmounted.

One of the corrupting influences associated with the lunar landed *Surveyor* tracking data, which prevents the determination of absolute DSS longitude, is the physical libration of the lunar figure.

In the first article of this series (SPS 37-56, Vol. II, pp. 74–80), Winn, employing the single-precision orbit determination program (SPODP) (Ref. 1), showed that the SPODP lunar physical libration model (Refs. 2 and 3) does not model the lunar landed *Surveyor I*, two-way doppler tracking data. Furthermore, the replacement of Heyn's coefficients with Eckhardt's (Ref. 4) did not improve the performance of the libration algorithm.

This article, the second of this series on lunar physical librations, will show that:

(1) The omission of some of the libration terms from the SPODP libration model does induce detectable range-rate errors in the *Surveyor I* topocentric doppler calculations.

(2) All libration terms of this study should be incorporated into the double-precision orbit determination program (DPODP)[19] libration model (Ref. 4).

(3) The preponderance of the SPODP libration modeling error does not stem from libration series truncation errors.

The SPODP and DPODP physical libration models utilize only the three terms of largest amplitude for each physical libration series:

$$\sigma = [-109''.\sin(g) + 37''.\sin(g+2\omega) - 11''.\sin(2g+2\omega)]/I \quad (1)$$

$$\rho = -107''.\cos(g) + 37''.\cos(g+2\omega) - 11''.\cos(2g+2\omega) \quad (2)$$

$$\tau = -12''.\sin(g) + 59''.\sin(g') + 18''.\sin(2\omega) \quad (3)$$

where

σ = total physical libration in the longitude of the mean ascending node of the lunar orbit on the ecliptic

ρ = total physical libration of the mean inclination of the lunar equator relative to the ecliptic

τ = total physical libration in the mean lunar longitude measured along the ecliptic

$g = \mathbb{C} - \Gamma'$ = mean anomaly of the moon

$g' = \odot - \Gamma$ = mean anomaly of the sun

$\omega = \Gamma - \Omega$ = argument of perigee of the moon

I = inclination of lunar equator relative to the ecliptic

[19]Warner, M., *Double Precision Orbit Determination Program*, June 15, 1967 (JPL internal document).

The truncation error associated with the σ, ρ, and τ series due to the omission of eight smaller amplitude terms are formulated in Eqs. (4), (5), and (6) (Ref. 5):

$$\Delta\sigma = [-3''.2\sin(2g' + 2\omega') - 2''.5 \sin(g - 2g' + 2\omega - 2\omega')]/I \quad (4)$$

$$\Delta\rho = -3''.2\cos(2g' + 2\omega') - 1''.9 \cos(g - 2g' + 2\omega - 2\omega') \quad (5)$$

$$\Delta\tau = -10''.\sin(-2g' + 2\omega - 2\omega') - 4''.2\sin(g - 2g' + 2\omega - 2\omega') + 3''.5\sin(\omega - g' - \omega') + 1''.7\sin(2g' + 2\omega') \quad (6)$$

where

$\omega' = \odot\text{-}g' =$ argument of perigee of the sun

To ascertain unambiguously the contributions of each physical libration term (Eqs. 1 through 6), the spatial displacements and speeds and topocentric radial velocities of *Surveyor I*[20] due to each individual libration were determined.

The spatial displacement of *Surveyor I* due to the libration algorithm defined by Eqs. (1) through (6) was computed in the following manner:

$$\left| \sum_{i=1,17} \Delta\underline{r}_i \right| = \left| \sum_{i=1,17} \Delta L_i \left[\frac{\partial [M]^T}{\partial L_i} \right] \underline{R} \right| \quad (7)$$

where

$|\Delta\underline{r}_i|$ = spatial displacement of *Surveyor I* in selenocentric, earth-equatorial, coordinates due to the ith libration term

$\underline{R}$ = selenocentric, moon-fixed, coordinates of *Surveyor I*

ΔL_i = numerical value of the ith libration coefficient as reported by Eckhardt (Ref. 4)

$\frac{\partial [M]^T}{\partial L_i}$ = partial derivative of the selenocentric, moon-fixed, to selenocentric, earth-equatorial, coordinate transformation matrix with respect to the ith libration coefficient

$[M]^T$ = moon-centered, moon-fixed, to moon-centered, earth-equatorial, transformation matrix defined as

$$[M]^T = [R_{+X}(\bar{\epsilon})]^T [R_{+Z'}(\bar{\Omega} + \sigma)]^T [R_{-X}(\bar{I} + \rho)]^T [R_{+Z}(\bar{\mathbb{C}} + \tau - \bar{\Omega} - \sigma + \pi)]^T \quad (8)$$

$[R_{+X}(\bar{\epsilon})]^T$ = rotation about the earth-equatorial X axis through angle equal to the mean obliquity of the ecliptic

$[R_{+Z'}(\bar{\Omega}+\sigma)]^T$ = rotation around the resulting Z' axis through an angle equal to the longitude of the true ascending node of the lunar orbit referenced to the mean ecliptic

$[R_{-X}(\bar{I}+\rho)]^T$ = rotation around the X' axis through an angle equal to the true inclination of the lunar equator with respect to the ecliptic (negative rotation)

$[R_{+Z}(\bar{\mathbb{C}}+\tau-\bar{\Omega}-\sigma+\pi)]^T$ = rotation around the resulting Z'' axis through an angle equal to the true longitude of the moon minus the longitude of the true ascending node plus π radians

Similarly, the spatial displacement of *Surveyor I*, from a nonlibrated inertial position, due to the libration algorithm defined by Eqs. (1) through (3), was computed.

Figure 57 depicts the *Surveyor I* spatial displacement, from a nonlibrated inertial position, associated with both libration functions. The plots show that the two libration functions do significantly differ in their influences on the *Surveyor I* inertial position (at times, the separation is greater than 35 m).

Using a technique similar to Eq. (7), it is also simple to compute the spatial speed resulting from the two sets of libration series components:

$$\left| \sum_{i=1,17} \Delta\dot{\underline{r}}_i \right| = \left| \sum_{i=1,17} \Delta L_i \left[\frac{\partial [\dot{M}]^T}{\partial L_i} \right] \underline{R} \right| \quad (9)$$

[20] *Surveyor I*, because of its displacement in longitude from the center of the earth-viewable lunar disk, is more sensitive to the libration than any other *Surveyor* (that is, the line-of-sight projection of the total libration is the largest), and hence was used for this study.

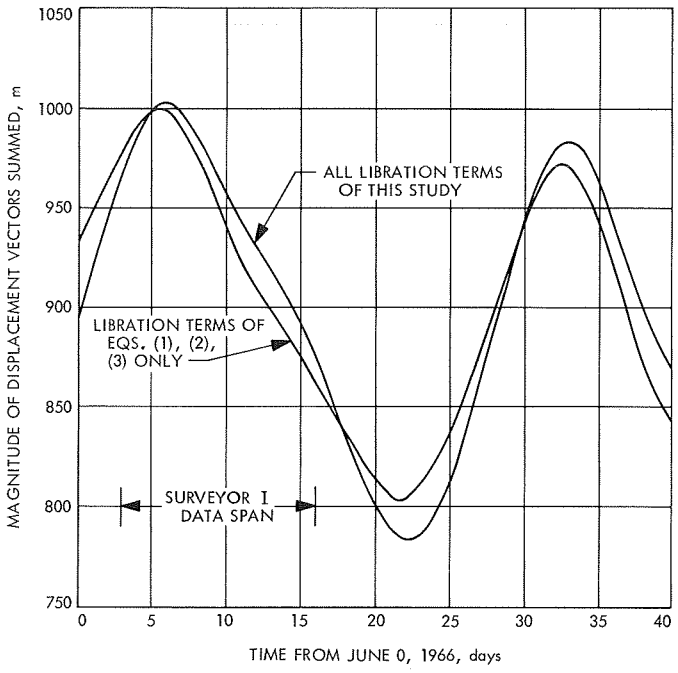

Fig. 57. *Surveyor I* spatial displacement: total libration functions

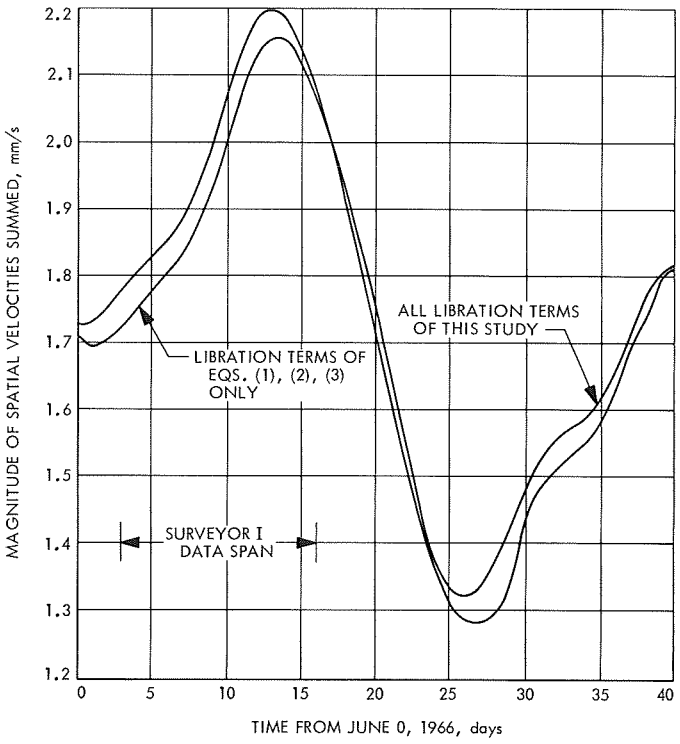

Fig. 58. *Surveyor I* spatial velocity: total libration functions

where

$|\Delta\dot{\underline{r}}_i|$ = spatial speed of *Surveyor I* in selenocentric, earth-equatorial, coordinates due to the ith libration term

$\frac{\partial[\dot{M}]^T}{\partial L_i}$ = partial of the time rate of change of the selenocentric, moon-fixed, to selenocentric, space-fixed, coordinate transformation matrix with respect to the ith libration term

The magnitudes of $\Delta\dot{\underline{r}}_i$ are plotted in Fig. 58. The plotted spatial speeds of *Surveyor I* due to the libration functions reveal the upper limits of the libration series truncation influences upon the topocentric range-rate observations, for the induced spatial speeds are the induced range-rate upper limits.

Figure 58 shows a maximum spatial speed error of 0.56 mm/s (that is, a 5.6-m differenced range error per 10^4 s). This significantly exceeds the accuracy constraint placed upon the DPODP which is the ability to compute doppler integrated over 10^4 to an accuracy of better than 0.1 m.

A more detailed investigation of the libration series component terms is permitted in Figs. 59, 60, and 61. These figures depict the spatial speed of the *Surveyor I* lunar site during a 40-day period due to each libration term independently.

The maximum differenced range error will be realized when the total spatial velocity is aligned with the observer-probe direction. Thus, by taking the maximum spatial velocities associated with each libration term as plotted in Figs. 59, 60, and 61, and assuming the velocities to be non-variant over 10^4 s, it is a simple operation to ascertain the maximum differenced range error that can result for a *Surveyor I* doppler observation due to individual libration term omissions. Table 30 tabulates the maximized differenced range error associated with each libration component of this study. The sum of the maximum differenced range errors which could result from truncated libration terms is 5.6 m/10^4 s.

Finally, the lunar physical libration model's modification of the *Surveyor I* topocentric radial velocity is examined. The projection of the spatial speed induced by the physical libration algorithm along an observer's line of sight is accomplished:

$$\sum_{i=1,17} \Delta\dot{\rho}_i = \sum_{i=1,17} \left[\Delta L_i \frac{\partial[\dot{M}]^T}{\partial L_i} \underline{R}\right] \cdot \underline{\rho} \qquad (10)$$

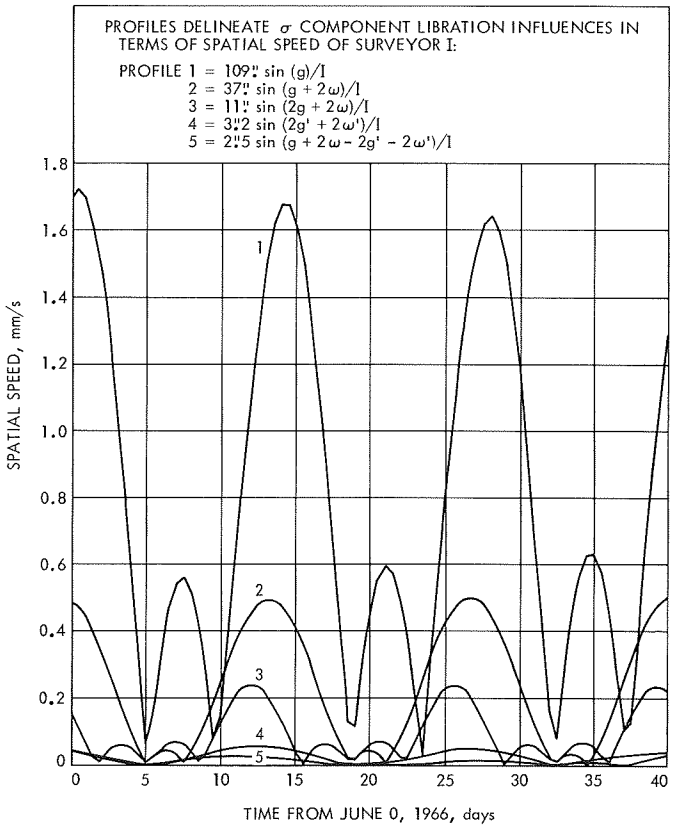

Fig. 59. Spatial speed: σ libration series

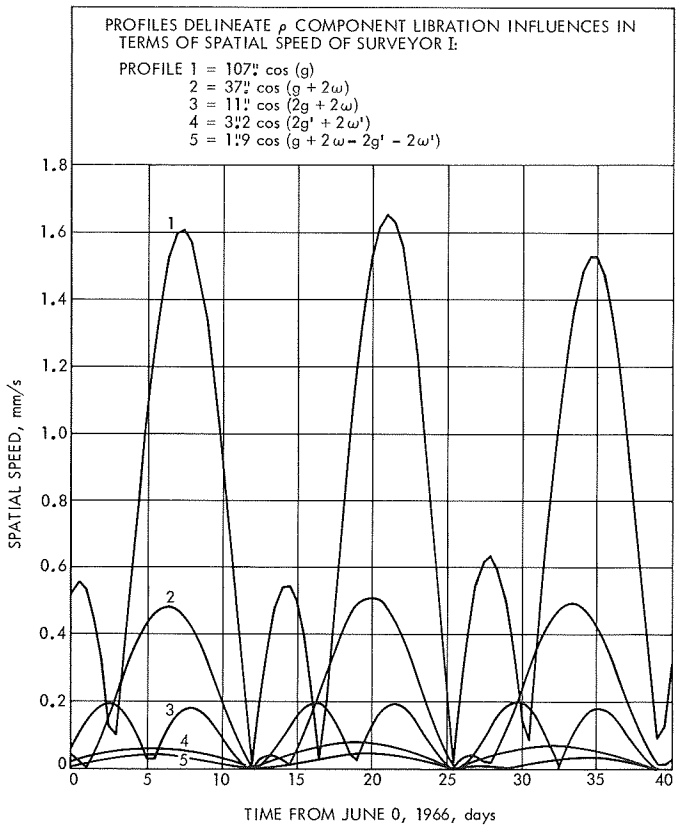

Fig. 60. Spatial speed: ρ libration series

where

$\Delta\dot{\rho}_i$ = topocentric radial velocity of *Surveyor I* due to the ith component of the libration model

$\underline{\rho}$ = topocentric range vector of *Surveyor I* as viewed at Canberra

The accumulative error which can result due to libration series truncation is shown in Fig. 62. The figure also presents a comparison between the truncated and the complete libration model of this study as they influence the *Surveyor I*–Canberra range rate.

The maximum difference between the two range-rate profiles is only 0.11 mm/s (1.1 m/10^4 s) or approximately 20% of the truncated libration models minimum value during the *Surveyor I* period.

As previously reported (SPS 37-56, Vol. II), the *Surveyor I* data was fit "best" when no libration modeling was attempted. Thus, it is apparent that the 20% range-rate error due to series truncation is not the primary cause of the algorithm's failure.

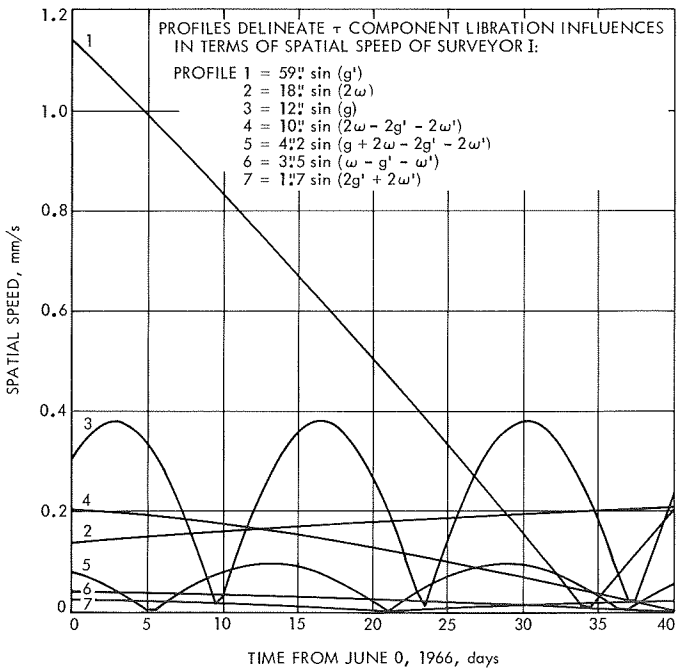

Fig. 61. Spatial speed: τ libration series

Table 30. Libration terms

Libration term argument	Period, days	Libration term amplitude, arc sec			$\lvert \sum \Delta\dot{r} \rvert \times 10^4$ s, meters			SPODP and DPODP retained
		σ^a	ρ^a	τ^a	σ	ρ	τ	
$2g + 2\omega$	14	11.0	11.0	—	2.3	2.0	—	✓
$g + 2\omega$	28	37.0	37.0	—	4.9	4.8	—	✓
g	28	109.0	107.0	12.0	17.0	16.0	3.7	✓
$g + 2\omega - 2g' - 2\omega'$	32	2.5	1.9	4.2	0.2	0.4	1.0	
$2g' + 2\omega'$	174	3.2	3.2	1.7	0.5	0.6	0.3	
$2\omega - 2g' - 2\omega'$	206	—	—	10.0	—	—	2.1	
g'	365	—	—	59.0	—	—	20.5	✓
$\omega - g' - \omega'$	418	—	—	3.5	—	—	0.5	
2ω	1100	—	—	18.0	—	—	3.9	✓

[a]Lunar central angle.

At this time, there is no confirmed explanation for the libration model's apparent failure. As a matter of course, the theory and computer algorithm are being investigated in detail; however, there are other possible error sources which remain to be studied. Such error sources are: tropospheric refraction, ionospheric charged-particle effects, lunar ephemeris, data selection effects, etc.

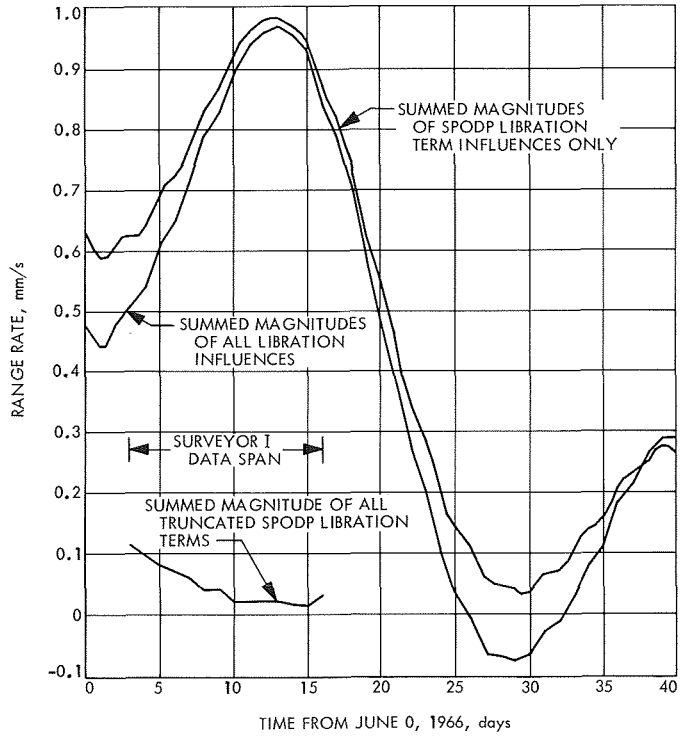

Fig. 62. *Surveyor I* range rate: total libration functions

All libration terms of this study (17) should be included into the DPODP to meet the DPODP accuracy constraint of 0.1 m/10^4 s. Not only are these libration terms of sufficient size to warrant DPODP inclusion, but their summed influences introduced a 0.1-mm/s error in the *Surveyor I* range-rate calculations (20% of the total libration algorithm influence). The preponderance of the SPODP libration model failure is not due to libration series truncation errors.

References

1. Warner, M. R., and Nead, M. W., *SPODP—Single Precision Orbit Determination Program,* Technical Memorandum 33-204. Jet Propulsion Laboratory, Pasadena, Calif., Feb. 15, 1965.
2. White, R. J., et al., *SPACE—Single Precision Cowell Trajectory Program,* Technical Memorandum 33-198. Jet Propulsion Laboratory, Pasadena, Calif., Jan. 15, 1965.
3. Hoffman, H. M., and Davies, J. R., *Landed Surveyor Modification for the Orbit Determination Program,* Design Document. Computer Applications, Inc., Glendale, Calif., Oct. 13, 1966.
4. *Measure of the Moon.* Edited by Z. Kopal and C. L. Goudas. D. Reidel Publishing Co., Dordrecht, Holland, 1967.
5. Melbourne, W. G., et al., *Constants and Related Information for Astrodynamic Calculations, 1968,* Technical Report 32-1306. Jet Propulsion Laboratory, Pasadena, Calif., July 15, 1968.

12. The Doppler Determination Accuracy of the Earth Gravitational Constant From Artificial Satellites as a Function of Orbital Elements,

G. E. Pease

a. Introduction. To date, it has been recognized that one of the most accurate values for $GM_\oplus$, the earth gravi-

tational constant, has been obtained by combining the result of the *Ranger* lunar missions (Ref. 1). This has been widely used to represent the zero-order term of the earth's potential in geodetic satellite solutions for the harmonic coefficients of the potential expansion. Gravitational constant solutions competitive with the combined *Ranger* value may now exist based on the early phase of the *Mariner* planetary missions (Ref. 2) and the radio tracking of artificial satellites (SPS 37-53, Vol. II, pp. 16–20, and SPS 37-56, Vol. II, pp. 80–85). In the case of a satellite solution, it is of interest to discover which orbital characteristics are most favorable to a rapid solution for $GM_\oplus$.

This article examines the doppler solution for $GM_\oplus$ as the conic elements of the satellite orbit are varied. Two classes of effects are involved here: (1) gravitational effects, primarily involving the distance of the satellite from earth (these are predominant in varying a and e); and (2) tracking geometry effects, primarily involving the length of time the satellite is tracked by each tracking station (predominant orbital elements here are i and Ω). In this study we examine the effects of varying the orbital elements a, e, i, and Ω. Early tracking results from varying a and e in many respects reproduce the effects of varying ω, the argument of perigee, which was, therefore, not studied separately. The geometrical effect of varying the mean anomaly t_0 is slight with good tracking station coverage, and was also not considered of sufficient interest for inclusion. Here again, the gravitational effects of varying t_0 are identical to those in varying a and e for short initial tracking spans.

As with other data reduction tasks, there are inherent limitations on the ability to extract information, including $GM_\oplus$, from the analysis of radio tracking data. These limitations include the degree to which both the noise on the observations and the physical system are properly represented in the regression model.

The noise on each data point was assumed independent of that on any other tracking data point, while in reality correlations do exist (this assumption greatly simplifies the analysis). However, the data weights are increased as a function of known correlated error on the tracking data to compensate for this assumption.

The fitter's model of the universe (physical system) may differ from the real universe either because of a simplified dynamical model (a conic spacecraft orbit is assumed, i.e., all gravitational forces are ignored except that due to $GM_\oplus$) or because random disturbances to the spacecraft motion are not properly taken into account. This latter category is known as process noise and includes such items as attitude-control forces (i.e., valves seating differently after each use thus causing a variable leak rate) and fluctuations in drag or solar radiation forces. Some model errors can be treated as correlated noise on the tracking data and thus contribute to the data weight used for this study.

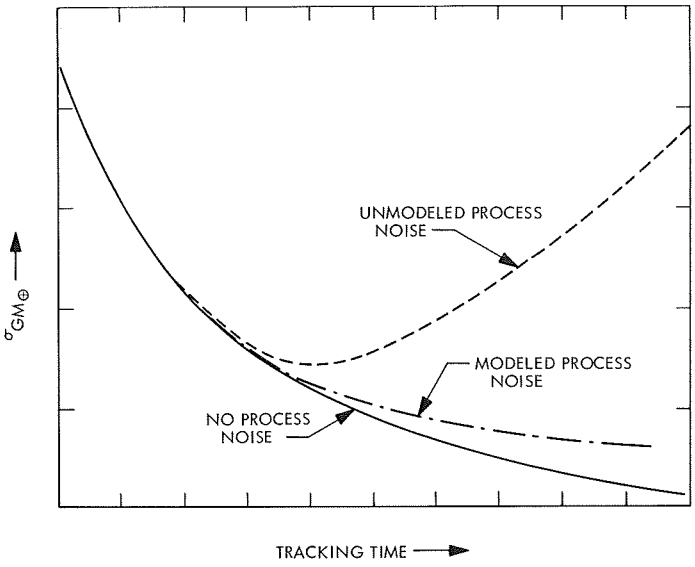

Fig. 63. Illustration of role of process noise in obtaining $GM_\oplus$ solutions

For the case of process noise, previous investigators have shown[21] effects analogous to those illustrated in Fig. 63, when cases containing unmodeled, modeled, and no process noise are compared. Notice that if process noise exists and is ignored (either not practical to model or not known well enough), the $GM_\oplus$ solution can actually be degraded by the addition of more tracking data. Also, if the process noise is properly modeled, the accuracy of the $GM_\oplus$ solution approaches a lower bound asymptotically as more data is added, thereby putting a practical limit on the length of data arc which need be processed.

Uncorrelated data noise, a conic spacecraft orbit, and the absence of process noise were assumed for this study. Although such a technique can reveal the relative quality of $GM_\oplus$ solutions obtainable as a function of the elements of an earth-orbiting spacecraft, care must be used in determining the region of validity. That is, while the

[21]Nishimura, T., *Evaluation of the Error Caused by Application of Non-optimal Estimators to the Orbit Determination of Low-Thrusted Spacecraft*, Apr. 21, 1966 (JPL internal document).

weight assigned the tracking data was adjusted to compensate for the first two assumptions, the fact that process noise is ignored causes the comparisons of the ability to determine $GM_\oplus$ among various orbital geometries presented in this article to lose their validity as the tracking data span increases. The analysis of process noise and its effects on the ability to determine $GM_\oplus$ from radio tracking of earth orbiters will constitute the next phase of this study.

b. Tracking model. As in Refs. 1 and 2, simulated range-rate tracking data were utilized, with a 1-σ weight of 2.23 mm/s per 300-s data sample except for the runs with small a ($a = 800$ km), where an equivalent 1-σ weight of 5 mm/s was used per 60-s sample. These data weights are roughly an order of magnitude higher than correlated data noise of observed S-band high-frequency data in order that unmodeled error sources such as the non-spherical earth gravitational potential can be represented. Three tracking stations were simulated 120° from each other in longitude and latitudes of 0°, +45°, and −45° (in order of increasing east longitude). The mean anomaly and argument of perigee were selected to place the satellite at perigee and on the meridian of the 0° latitude tracking station at the start of simulated tracking. Simulated tracking data were not taken below 10-deg satellite elevation angle.

c. Statistical model. The statistical computations were performed by the JPL Multiple-Link Satellite Program (MLSP) described in the following article, *Subsection 13.* This computer program utilizes elliptical orbital elements to define the satellite state vector, which makes it extremely fast and efficient for statistical computations. A simple two-body representation such as this does, however, ignore effects such as lunisolar and planetary perturbations, solar radiation pressure, atmospheric drag, and non-spherical gravitational potential of the central body. Although MLSP may be used for analyzing simultaneous tracking of more than one satellite, only one satellite at a time was simulated in this study. The program was used to compute a covariance matrix

$$\Gamma = \left(\sum_{i=1}^{N} \phi_i \, w_i^{-1} \, \phi_i^T + \tilde{\Gamma}^{-1} \right)^{-1}$$

where, for the ith observation, ϕ_i is the vector of partial derivatives of range rate with respect to the parameters for which we desire statistics, w_i the variance of the data point, and $\tilde{\Gamma}$ a diagonal *a priori* covariance matrix.

The topocentric range vector of the satellite at each data point is computed as

$$\boldsymbol{\rho} = \mathbf{R}_G - \mathbf{R}_{GS}$$

where $\mathbf{R}_G$ is the geocentric range vector of the satellite and $\mathbf{R}_{GS}$ is the geocentric station vector, and

$$\mathbf{R}_G = f(a, e, i, \Omega, \omega, GM_\oplus, t_0, t) = f(Q_G, t)$$

$$\mathbf{R}_{GS} = f(\lambda, \phi, R_{GS}, t) = f(Q_{GS}, t)$$

In this formulation, t is the independent time argument and λ, ϕ, R_{GS} are the respective station coordinates of longitude, latitude, and geocentric radius. The range rate is computed as

$$\dot{\rho} = \frac{\dot{\boldsymbol{\rho}} \cdot \boldsymbol{\rho}}{\rho}$$

and the partial derivatives are

$$\frac{\partial \dot{\rho}}{\partial Q} = \frac{\frac{\partial \dot{\boldsymbol{\rho}}}{\partial Q} \cdot \boldsymbol{\rho} + \dot{\boldsymbol{\rho}} \cdot \frac{\partial \boldsymbol{\rho}}{\partial Q} - \frac{\partial \rho}{\partial Q} \cdot \frac{\dot{\rho}}{\rho}}{\rho}$$

For this study, the full set of $Q = Q_G, Q_{GS}$ was represented in the covariance matrices from which standard deviations of $GM_\oplus$ were obtained.

d. Parametric analysis. No *a priori* information was input except on tracking station coordinates. These were assumed known to 20 m in λ and ϕ and 10 m in R_{GS}.[22] In each of the runs, a covariance matrix is computed every 3 h from the start of tracking up to 36 h. A standard orbit was adopted and a, e, i, Ω were varied one at a time, holding the others fixed at the standard values. The standard elements and the variations on them are listed in Table 31.

It may be seen that a very wide range of satellite orbits is represented in the table. Figure 64 shows $GM_\oplus$ accuracy as a function of tracking time for the standard orbit. The tracking stations which are in view (satellite above 10-deg elevation angle) are identified on the horizontal bar by their latitude.

[22]Although tracking stations with a capability comparable to a DSS were assumed, it was not assumed that their locations are known to 3 m in λ and 1.5 m in r_s as is the case for the DSS.

Table 31. Standard and varied orbital elements

Element	Standard value	Varied values
a, km	24000	8000, 16000, 32000, 40000
e	0.1	0.3, 0.5, 0.7
i, deg	45	5, 25, 65, 85
Ω (measured from t_0), deg	0	90, 180, 270
ω, deg	0	Not varied
t_0	(see *Tracking model, Paragraph b*)	Not varied

This plot indicates that doppler tracking of a satellite in the standard orbit is not sufficient to determine $GM_\oplus$ to the combined *Ranger* accuracy, at least for only 36 h of tracking data. This conclusion was also reached for somewhat lower orbits in SPS 37-53, Vol. II. In that study the addition of ranging data was found to significantly lower $\sigma_{GM_\oplus}$.

Figure 65 shows the behavior of the standard orbit solution as the semimajor axis of the orbit is varied. Each curve represents a different amount of tracking time. The plateau between $a = 24{,}000$ km and $a = 32{,}000$ km for the 6-h tracking interval plot is caused by the existence of more tracking station view overlap for the higher satellite. This is because the first station tracking the lower satellite is lost from view more quickly due to the greater angular velocity of this satellite. The lower-altitude orbits show an astonishingly rapid and accurate ability to estimate $GM_\oplus$. In reality, these orbits would be somewhat corrupted by atmospheric drag and high-order earth gravitational potential effects. Because of this, the plotted numbers at $a = 8000$ km should not be taken too literally. An effect that was noticed in SPS 37-56, Vol. II, is also present. This is the tendency for the higher-altitude orbits to become comparatively more suitable for determining $GM_\oplus$ with long tracking times. This is seen in the flattening of the curves towards the horizontal at longer tracking times. On the other hand, absolute accuracies at the higher altitudes are in substantial disagreement with the results of SPS 37-56, Vol. II, which utilized a much more sophisticated mathematical model, including a numerical integration of the satellite orbits which represented perturbations of the sun, moon and planets. Nevertheless, the results of this study, using a simple conic model, appear to be a great deal more realistic. This may be due to a number of factors, such as the different tracking station geometry or the 10-deg elevation limit on data in this study (in SPS 37-56, Vol. II, data were taken from horizon to horizon, but low-elevation data were weighted in a way that accounted for uncertainties in the refraction model). The possibility also exists that the complex motion resulting from lunisolar and planetary perturbations on high-altitude satellites enhances the orbit determination process, as reflected in the results

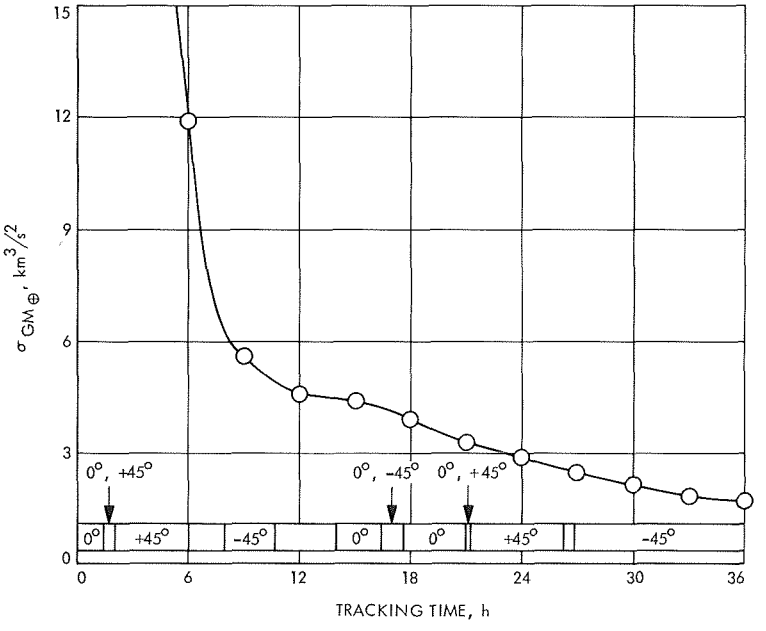

Fig. 64. $GM_\oplus$ standard deviation as a function of tracking time

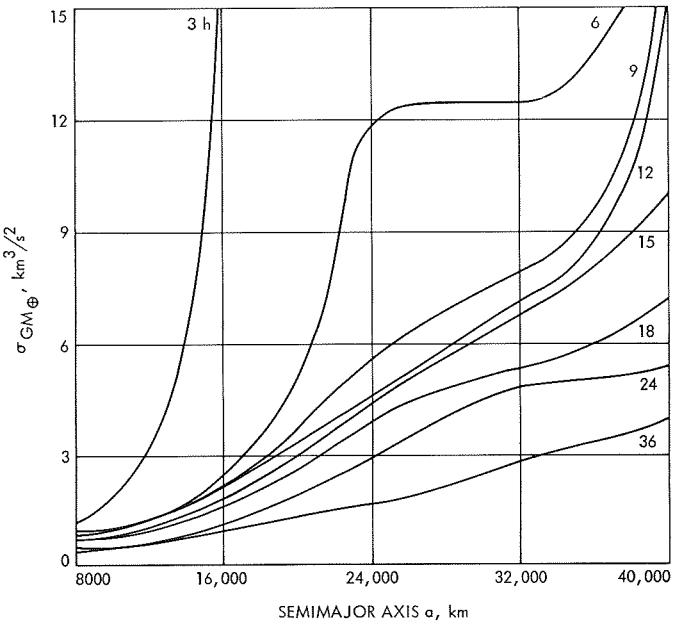

Fig. 65. $GM_\oplus$ standard deviation as a function of orbital semimajor axis for various tracking intervals

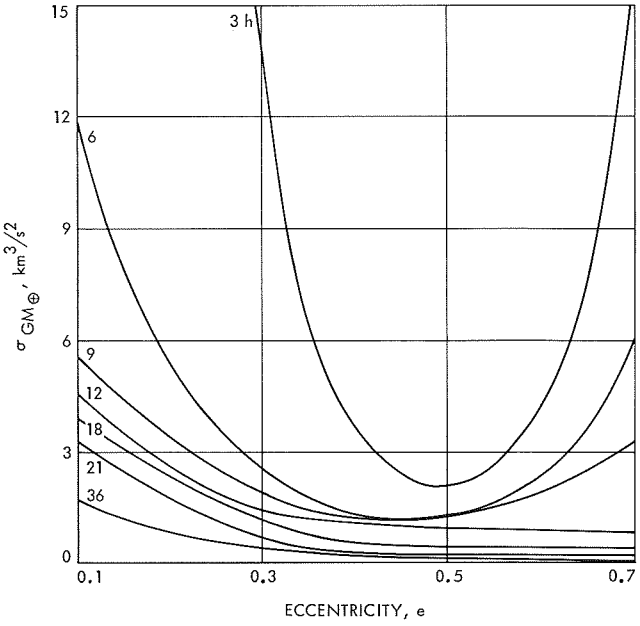

Fig. 66. $GM_\oplus$ standard deviation as a function of orbital eccentricity for various tracking intervals

of SPS 37-56, Vol. II. At any rate, it seems clear that high-altitude orbits require substantially longer tracking times and/or the addition of ranging data to equal the results from low orbits.

Figure 66 illustrates the improvement available to the 24,000-km standard orbit at higher orbital eccentricities. At an eccentricity of 0.5, the $GM_\oplus$ accuracy is dramatic. This is because tracking has been set up to start at perigee, so that the first data points are similar to those in a lower orbit. Apparently the increased radial velocity of the high-eccentricity satellites is an important factor, since these orbits yield an even lower 36-h value for $\sigma_{GM_\oplus}$ than a near-circular low-orbit satellite ($\sigma_{GM_\oplus} = 0.1$ km^3/s^2 compared with 0.4 km^3/s^2 for the 8000-km low-eccentricity orbit). Such a high-eccentricity, high-altitude satellite is therefore more than competitive with *Ranger* or *Mariner* for determining $GM_\oplus$, provided that earth gravitational harmonics can be well-modeled near perigee. Figure 66 indicates that for short tracking times the determination of $GM_\oplus$ becomes worse above an eccentricity of 0.5. This is because at perigee the angular velocity of these satellites is so high as to cause large gaps between acquisition by the various tracking stations. The longer tracking interval or the addition of extra tracking stations will remedy this situation.

Figure 67 illustrates the effect of altering tracking geometry by varying the orbital inclination of the standard satellite with respect to the earth equatorial plane. It appears that at high inclinations some advantage is taken of earth rotation rate in determining $GM_\oplus$. Since this is a geometrical effect, it does not have very much significance for long tracking intervals.

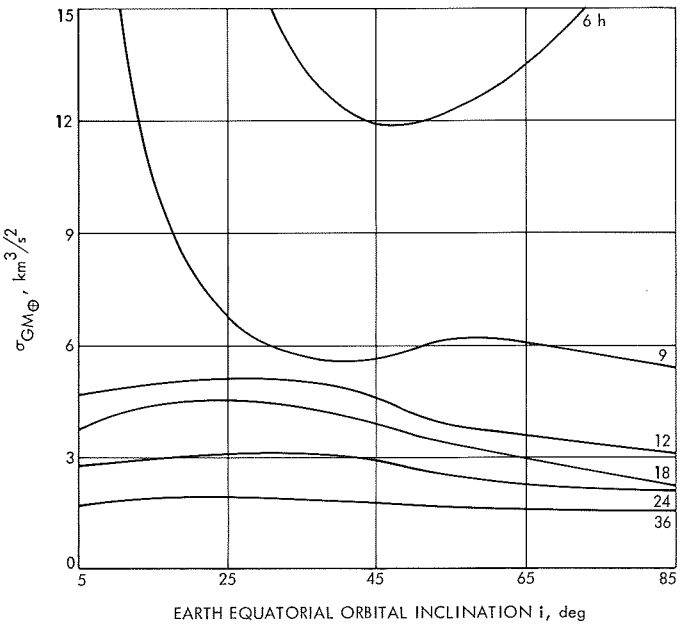

Fig. 67. $GM_\oplus$ standard deviation as a function of orbital inclination for various tracking intervals

The effect of varying the longitude of the ascending node of the standard orbit is shown in Fig. 68. For this particular tracking station configuration, the primary effect is a degradation in the early determination of $GM_\oplus$ in the vicinity of $\Omega = 250°$. As the plot shows, this geometrical effect can be quite important for the first 9 h of tracking. Presumably, however, in actually attempting to determine $GM_\oplus$ from satellite tracking, one would be free to choose a data block containing favorable tracking geometry. This may be an important advantage of an orbiter as opposed to a lunar or planetary probe.

e. Conclusions. The primary desirable orbital characteristic for accurately determining $GM_\oplus$ from the doppler tracking of a satellite appears to be a low perigee altitude. In this class, satellites having a large semimajor axis and high eccentricity seem to be more suitable than those with a small semimajor axis and low eccentricity. The closeness of perigee is limited, of course, by the height of the atmosphere. Since it is not possible to accurately model atmospheric drag, perigee must be substantially above the atmosphere if the satellite is to be used for determining $GM_\oplus$. In such a determination, a very careful modeling of earth gravitational harmonics is also necessary. In addition, the data span must be limited to prevent the solution from being corrupted by process noise resulting from solar radiation pressure uncertainty and attitude-control accelerations. This is why this study was restricted to data spans of 36 h or less. If these conditions are fulfilled, it appears that $GM_\oplus$ standard deviations of the order of 0.2 km^3/s^2 are obtainable from doppler tracking of earth satellites, which is comparable to the accuracy obtainable from the *Ranger* lunar missions or the *Mariner* planetary missions.

References

1. Sjogren, W. L., et al., *Physical Constants as Determined from Radio Tracking of the Ranger Lunar Probes.* Technical Report 32-1057, p. 11. Jet Propulsion Laboratory, Pasadena, Calif., Dec. 30, 1966.
2. Pease, G., et al., *The Mariner V Flight Path and its Determination from Tracking Data,* Technical Report 32-1363, p. 7. Jet Propulsion Laboratory, Pasadena, Calif., July 1, 1969.

13. MLSP—The Multiple-Link Satellite Program,

D. W. Green

a. Introduction. In connection with recent JPL studies of a Tracking and Data Relay Satellite Network, a need became apparent for a computer program to study the statistics of satellite orbit determinations using data types involving several satellites. As the current JPL orbit determination programs generate data for only a single satellite at a time, a program was necessary either to combine the output of present JPL programs or to generate data for multiple satellites simultaneously. For

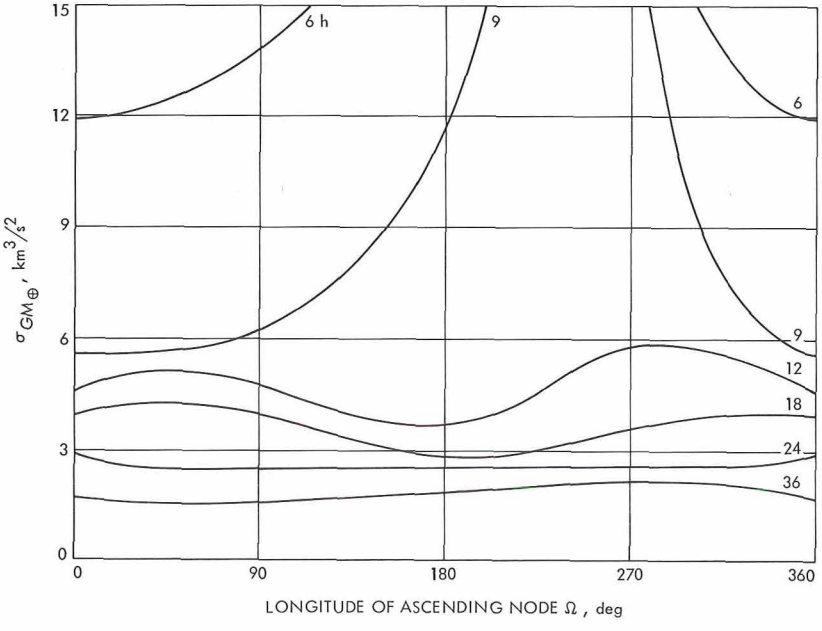

Fig. 68. $GM_\oplus$ standard deviation as a function of longitude of ascending orbital node for various tracking intervals

various reasons, the latter approach was chosen. The resulting program is called the Multiple-Link Satellite Program (MLSP).

The MLSP assumes that the orbit determination process will be done with radio ranging and/or doppler data. Unlike current orbit determination programs, however, the MLSP does not confine the signal path to direct ground station-to-satellite measurements but allows the signal to be relayed many times, including relays between satellites. In particular, the program accepts any sequence of ground stations and satellites as a path for a radio signal with two exceptions. Paths which contain two consecutive ground stations and paths for which a proper subset forms a closed loop are not allowed.

b. Satellite and ground station dynamic model. For reasons of economy both in programming and operating time, very simple dynamic models are used in the MLSP. The satellites move in strict two-body Keplerian orbits. The ground stations move on an earth which is rotating at an exactly uniform rate about a fixed axis. Specifically, the system takes no account of irregularities in the earth's geopotential, perturbations due to moon, sun, and other planets, irregularities in the earth's rotation and polar motion, solar pressure and spacecraft attitude-control effects, atmospheric drag, or atmospheric and ionospheric effects on signal propagation.

c. Mathematical formulation. The MLSP assumes that the satellite orbit determination process will be performed using a linearized, weighted, least-squares solution for the satellites' classical orbital elements. If an observable quantity O depends on a set of parameters q_i and time, we can write

$$O = F(q_1, q_2, \cdots, q_I, t)$$

and, if an initial guess q_{i0} is made, O can be expressed as a series expansion

$$O = F(q_{10}, q_{20}, \cdots, q_{I0}, t) + \sum_{i=1}^{I} \frac{\partial F(q_{10}, q_{20}, \cdots, q_{I0}, t)}{\partial q_i} (q_i - q_{i0}) + \text{terms of order } (q_i - q_{i0})^2$$

Any real observation will be contaminated with measurement noise, and repeated observations will be required in order to solve for all of the required parameters and to reduce the effects of the observational noise. If a set of observations are made at times t_j, we may write

$$\mathbf{y} = A\mathbf{x} + \boldsymbol{\varepsilon} \tag{1}$$

where

$\mathbf{y}$ = column vector of dimension J, the number of observations taken, and

$$y_j = O(t_j) - F(q_{10}, q_{20}, \cdots, q_{I0}, t_j)$$

that is, y is the actual observed value at each time minus the expected value of the quantity based on an initial guess for the parameters upon which it depends

A = matrix of the partial derivatives of the observable quantity evaluated at the nominal values of each parameter and at each observation time, i.e.,

$$a_{ij} = \frac{\partial F(q_{10}, q_{20}, \cdots, q_{I0}, t_j)}{\partial q_i}$$

$\mathbf{x}$ = column vector of differences between the nominal values of the parameters q_i and their true values

$\boldsymbol{\varepsilon}$ = vector of the noise on each measurement

Terms of order $\mathbf{x}^T\mathbf{x}$ have been ignored.

It will be stated here without proof that a minimum variance solution to such a system of equations is

$$\hat{\mathbf{x}} = (A^T\Lambda_\varepsilon^{-1}A)^{-1}A^T\Lambda_\varepsilon^{-1}\mathbf{y} \tag{2}$$

where A and $\mathbf{y}$ are as defined above and Λ_ε is the covariance matrix of noise on observations.

The resulting covariance matrix on the solution is

$$\Lambda_x = (A^T\Lambda_\varepsilon A)^{-1} \tag{3}$$

If more than one observable is used in a solution and if an *a priori* covariance matrix Γ_0 exists for the solution,

$$\Lambda_x = \left(\Gamma_0^{-1} + \sum_{k=1}^{K} A_k^T \Lambda_{\varepsilon k}^{-1} A_k\right)^{-1} \tag{4}$$

where A_k and $\Lambda_{\varepsilon k}$ are the quantities A and Λ_ε defined in Eqs. (1) and (2) for the kth observable.

In particular, if the noise on each observable is uncorrelated in time,

$$A_k^T \Lambda_{\varepsilon k}^{-1} A_k = \frac{1}{\sigma_{\varepsilon k}^2} \sum_{j=1}^{J} a_{jk}^T a_{jk}$$

where

$\sigma_{\varepsilon k}^2$ = variance of noise on each observation of the kth observable

$\mathbf{a}_{jk}$ = vector of partials of the kth data type at time t_j with respect to the parameters q_i

This allows the matrix Λ_x to be written

$$\Lambda_x = \left(\Gamma_0^{-1} + \sum_{j=1}^{J} \sum_{k=1}^{K} \frac{1}{\sigma_{\varepsilon k}^2} a_{jk}^T a_{jk} \right)^{-1} \tag{5}$$

and hence to be accumulated serially in time.

If the observables depend on parameters which are known imprecisely and it is desired to determine the effect of the uncertainty in those parameters (the so-called considered parameters), the covariance matrix of the solution is given by

$$\bar{\Lambda}_x = \Lambda_x + \Lambda_x M \Lambda_p M^T \Lambda_x^T \tag{6}$$

where

$$M = \sum_k A_k^T \Lambda_{\varepsilon k}^{-1} B_k$$

and

B_k = matrix of partials of kth observable with respect to uncertain parameters

Λ_p = covariance matrix of *a priori* uncertainties of uncertain parameters

$\bar{\Lambda}_x$ = total covariance matrix

The observables in the MLSP consist of range and range rate along a path connecting a series of ground stations and satellites. These observables are computed as

$$\rho_{123\cdots n-1\,n} = \rho_{12} + \rho_{23} + \cdots + \rho_{n-1\,n}$$

$$\dot{\rho}_{123\cdots n-1\,n} = \dot{\rho}_{12} + \dot{\rho}_{23} + \cdots + \dot{\rho}_{n-1\,n}$$

The partial derivatives are

$$\frac{\partial \rho_{123\cdots n-1\,n}}{\partial q} = \frac{\partial \rho_{12}}{\partial q} + \frac{\partial \rho_{23}}{\partial q} + \cdots + \frac{\partial \rho_{n-1\,n}}{\partial q}$$

$$\frac{\partial \dot{\rho}_{123\cdots n-1\,n}}{\partial q} = \frac{\partial \dot{\rho}_{12}}{\partial q} + \frac{\partial \dot{\rho}_{23}}{\partial q} + \cdots + \frac{\partial \dot{\rho}_{n-1\,n}}{\partial q}$$

i.e., range and/or range rate along a total path equals the sum of range and/or range rate between each sequential pair of vertices along that path.

For any sequential pair of points,

$$\rho_{12} = (\mathbf{R}_{12} \cdot \mathbf{R}_{12})^{1/2}$$

$$\dot{\rho}_{12} = (\dot{\mathbf{R}}_{12} \cdot \mathbf{R}_{12})/\rho_{12}$$

$$\frac{\partial \rho_{12}}{\partial q} = \left(\frac{\partial \mathbf{R}_{12}}{\partial q} \cdot \mathbf{R}_{12} \right)/\rho_{12}$$

$$\frac{\partial \dot{\rho}_{12}}{\partial q} = \left(\frac{\partial \dot{\mathbf{R}}_{12}}{\partial q} \cdot \mathbf{R}_{12} + \dot{\mathbf{R}}_{12} \cdot \frac{\partial \mathbf{R}_{12}}{\partial q} - \frac{\partial \rho_{12}}{\partial q} \cdot \rho_{12} \right) / \dot{\rho}_{12}$$

where

$$\mathbf{R}_{12} = \mathbf{x}_2 - \mathbf{x}_1$$

$$\dot{\mathbf{R}}_{12} = \dot{\mathbf{x}}_2 - \dot{\mathbf{x}}_1$$

$$\frac{\partial \mathbf{R}_{12}}{\partial q} = \frac{\partial \mathbf{x}_2}{\partial q} - \frac{\partial \mathbf{x}_1}{\partial q}$$

$$\frac{\partial \dot{\mathbf{R}}_{12}}{\partial q} = \frac{\partial \dot{\mathbf{x}}_2}{\partial q} - \frac{\partial \dot{\mathbf{x}}_1}{\partial q}$$

and

ρ_{12} = range from point 1 to 2

$\dot{\rho}_{12}$ = range rate from point 1 to 2

$\mathbf{R}_{12}$ = vector from point 1 to 2

$\dot{\mathbf{R}}_{12}$ = time derivative of vector from point 1 to 2

$\mathbf{x}_2, \mathbf{x}_1$ = cartesian coordinates of points 1 and 2, respectively

q = parameter on which position 1 and/or 2 depends

For satellites, the parameters upon which position depends are:

a the semimajor axis

e the eccentricity

t_0 time of first perifocal passage

θ the longitude of the node

ϕ the argument of perigee

i the equatorial inclination

GM_e the gravitational mass constant of the earth

The position is given by

$$\mathbf{x} = M\mathbf{u}$$

where M is the matrix

$$\begin{pmatrix} \cos\theta\cos\phi - \sin\theta\sin\phi\cos i & -\cos\theta\sin\phi - \sin\theta\cos\phi\cos i \\ \sin\theta\cos\phi + \cos\theta\sin\phi\cos i & -\sin\theta\sin\phi + \cos\theta\cos\phi\cos i \\ \sin i\sin\phi & \sin i\cos\phi \end{pmatrix}$$

and $\mathbf{u}$ is the two-vector

$$\mathbf{u} = \begin{pmatrix} u \\ v \end{pmatrix} = \begin{pmatrix} a\cos E - e \\ a(1-e^2)^{1/2}\sin E \end{pmatrix}$$

The quantity E is the solution to Kepler's equation

$$(GM_e)^{1/2} a^{-3/2}(t - t_0) = E - e\sin E$$

The matrix M is not time dependent so

$$\dot{\mathbf{x}} = M\dot{\mathbf{u}}$$

and

$$\frac{\partial x}{\partial q} = \frac{\partial M}{\partial q}\mathbf{u}, \qquad q = \theta, \phi, i$$

$$\frac{\partial \mathbf{x}}{\partial q} = M\frac{\partial \mathbf{u}}{\partial q}, \qquad q = a, e, t_0, GM_e$$

$$\frac{\partial \dot{x}}{\partial q} = \frac{\partial M}{\partial q}\dot{\mathbf{u}}, \qquad q = \theta, \phi, i$$

$$\frac{\partial \dot{\mathbf{x}}}{\partial q} = M\frac{\partial \dot{\mathbf{u}}}{\partial q}, \qquad q = a, e, t_0, GM_e$$

Finally, due to the introduction of the parameter E,

$$\frac{\partial u}{\partial q} = \frac{\partial u}{\partial q} + \frac{\partial u}{\partial E}\cdot\frac{\partial E}{\partial q}$$

$$\frac{\partial \dot{u}}{\partial q} = \frac{\partial \dot{u}}{\partial q} + \frac{\partial \dot{u}}{\partial E}\cdot\frac{\partial E}{\partial q} + \frac{\partial \dot{u}}{\partial \dot{E}}\left(\frac{\partial \dot{E}}{\partial q} + \frac{\partial \dot{E}}{\partial E}\cdot\frac{\partial E}{\partial q}\right)$$

$$q = a, e, t_0, GM_e$$

$$\dot{E} = \frac{(GM_e)^{1/2} a^{-3/2}(t - t_0)}{1 - e\cos E}$$

For ground stations, the position depends on the parameters

R radius from center of earth
L latitude
λ longitude

Thus,

$$\mathbf{x} = \begin{pmatrix} R\cos L\cos(\omega t + \lambda) \\ R\cos L\sin(\omega t + \lambda) \\ R\sin L \end{pmatrix}$$

where ω is the rotation rate of earth.

A particular data type is occulted if the ray path between any pair of sequential points along the path intersects the surface of the earth. For satellite-to-ground station links, the occultation formula is

$$A = (\mathbf{x}_s - \mathbf{x}_G)\cdot(\mathbf{x}_s - \mathbf{x}_G)$$

$$Q = \sin^2(E) - \frac{1}{4}\frac{A}{|\mathbf{x}_s|^2}\cdot\frac{A}{|\mathbf{x}_G|^2}$$

where $\mathbf{x}_s$ is the satellite position, $\mathbf{x}_G$ the ground station position, and E the minimum elevation angle for station. Occultation occurs if $Q \leq 0$.

For satellite-to-satellite links

$$Q = [\mathbf{x}_2\cdot(\mathbf{x}_2 - \mathbf{x}_1)]^2 - |\mathbf{x}_2 - \mathbf{x}_1|^2\cdot(|\mathbf{x}_2|^2 - R_e^2)$$

where $\mathbf{x}_1$, $\mathbf{x}_2$ are satellite positions and R_e is the radius of the earth. Occultation occurs if $Q > 0$.

In addition to the covariance matrix of the classical Keplerian elements, the MLSP will produce a covariance

matrix on the instantaneous cartesian coordinate position at time x_j via the transformation

$$\Lambda_x = \frac{\partial x(t_j)^T}{\partial a} \Lambda_a \frac{\partial x(t_j)}{\partial a}$$

where a is the set of parameters a, e, t_0, θ, ϕ, i, GM_e.

d. Capacity and limitations. The current capacities and limitations of the MLSP include:

Parameter	Maximum number
Satellites	20
Ground stations	10
Links per data type	15
Data types	24
Solve-for parameters	24
Consider parameters	24

e. Applications. The MLSP has thus far been used for two applications, a study of the accuracy with which the gravitational mass constant of the earth can be determined (see previous article, *Subsection 12*, and a study of the accuracy with which a target satellite can be tracked via an orbiting tracking relay.[23]

14. Differenced-Range Doppler Versus Integrated Doppler, T. D. Moyer

a. Introduction. This study demonstrates the feasibility of computing doppler observables from differenced-range observables divided by the count time. The changes specified for the Univac 1108 version of the double-precision orbit determination program (DPODP) should produce "differenced-range" doppler (DRD) accurate to 10^{-5} m/s or better for all count times above 0.2 s. The primary analytical change is a more accurate expression for the relativistic transformation from coordinate time (ephemeris time, ET) to proper time (atomic time, A1). Specifically, the coefficient of one of the two existing terms has been changed and six new terms have been added (see Eq. 16). The increase in numerical precision from the 16-decimal digits of the IBM 7094 to the 18-decimal digits of the Univac 1108 is required; also, the precision of representation of time must be increased from double- to triple-precision seconds past 1950.[24] It is also recommended that the current type 50 n-body ephemeris be replaced by the more accurate type 66 ephemeris or equivalent.

The doppler observables are currently computed by expanding the frequency shift in a Taylor series and averaging over the count time. The primary advantage of DRD is that there is no upper limit to the count interval, whereas with the current "integrated" doppler (ID) formulation, count times are limited to approximately 1000 s in heliocentric cruise due to truncation of the fourth and higher derivatives of the frequency shift in the Taylor series expansion. The partial derivatives of the DRD observables with respect to the estimated parameters $\mathbf{q}$ will be computed from differences of the partial derivatives of the two range observables (used to compute DRD) with respect to $\mathbf{q}$. The use of DRD will reduce running time since the formulation is simpler and because fewer observables will be computed (since larger count times will be used). Furthermore, the coding will be simplified and reduced in volume since the DRD formulation draws heavily upon the existing range observable formulation.

It is recommended that the DRD formulation be incorporated into the forthcoming Univac 1108 version of the DPODP as an alternate option to the existing ID formulation. This will allow a direct comparison of fits to real data with the two different formulations. If the DRD formulation proves itself, the ID formulation will be removed from the program.

Starting with the definitions of range and doppler observables, it is shown in *Paragraph b* that two-way doppler may be computed from differenced round-trip range observables divided by the count time. The DPODP runs, which produced range and doppler observables, and program DRDVID,[25] which used these observables to compute DRDVID residuals, are described in *Paragraph c.* Residuals were obtained for the *Mariner V* mission and for the first leg of a grand tour mission at 1, 2, 3, 4, and 5 AU and at encounter with Jupiter. The new expression for the ET−A1 time transformation is given in *Paragraph d.* In *Paragraph e*, the error sources affecting DRD and ID are discussed and are related to the DRD−ID residual versus count time plots.

[23] *Tracking and Data Relay Satellite Network (TDRSN) Final Study Report,* Chap. II, Section 4, Sept. 30, 1969 (JPL internal document).

[24] Alternately, time could be represented as one-single-precision word (8-decimal digits) for the Julian day number plus one double-precision word (18-decimal digits) for seconds past the beginning of the day.

[25] DRDVID = differenced-range doppler versus integrated doppler.

The range observables computed by the IBM 7094 version of the DPODP contain a random error of a few millimeters due to truncation of time (seconds past 1950) beyond 16-decimal digits.[26] The corresponding error in DRD is a maximum of 3×10^{-3} m divided by the count time. For DRD accurate to 10^{-5} m/s, the minimum allowable count time is 300 s. If the representation of time is changed from double precision to triple precision, the random error in the computed range observable is reduced to the smaller error due to truncation of position beyond double precision. On the forthcoming Univac 1108 version of the DPODP, which has a word length of 18-decimal digits, the position truncation error will be 10^{-6} m for range up to 7 AU. The corresponding error in DRD is 2×10^{-6} m divided by the count time, or 10^{-5} m/s or less for count times of 0.2 s or greater.

In the computation of the range observables used to compute DRD, the new terms of the ET−A1 time transformation are required to accurately transform round-trip ephemeris time from the light time solution to observed round-trip station time. The effect on the range observables is less than 2 m/AU. However, the corrections vary rapidly (with periods of 1 day or 1 mo) and the effect on the DRD observables of this study is as large as 3×10^{-4} m/s. The maximum effect of a periodic term of ET−A1 on DRD is the second time derivative of the term multiplied by the probe range. In the derivation of the new terms of ET−A1, all terms affecting DRD by more than 2×10^{-7} m/s per AU of distance to the spacecraft were retained. Several terms of this magnitude were neglected and the resulting error in DRD has a maximum value of about 10^{-6} m/s/AU or 10^{-5} m/s for a range of 10 AU. No correction is required to the ID observable formulation since it contains the exact differential equation relating proper time to coordinate time.

The pre-computed n-body ephemeris tapes used by the DPODP are of the so-called type 50 format. They contain modified second and fourth central differences of position and velocity. Interpolation is obtained by the fifth-order Everett's formula. Both the velocity interpolation error, which affects ID, and the differenced position interpolation error divided by the count time, which affects DRD, can approach 10^{-5} m/s. This small error could be eliminated by converting to the type 66 n-body ephemeris tape format, which contains the full sum and difference array (on acceleration) used to generate the ephemeris. The heliocentric velocity of the spacecraft is affected by errors in interpolation of the heliocentric ephemeris of the center of integration for the probe trajectory, while errors in interpolation of the heliocentric ephemeris of the earth–moon barycenter affect the heliocentric velocity of the tracking station.

b. Equivalence of differenced-range and integrated two-way doppler. From SPS 37-42, Vol. III, pp. 15–21, the output from the electronic equipment at the tracking station is a signal whose frequency f in cycles per second of station time is

$$f = C_3\left[f_q(t_3) - f_q(t_1)\left(\frac{f_R}{f_T}\right)\right] + C_4 \qquad (1)$$

where

$f_q(t_3), f_q(t_1)$ = transmitter reference oscillator frequency at reception time t_3 and transmission time t_1, respectively (generally identical unless f_q has been changed between t_1 and t_3)

f_R/f_T = ratio of received to transmitted frequency for unity frequency multiplication at spacecraft

$$C_3 = \begin{cases} 30\left(\frac{96}{89}\right), & \text{L-band} \\ 96\left(\frac{240}{221}\right), & \text{S-band} \end{cases}$$

$$C_4 = \begin{cases} 10^5, & \text{L-band} \\ 10^6, & \text{S-band} \end{cases}$$

The transmitted frequency is 30 or 96 times the reference oscillator frequency for L- or S-band operation. The spacecraft transponder multiplies the frequency of the received signal by 96/89 or 240/221 for L- or S-band operation before retransmitting. The expression for f may be written as

$$f = C_3 f_q(t_1)\left(1 - \frac{f_R}{f_T}\right) + f_{\text{bias}} \qquad (2)$$

where

$$f_{\text{bias}} = C_3\left[f_q(t_3) - f_q(t_1)\right] + C_4 \qquad (3)$$

Note that the first term of f_{bias} normally is zero.

[26]Time is represented as double-precision (54 bits on the IBM 7094 computer) seconds past January 1, 1950,0^h. From 1967 to 1984, the value of the last bit is 0.6×10^{-7} s. The transmission time, reflection time at the spacecraft, and reception time (in ephemeris time) obtained from the light time solution may be in error by about this amount. Hence, for a probe range rate of 30 km/s, the error in computed range will be about 30 km/s $\times$ 10^6 mm/km $\times$ 0.6×10^{-7} s = 1.8 mm.

The signal with frequency f is fed into an electronic counter whose register is incremented by 1 each time the amplitude of the signal changes from minus to plus. N cycles are counted during the count time T_c. The two-way doppler observable which the data editing program passes on to the orbit determination program is

$$F2 = \frac{N}{T_c} - f_{\text{bias}} \tag{4}$$

Since N is the integral of f over the count time,

$$F2 = \frac{1}{T_c}\int_{t_3-\frac{1}{2}T_c}^{t_3+\frac{1}{2}T_c} f d\tau - f_{\text{bias}} \tag{5}$$

where

$\tau =$ station time (proper time) at tracking station, from station atomic clock

$t_3 =$ epoch at midpoint of count interval T_c

Substituting Eq. (2) into Eq. (5) gives

$$F2 = \frac{C_3 f_q(t_1)}{T_c}\int_{t_3-\frac{1}{2}T_c}^{t_3+\frac{1}{2}T_c}\left(1 - \frac{f_R}{f_T}\right) d\tau \tag{6}$$

"Integrated" two-way doppler may be obtained from Eq. (6) by expanding $1 - (f_R/f_T)$ in a Taylor series with coefficients evaluated at t_3. Equation (6) may then be integrated term by term. The odd derivatives vanish, and the fourth and higher derivatives are ignored. The resulting expression for $F2$ is

$$F2 = C_3 f_q(t_1)\left[\left(1 - \frac{f_R}{f_T}\right) + \frac{T_c^2}{24}\left(1 - \frac{f_R}{f_T}\right)^{\cdot\cdot}\right] \tag{7}$$

where $1 - (f_R/f_T)$ and its second derivative with respect to station time $[1 - f_R/f_T)]^{\cdot\cdot}$ are evaluated at the midpoint of the count interval. The first term, which has been truncated in Eq. (7), is $(1/1920)\,(T_c^4)\,[1 - (f_R/f_T)]^{\text{iv}}$. In order to limit the truncation error in Eq. (7) to 10^{-5} m/s, the count time T_c must be limited to approximately 1 s for near-earth spacecraft, and to approximately 1000 s when the spacecraft is in heliocentric cruise.

The expression for "differenced-range" two-way doppler may also be obtained from Eq. (6). The ratio of received to transmitted frequency is

$$\frac{f_R}{f_T} = \frac{dn}{d\tau_3}\cdot\frac{d\tau_1}{dn} = \frac{d\tau_1}{d\tau_3} \tag{8}$$

where

$dn =$ infinitesimal number of cycles transmitted and received

$d\tau_1 =$ infinitesimal period (of proper time τ) of transmission of dn cycles from tracking station at time t_1

$d\tau_3 =$ infinitesimal period (of proper time τ) of reception of dn cycles at tracking station at time t_3

Substituting Eq. (8) into Eq. (6) and denoting $d\tau$ in Eq. (6) as $d\tau_3$ gives

$$F2 = \frac{C_3 f_q(t_1)}{T_c}\int_{t_3-\frac{1}{2}T_c}^{t_3+\frac{1}{2}T_c}\left(1 - \frac{d\tau_1}{d\tau_3}\right) d\tau_3 \tag{9}$$

The count time T_c is an interval of reception time; the corresponding transmission interval is denoted T_c', and has midpoint t_1. Thus,

$$F2 = \frac{C_3 f_q(t_1)}{T_c}\left[\int_{t_3-\frac{1}{2}T_c}^{t_3+\frac{1}{2}T_c} d\tau_3 - \int_{t_1-\frac{1}{2}T_c'}^{t_1+\frac{1}{2}T_c'} d\tau_1\right]$$

$$= \frac{C_3 f_q(t_1)}{T_c}(T_c - T_c') \tag{10}$$

The four station time epochs corresponding to the start and end of the transmission and reception intervals T_c' and T_c are denoted as

$\tau_{3_e} =$ end of reception interval T_c

$\tau_{3_s} =$ start of reception interval T_c

$\tau_{1_e} =$ end of transmission interval T_c'

$\tau_{1_s} =$ start of transmission interval T_c'

Also, "range" ρ corresponding to reception time τ_3 and transmission time τ_1 is defined as elapsed round-trip proper time:

$$\rho(\tau_3) \equiv \tau_3 - \tau_1$$

and

$$\rho_e \equiv \tau_{3_e} - \tau_{1_e}$$

$$\rho_s \equiv \tau_{3_s} - \tau_{1_s}$$

Thus,

$$T_c - T'_c = (\tau_{3_e} - \tau_{3_s}) - (\tau_{1_e} - \tau_{1_s}) = \rho_e - \rho_s \tag{11}$$

Substituting Eq. (11) into Eq. (10) gives

$$F2 = C_3 f_q(t_1)\left[\frac{\rho_e - \rho_s}{T_c}\right] \tag{12}$$

The DPODP range observables R, RD, and RT are computed as round-trip station time ρ multiplied by a conversion factor F and modulated by modulo number M:

R (kilometers/2): $F = \frac{c}{2}$

M = no modulo number

RD (range units): $F = \frac{1440}{221} f_q(t_1)$

$M = 785{,}762{,}208$

RT (nanoseconds): $F = 10^9$

$M = 1.00947 \times 10^9/1.0002$

$= 1.009{,}268{,}146{,}370{,}725{,}8548 \times 10^9$

where c = speed of light = 299,792.5 km/s, and one range unit $\approx$ 1 m of distance to the spacecraft. The observable R is obtained from the AFETR pulse radar ranging system. The observables RD and RT are obtained from the DSIF Mark 1A and R&D planetary ranging systems, respectively.

The DRD observables of this study were computed from differenced round-trip range R (in units of kilometers divided by two):

$$F2 = \frac{2C_3 f_q(t_1)}{c}\left[\frac{R_e - R_s}{T_c}\right] \tag{13}$$

The conversion factor CON between two-way doppler (integrated or differenced-range) in observed units of Hz and in units of one-way meters/s is

$$CON = \frac{F2\,(\text{Hz})}{F2\,(\text{1-way meters/s})} = \frac{2C_3 f_q(t_1)(\text{Hz})}{c\,(\text{meters/s})} \tag{14}$$

$$= 15.343{,}946{,}229{,}475{,}39\ \text{Hz/(1-way meters/s)}$$

since the observables of this study were computed with $C_3 f_q(t_1) = 2300 \times 10^6$ Hz exactly and $c = 2.997925 \times 10^8$ m/s.

c. Generation of differenced-range doppler minus integrated doppler residuals. The DPODP was used to compute the round-trip range observable R (round-trip time multiplied by one-half the speed of light c) and two-way doppler $F2$ at each of three successive observation times, with a data spacing equal to half of the count time T_c. Differenced-range doppler was computed from the range observables R_e and R_s at the third and first observation times, respectively, and compared to two-way doppler at the second observation time. The computations were performed by program DRDVID. The equivalence of integrated and differenced-range two-way doppler is given by Eq. (13). The residual RES in m/s computed by DRDVID is

$$RES = \frac{1000\,[R_e(\text{km}) - R_s(\text{km})]}{T_c} - \frac{F2(\text{Hz})}{CON} \tag{15}$$

where CON is given by Eq. (14).

The doppler corrections due to antenna motion, troposphere, and ionosphere are in the form of differenced-range corrections divided by the count time; hence, all observables were computed without applying these corrections. It is noted that the sign of the ionospheric range correction must be changed when the range observable is used to compute DRD.

d. New expression for ET − A1 time transformation. Given a system of synchronized (on the average) A1 atomic clocks, one at each tracking station, the new expression for ET minus A1 obtained from any of the clocks (in seconds) is

$$
\begin{aligned}
\text{ET}-\text{A1} = {} & \Delta T_{1958} \\
& - (\text{JD} - 2436204.5)\,(86400)\,\frac{\Delta f_{\text{cesium}}}{f_{\text{cesium}}} \\
& + 1.658 \times 10^{-3} \sin E && [\text{AT}] \\
& + 0.317679 \times 10^{-9} r_s \sin(\text{UT} + \lambda) && [\text{DA1} + \text{DP}] \\
& + 5.341 \times 10^{-12} r_s \sin(\text{UT} + \lambda - M) && [\text{DA1(e)}] \\
& + 1.01 \times 10^{-13} r_s \sin(\text{UT} + \lambda - 2M) && [\text{DA1}(e^2)] \\
& - 1.3640 \times 10^{-11} r_s \sin(\text{UT} + \lambda + 2L) && [\text{DA2}] \\
& - 2.27 \times 10^{-13} r_s \sin(\text{UT} + \lambda + 2L + M) && [\text{DA2(e)}] \\
& + 1.672 \times 10^{-6} \sin D && [\text{AM}] \\
& + 1.38 \times 10^{-13} r_s \sin(\text{UT} + \lambda - D) && [\text{DM}]
\end{aligned}
\qquad \text{Term identification} \qquad (16)
$$

The first and second terms account for the initial setting and rate of the A1 atomic time scale relative to ET; the remaining terms account for the periodic relativistic variations in A1 atomic time relative to uniform ET. The variables in Eq. (16) are defined as

ΔT_{1958} = ET − UT2 on January 1, 1958, $0^h\,0^m\,0^s$ UT2 minus the periodic terms of Eq. (16) evaluated at this epoch using r_s and λ of the master A1 clock. The master A1 clock was set equal to UT2 on this date. The parameter ΔT_{1958} may be estimated by the DPODP.

f_{cesium} = 9192631770 cycles of cesium atomic clock per second of A1 time (definition). This adopted length of the A1 second is the current experimentally determined average length of the ET second.

$f_{\text{cesium}} + \Delta f_{\text{cesium}}$ = cycles of cesium atomic clock per ephemeris second. The parameter Δf_{cesium} may be estimated by the DPODP; its current nominal value is zero.

2436204.5 = Julian date on January 1, 1958, 0^h.

JD = Julian date.

M = mean anomaly of heliocentric orbit of earth–moon barycenter.

E = eccentric anomaly of heliocentric orbit of earth–moon barycenter.

L = geometric mean longitude of the sun, referred to mean equinox and ecliptic of date.

$D = \mathbb{C} - L$ = mean elongation of the moon from the sun, where

$\mathbb{C}$ = mean longitude of the moon, measured in the ecliptic from the mean equinox of date to the mean ascending node of the lunar orbit, and then along the orbit.

r_s = distance of tracking station from earth's spin axis, km.

λ = east longitude of tracking station.

UT = universal time, hours past midnight, converted to radians. It is computed from

$$\text{UT} = 2\pi \left[\frac{\text{UT1}}{86400} \right]_{\text{decimal part}} \qquad (17)$$

where UT1 = seconds of UT1 time past January 1, 1950, 0^h UT1. The angles M, L, and D in radians are given by

$$M = 6.248,291 + 1.990,968,71 \times 10^{-7}\, t \qquad (18)$$

$$L = 4.888,339 + 1.991,063,83 \times 10^{-7}\, t \qquad (19)$$

$$D = 2.518,410 + 2.462,600,818 \times 10^{-6}\, t \qquad (20)$$

where t = seconds past January 1, 1950, 0^h. To a sufficient degree of accuracy, the eccentric anomaly E is given by

$$E \approx M + e \sin M \tag{21}$$

where e = eccentricity of heliocentric orbit of earth–moon barycenter = 0.01672.

The eight periodic relativity terms in Eq. (16) were obtained by integrating Eq. (13) of SPS 37-42, Vol. III, pp. 15–21. The derivation will be included in a forthcoming JPL Technical Report on the DPODP formulation. Term AT arises from the annual variation in velocity and potential at the tracking station. The second term is the sum of terms DA1 and DP with coefficients of 0.318549 and −0.000870, respectively. Terms DA1, DA1(e), DA1(e^2) DA2, DA2(e) arise from the product of the daily and annual components of the heliocentric station velocity in the expression for the station velocity squared ($\dot{s}^2$) in Eq. (13) of SPS 37-42, Vol. III. Terms DA1 and DA2 account for the mean motion of the earth–moon barycenter about the sun. Terms DA1(e) and DA2(e) are first-order eccentricity terms while term DA1(e^2) is a second-order eccentricity term. Term DP accounts for the daily variation in potential at the station. Term AM stems from the product of the annual and monthly components of station velocity in $\dot{s}^2$, while term DM is due to the product of the daily and monthly components.

The expression for ET − A1 currently used in the DPODP consists of the first three terms of Eq. (16) and the following term derived by Anderson (SPS 37-50, Vol. III, pp. 39–47):

$$2.03 \times 10^{-6} \cos \phi \sin (\mathrm{UT} + \lambda) \qquad [\mathrm{DT}]$$

where ϕ is the station latitude. Anderson's term is term DA1 of Eq. (16) (coefficient = 0.318549) with r_s set equal to 6372 km cos ϕ. Computation of the daily terms of Eq. (16) from the station's spin axis distance rather than latitude accounts for the effect of the earth's flattening. The increased accuracy is required for the computation of DRD.

e. Residual plots. Differenced-range doppler minus integrated doppler (DRD − ID) residuals were obtained for the *Mariner V* trajectory early and late in heliocentric cruise, and at encounter with Venus (10,000-km radius of closest approach), and also on the first leg of a grand tour mission at 1, 2, 3, 4 and 5 AU and at encounter with Jupiter (125,000-km radius of closest approach). The DRD − ID residuals are plotted as a function of count time T_c in Figs. 69, 70, and 71. For each curve, the epoch at the midpoint of the count interval is held fixed.

Figure 69 shows DRD − ID residuals for three different observation times on the *Mariner V* trajectory to Venus. Each observable is computed with 24 different count times ranging from 0.1 to 10,000 s. For count times below approximately 100 s, the residuals are random with an upper limit of about 3 mm/T_c. These residuals represent errors in the range observables used to compute DRD due to truncation of time (seconds past 1950) beyond double precision on the IBM 7094 computer (54 bits or approximately 16-decimal digits). The randomness of the residuals is expected since the range observables and hence their time truncation errors change with the count time. It can be shown that if each of several contributing time truncation errors were at their upper limits, DRD could be in error by as much as 10 mm/T_c. Figure 70 shows the variation in the *Mariner V* residuals with integration central body on October 6, 1967 at 16 h UTC. Figure 71 shows residuals for the first leg of a grand tour mission at 1, 2, 3, 4, and 5 AU and at encounter with Jupiter. These figures have a typical residual of 1 mm/T_c due to truncation of time beyond double precision.

Integrated two-way doppler is computed from Eq. (7), which was obtained from Eq. (6) by expanding the doppler frequency shift in a Taylor series (with coefficients evaluated at the midpoint of the count interval T_c) and integrating term by term. The odd derivatives of the frequency shift vanish and the fourth and higher derivatives are ignored. The first deleted term in Eq. (7) is

$$(1/1920)T_c^4 [1 - (f_R/f_T)]^{\mathrm{iv}}$$

where iv represents the fourth derivative with respect to the reception time (station time). For an accuracy of 10^{-5} m/s, truncation of the fourth derivative of the frequency shift limits the count time to approximately 1000 s in heliocentric cruise and typically 1 to 60 s at planetary encounter depending upon the radius of closest approach. Thus, on the log residual versus log count time plots, the residuals should rise linearly with a slope of four at high count times. This is exactly what is obtained in Figs. 69, 70, and 71.

For heliocentric cruise on the *Mariner V* and Jupiter trajectories, the doppler truncation residuals rise above 10^{-5} m/s at count times ranging from 1200 to 3000 s. At Venus and Jupiter encounter, the corresponding figures are 70 and 60 s, respectively. Once the doppler truncation residuals have risen above 10^{-4} to 10^{-3} m/s, all

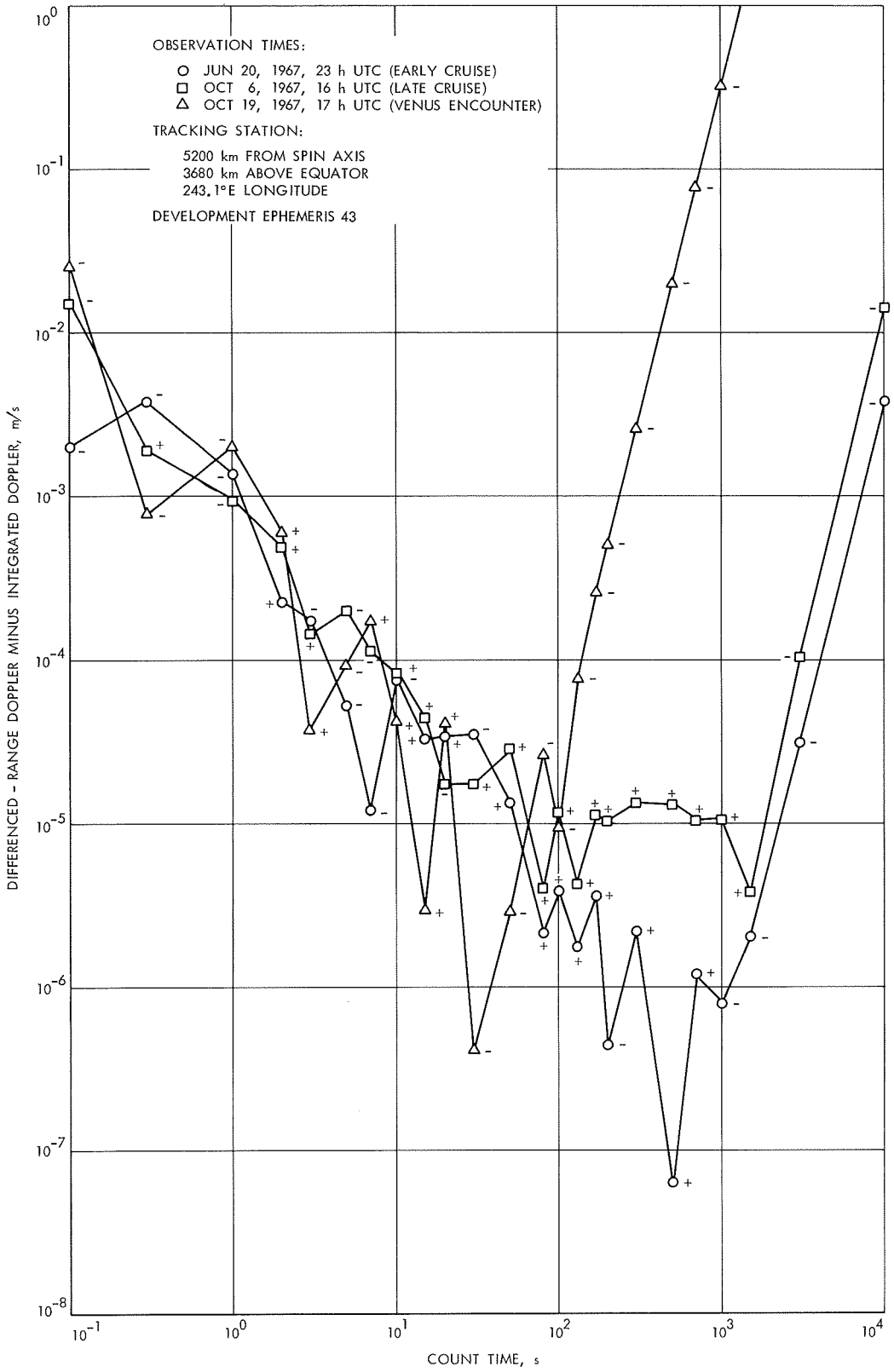

Fig. 69. *Mariner V* trajectory: Jun 20, Oct 6 and 19, 1967

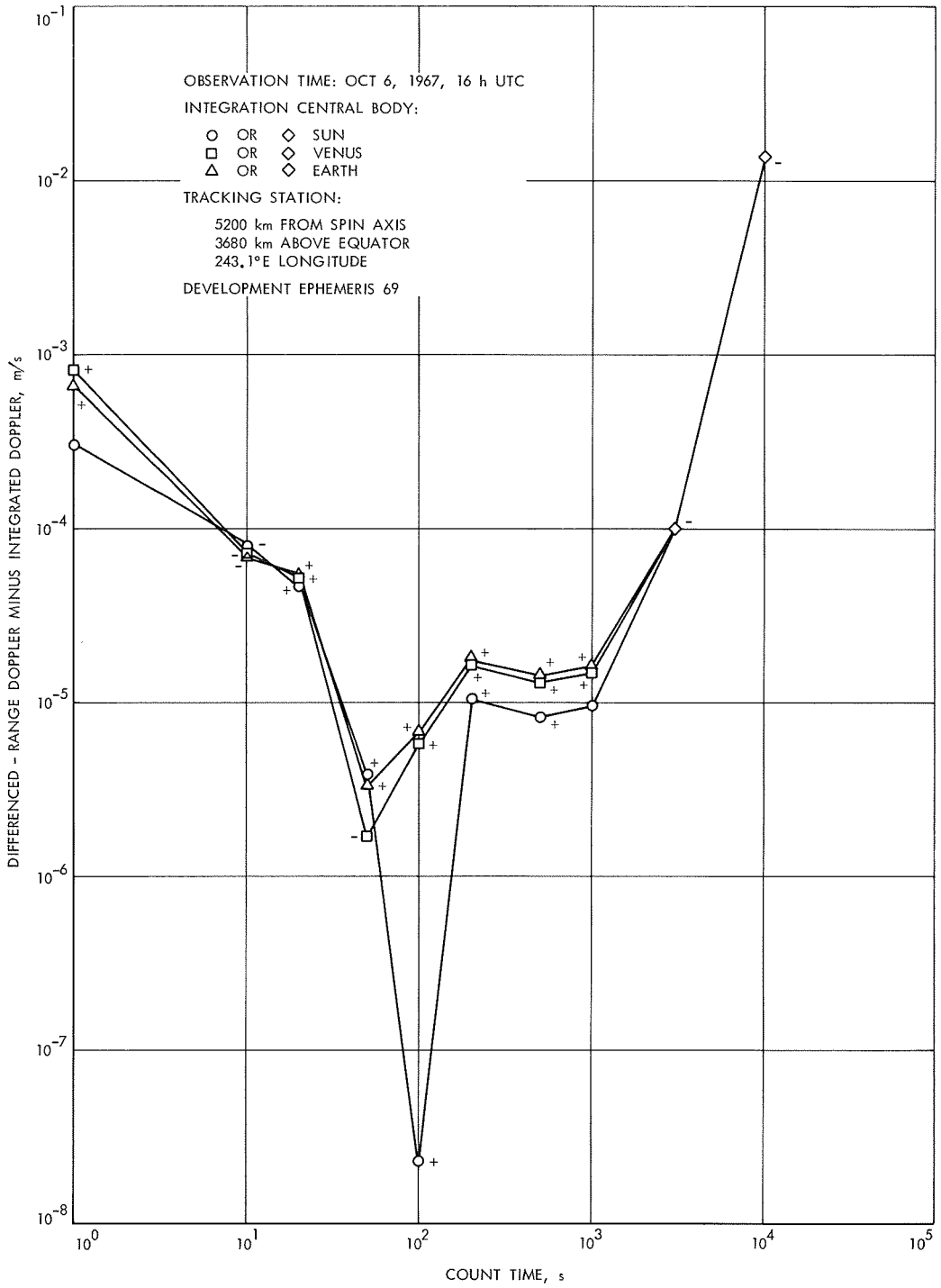

Fig. 70. *Mariner V* trajectory: variation in center of integration

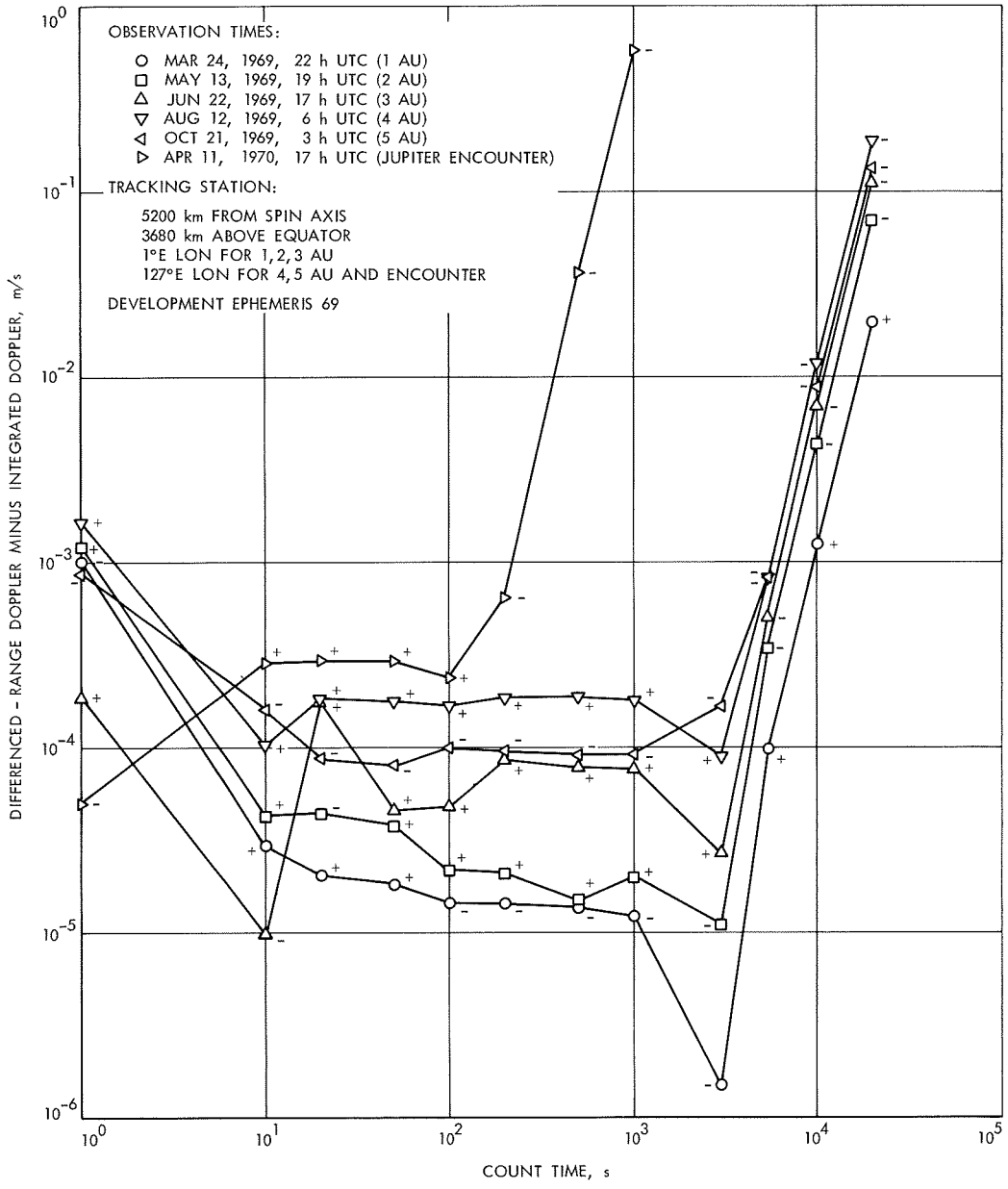

Fig. 71. Jupiter trajectory

points lie on a straight line with slope equal to four. All residuals on a given straight line have the same sign, namely, that of $[1 - (f_R/f_T)]^{iv}$. Thus, the residual versus count time curve is continuous for high count times since the doppler truncation error is continuous, whereas the residuals for moderate and particularly for low count times are discontinuous due to the random double-precision time truncation error.

If errors other than the time truncation error and the doppler truncation error were not present, minimum residuals of approximately 10^{-6} m/s would be obtained during heliocentric cruise at a count time of about 1000 s, as occurs on the *Mariner V* trajectory on June 20, 1967 (Fig. 69), where the probe range is 1.8×10^6 km. However, on October 6, 1967, where the probe range is 62×10^6 km (Figs. 69 and 70), and on the Jupiter trajectory with ranges of 1 to 5 AU (Fig. 71), the minimum residuals are 10^{-5} to 3×10^{-4} m/s with the larger values occurring for greater probe ranges. These residuals are due primarily to neglected relativity terms in the current expression for the ET − A1 time transformation (*Paragraph d*) and will be reduced to less than 10^{-5} m/s by addition of the new terms of Eq. (16). The relativity terms of ET − A1 represent the periodic variations in atomic time on earth relative to uniform ephemeris time ET (also denoted as coordinate time t in the heliocentric space-time frame of reference).

For each range observable used to compute DRD, the new terms of ET − A1 are required to accurately transform round-trip ET obtained from the light time solution to observed round-trip station time ST. The terms in DRD and in ID which arise from the periodic variations in atomic time on earth due to general relativity will be referred to as Atomic Time Theory (ATT) terms. Integrated doppler is computed using the exact differential equation relating proper time τ and coordinate time t. The only error in the ATT contribution to ID is the neglect of the second derivative of $d\tau/dt$ in Eq. (7); for the observables of this study, the maximum error is 1.0×10^{-6} m/s.

A program was written to compute the residuals between the ATT terms of DRD and ID using both the current and new expressions for ET − A1 to compute the ATT terms of DRD. Table 32 shows the DRD − ID residuals of Fig. 70 (integration central body = sun) and Fig. 71 for intermediate count times, the contribution from the ATT residuals obtained from the current expression for ET − A1, and the corrected residual with the ATT error removed. It is immediately evident that the larger residuals occurring at the larger probe ranges are due almost entirely to the ATT error. The corrected residuals

Table 32. Reduction in DRD − ID residuals with removal of ATT error[a]

Mission	$T_c = 100$	$T_c = 200$	$T_c = 500$	$T_c = 1000$
Mariner V	0.0	1.1	0.9	1.0
(Oct 6, 1967)	1.8	1.8	1.8	1.8
	−1.8	−0.7	−0.9	−0.8
Jupiter	−1.5	−1.5	−1.4	−1.3
1 AU	−1.1	−1.1	−1.1	−1.1
	−0.4	−0.4	−0.3	−0.2
2 AU	2.2	2.2	1.5	2.0
	2.1	2.1	2.1	2.2
	0.1	0.1	−0.6	−0.2
3 AU	4.9	8.6	7.9	7.9
	8.0	8.0	8.0	8.1
	−3.1	0.6	−0.1	−0.2
4 AU	17.3	18.9	19.0	18.5
	18.8	18.8	18.8	18.9
	−1.5	0.1	0.2	−0.4
5 AU	−10.1	−9.8	−9.2	−9.4
	−9.2	−9.2	−9.2	−9.2
	−0.9	−0.6	0.0	−0.2
	$T_c = 10$	$T_c = 20$		$T_c = 50$
Encounter	29.2	30.0		29.5
	29.7	29.7		29.7
	−0.5	0.3		−0.2

[a]Units = 10^{-5} m/s.
xx = existing DRD − ID residual
$\underline{xx}$ = ATT error
$\overline{xx}$ = residual with ATT error removed

are as high as 3×10^{-5} m/s at a count time of 100 s; for count times of 200, 500, and 1000 s, they are less than 10^{-5} m/s. The higher corrected residuals at the lower count times represent the previously mentioned double-precision time truncation error. Using the new expression for ET − A1, the ATT error in DRD is reduced to a maximum of 1.5×10^{-6} m/s and the ATT residuals are reduced to 2.3×10^{-6} m/s or less. Hence, Table 32 represents the approximate reduction in the DRD − ID residuals of Figs. 70 and 71 due to addition of the new terms to ET − A1.

Table 33 shows the DRD − ID residuals corrected for the ATT error (obtained from Table 32), the contribution to the residuals from the n-body ephemeris interpolation errors, and the residuals corrected for both ATT and the n-body ephemeris interpolation errors. It is seen that the maximum contribution from the n-body ephemeris interpolation errors is 0.6×10^{-5} m/s. Removal of the

Table 33. Reduction in DRD — ID residuals with removal of ATT error and ephemeris interpolation error[a]

Mission	$T_c = 100$	$T_c = 200$	$T_c = 500$	$T_c = 1000$
Mariner V (Oct 6, 1967)	−1.8 −0.6 −1.2	−0.7 −0.6 −0.1	−0.9 −0.6 −0.3	−0.8 −0.6 −0.2
Jupiter 1 AU	−0.4 −0.2 −0.2	−0.4 −0.2 −0.2	−0.3 −0.2 −0.1	−0.2 −0.2 −0.0
2 AU	0.1 0.0 0.1	0.1 0.0 0.1	−0.6 0.0 −0.6	−0.2 0.0 −0.2
3 AU	−3.1 −0.2 −2.9	0.6 −0.2 0.8	−0.1 −0.2 0.1	−0.2 −0.2 0.0
4 AU	−1.5 −0.2 −1.3	0.1 −0.2 0.3	0.2 −0.2 0.4	−0.4 −0.2 −0.2
5 AU	−0.9 −0.3 −0.6	−0.6 −0.3 −0.3	0.0 −0.3 0.3	−0.2 −0.3 0.1
	$T_c = 10$	$T_c = 20$	$T_c = 50$	
Encounter	−0.5 0.4 −0.9	+0.3 0.4 −0.1	−0.2 0.4 −0.6	

[a]Units = 10^{-5} m/s.
xx = existing DRD — ID residual with ATT error removed
$\underline{xx}$ = ephemeris interpolation error
$\overline{xx}$ = residual with ATT and ephemeris interpolation errors removed

ephemeris interpolation error greatly reduces the residuals for October 6 on the *Mariner V* trajectory and at a range of 1 AU on the Jupiter trajectory. For the remaining observation times, the residuals are changed but their average value is not. It is not possible to determine whether removal of the n-body ephemeris interpolation error is an improvement in all cases because of the presence of the random double-precision time truncation error. This error source has a typical value of 3 mm/T_c and the expected values at count times of 100, 200, 500, and 1000 s are 3, 1.5, 0.6 and 0.3×10^{-5} m/s, respectively. Thus, the remaining unaccounted for residuals of Table 33 may be due almost entirely to the double-precision time truncation error. If this is the case, the residuals will be considerably smaller on the Univac 1108 version of the DPODP. It should be noted that for a count time of 1000 s, where the time truncation error is small, removal of the n-body ephemeris interpolation error reduces the residual in every case.

Table 34 shows the DRD — ID residuals of Fig. 70 for the *Mariner V* trajectory on October 6, 1967, with the sun, Venus, and earth as integration central bodies. The uncorrected residuals vary with the center of integration. However, removal of the ATT error and different n-body ephemeris interpolation error for each center results in corrected residuals which are almost identical for each center of integration. This indicates that the double-precision time truncation error is the same for the different centers of integration. That is, changing the center of integration does not change the light time solutions for the range observables used to compute DRD. This is as expected since the variation in the heliocentric position of the probe with different centers and corresponding n-body ephemeris interpolation errors is only about 1 m, or 0.3×10^{-8} s of light time. This generally will not change the epochs of participation since the last bit of double-precision seconds past 1950 is 0.6×10^{-7} s.

The contributions to the DRD — ID residuals due to n-body ephemeris interpolation errors shown in Tables 33 and 34 are due primarily to differenced position interpretation errors divided by the count time. However, for the *Mariner V* observable of Table 33, with the sun as center of integration, the residual is almost entirely a velocity interpolation error. The upper limit for the error in either DRD or ID is probably about 10^{-5} m/s.

Table 34. Corrected *Mariner V* residuals with different integration central bodies[a]

Integration central body	$T_c = 200$	$T_c = 500$	$T_c = 1000$
Sun	1.1 1.8 −0.7 −0.6 −0.1	0.9 1.8 −0.9 −0.6 −0.3	1.0 1.8 −0.8 −0.6 −0.2
Venus	1.6 1.8 −0.2 −0.1 −0.1	1.3 1.8 −0.5 −0.1 −0.4	1.5 1.8 −0.3 −0.1 −0.2
Earth	1.7 1.8 −0.1 0.0 −0.1	1.4 1.8 −0.4 0.0 −0.4	1.6 1.8 −0.2 0.0 −0.2

[a]Units = 10^{-5} m/s; observation time = Oct 6, 1967, 16 h UTC.
xx = existing DRD — ID residual
$\underline{xx}$ = ATT error
$\overline{xx}$ = residual with ATT error removed
$\underline{xx}$ = ephemeris interpolation error
$\overline{xx}$ = residual with ATT and ephemeris interpolation errors removed

The position and velocity interpolation errors for the barycenter ephemeris are roughly sinusoidal with the vast majority of zero crossings occurring at the tabular points (four days apart). The position and velocity interpolation errors for the Venus ephemeris are zero at the tabular points and have typically 2–4 zero crossings in between. In all cases, the interpolation errors are extremely smooth functions.

Changing the representation of time from double- to triple-precision seconds past 1950 or equivalent and conversion of the DPODP to the Univac 1108 will reduce the random error of computed DRD from 3×10^{-3} m/T_c due to truncation of time beyond 16-decimal digits to 2×10^{-6} m/T_c due to truncation of position beyond 18-decimal digits. For an accuracy of 10^{-5} m/s, count times as low as 0.2 s may be used. Use of the new expression for ET − A1 (Eq. 16) will reduce the error in computed DRD to approximately 10^{-5} m/s. Use of the type 66 n-body ephemeris would reduce the error closer to 10^{-6} m/s. The growth of error in the probe ephemeris with time due to position interpolation error for the perturbing bodies would also be eliminated.

The new terms of ET − A1 affect the computed range observables by 0.01 to 1.0 m/AU. There is a monthly term of 0.05 m/AU not included in Eq. (16). In order to realize this increased accuracy, the type 66 n-body ephemeris or equivalent must be used since the current type 50 position interpolation errors are almost 1 m (or slightly larger for Mercury).